2014 - 2020 Interreg V-A

Italy - Croatia CBC Programme

Call for proposal 2019 Strategic

CoAStal and marine waters integrated monitoring systems for ecosystems proteCtion AnD managemEnt

CASCADE

Project ID: 10255941

Priority Axis: Environment and cultural heritage

Specific objective: Improve the environmental quality conditions of the sea and coastal area by use of sustainable and innovative technologies and approaches.

D4.2.1

Models simulations and forecasting systems implemented and products available

Part 2

PP1 – CMCC

Final version

Public document

May, 2023

Project acronym	CASCADE
Project ID number	10255941
Project title	CoAStal and marine waters integrated monitoring systems for ecosystems protection AnD managemEnt
Priority axis	3 - Environment and cultural heritage
Specific objective	3.2 - Contribute to protect and restore biodiversity
Strategic theme	3.2.1 - Marine environment
Word Package number	WP4
Word Package title	Monitoring (observations and modelling) and information system
Activity number	Activity 4.2
Activity title	Set up and testing of the integrated modelling system
Partner in charge	PP1 – CMCC
Partners involved	All PPs

Table of contents

3.4 Coastal area in Veneto (IT)

3.4.1 Application of a spatially explicit food web model in the Gulf of Venice, with a focus on the Tegnùe di Chioggia Natura 2000 site.

3.4.1.1 Study area

The Tegnùe di Chioggia site is one of the rocky outcrops of biogenic origin (Ponti & Mastrototaro 2005; ISPRA 2010) typical of the North Adriatic (Caressa *et al.* 2002). The considerable environmental heterogeneity that these outcrops create, standing out in a seabed dominated by muddy and sandy sediments (Russo & Artegiani 1996), and therefore the numerous environmental gradients found there, allows them to be colonised by numerous organisms, such as algae mainly from the Corallinaceae family, poriferous, bryozoans and numerous other macrobenthic species (Casellato & Stefanon 2008; Ponti *et al.* 2011; Falace *et al.* 2015). Tegnùe play an important role for some fish species, constituting an important food source, as well as a nursery site during the spawning period (ARPAV 2011; Melli *et al.* 2017). The high natural and ecological value of the Tegnùe di Chioggia was declared a Site of Community Interest (SCI) in 2012 and a Special Area of Conservation (SAC) in 2018. However, being located off the coast of Chioggia, the site is exposed to numerous pressures and threats, especially of anthropogenic origin, such as the presence of mussel farms, maritime traffic routes, sand extraction sites and trawling activities. The model developed within CASCADE project activities is intended as a useful tool to assess the vulnerability of this natural area to climatic and anthropogenic threats, and to evaluate the effectiveness of potential management measures.

3.4.1.2 Trophic network modelling approach for the Tegnùe di Chioggia in EwE

Resuming a previous work published for the North Adriatic trophic network in EwE (Libralato *et al.* 2015), we adapted this version to the natural area in front of the Tegnùe di Chioggia, introducing new structural trophic groups typical of tegnùe (Casellato & Stefanon 2008; Ponti *et al.* 2011; Falace *et al.* 2015) and updating the trophic parameterization of the model (production rates, consumption, and diet matrices). Once the stability of matter flows between trophic compartments was guaranteed (model balancing phase), geo-environmental data were processed in order to spatialize the trophic network in its structure and functioning through the Ecospace module of the software, thus obtaining a spatially explicit representation of the state of the trophic network today (base model). The inclusion of environmental drivers within the model and spatial information on the main anthropogenic pressures in the area, allowed the development of climate change and fishing effort scenarios, useful to assess the vulnerability of the area. The estimation of vulnerability was possible through the identification of suitable indicators of ecosystem structure and

functioning; the temporal variation of biomass and selected indicators, observed in Ecosim following the implementation of climate and management scenarios, allowed to assess the vulnerability of the area to the simulated pressures. Furthermore, it was possible to explore alternative spatially explicit management scenarios in Ecospace (i.e., controlled opening to small-scale fishing in the SCI, expansion of the SCI area), which were evaluated *a posteriori* through a multi-criteria analysis. To corroborate the base model, spatial data on fishing effort for Volante and Rapido tracked through the Automatic Identification System (Russo *et al.* 2020) were compared with those simulated by the base model in Ecospace.

3.4.1.3 Model theory: Ecopath with Ecosim with Ecospace

Ecopath with Ecosim (EwE) is a free software (downloadable at https://ecopath.org/downloads/.) used for modelling marine trophic networks (Christensen & Walters 2004b). Version 6.5 was used for the present study, later upgraded to version 6.6.

EwE has three main components:

- Ecopath - a static and balanced snapshot of the mass of the trophic network (Christensen & Pauly 1992);
- Ecosim - a dynamic temporal simulation module used to analyse the efficiency of management policies (Walters *et al.* 1997; Walters *et al.* 2000);
- Ecospace - a spatial and temporal dynamic module designed primarily to explore the effectiveness of marine protected area institutions (Walters *et al.* 1999).

Ecopath represents the ecosystem through functional groups, i.e., groups of trophically and ecologically similar species/taxa that exchange matter with each other through prey-predator trophic relationships defined by the diet matrix. Ecopath ensures the mass balance for each trophic group, i.e., the balance between the total production and consumption of the trophic group (Hernvann *et al.* 2020). The network balance is based on two fundamental equations, whose minimum necessary parameters must be provided as input by the user (Christensen & Walters 2004):

- B (biomass in the area; t/km2);
- P/B (production rate of the trophic group; y-1);
- Q/B (consumption rate of the trophic group; y-1)
- EE (Ecological efficiency of the trophic group, i.e., proportion of the production used in the ecosystem).

At least 3 parameters from the list must be estimated, while the 4' will be calculated accordingly by the software, in order for the network balancing to be satisfied (Christensen & Walters, 2004). In addition, the diet composition (DCij) the total fishing yield (Yi) must be provided for each group.

During the balancing process, the trophic parameters and diet matrices provided as input by the user are gradually modified, starting with the trophic groups whose matter flows are most unbalanced and the parameters whose estimation is most uncertain (Heymans *et al.* 2016). Once the balanced version of the network is obtained in Ecopath, the Ecosim module allows to assess the temporal stability of the trophic network balance over time, as well as the temporal variation of the trophic group biomass, by implementing effort management scenarios and/or introducing climate forcings (Christensen *et al.* 2008). Once the temporal stability of the trophic network balance has been verified, it is possible to proceed with the spatialisation of the network in Ecospace. Ecospace is the spatial component of EwE, which predicts the spatial distribution of the biomass of the functional groups on a 2-D horizontal grid (Walters *et al.* 1999; Pauly *et al.* 2000) whose resolution is provided as input by the user. Each trophic group can be spatialized as it is assigned to specific habitats within the study area or based on its tolerance responses to different environmental factors; the combination of environmental responses defines the 'capacity' of each grid cell to forage the trophic group (value from 0 to 1) (Christensen *et al.* 2014; Hernvann *et al.* 2020); the capacity then determines the distribution of trophic group biomass across space (Christensen *et al.* 2014).

3.4.2 Application of EwE software to the Le Tegnùe di Chioggia case study

3.4.2.1 Network parameterization and balancing in Ecopath

For 'Le Tegnùe di Chioggia' (P5 - CASCADE), the structure of the Ecopath model and its parameterization, was largely taken from the version developed for the North Adriatic Sea (Libralato *et al.* 2015): this version included 22 trophic groups to represent the primary producers, such as phytoplankton, but also the detritus compartment, macrobenthic groups, zooplankton, and the fish compartment. The model also includes fishing fleets (Volante, Rapido, Coccia, Vongolara, Artisanal Fishing and Recreative Fishing), whose catches (tkm-2year-1) and discards (tkm-2year-1) were taken from the North Adriatic version. The trophic group *Mytilus galloprovincialis* (MYT), present in mussel farms in the area, and the trophic group *Chamelea gallina* (CHA), which replaces the pre-existing group of the family Veneridae, were added. Trophic groups typical of rocky outcrops were also included:

- Primary producers of Tegnùa (PPT): *Lithophyllum stictaeforme, Lithothamnion minervae, Peyssonnelia polymorpha* and turf algae;
- Tegnùa filter feeders (FFT): *Dictyonella incisa, Antho inconstans, Cliona viridis, Tedania anhelans, Epizoanthus spp, Polycitur adriaticus*;
-Nekton Tegnùa (DIP, PAG, SPI): *Pagellus erythrinus, Spicara smaris, Diplodus annularis*.

The complete list of trophic groups and species included can be found in Appendix I. For these additional trophic groups, the trophic parameterization required by the Ecopath fundamental equations and diet matrices was taken from literature (Sala *et al.* 2012; ISPRA 2010; Šantić *et al.* 2011a, b; Adriat *et al.* 2014), databases (Fishbase.org and Sealifebase.org), or by assuming identical parameterization to the trophically similar groups to already included in the model. For PPTs, biomass estimation was carried out through collaboration with the University of Bologna (Prof. Massimo Ponti and Eva Turicchia). The % cover of all species falling into the category was analysed from sampling carried out during the field sessions of the Project and through cover-biomass conversion factors, it was possible to estimate the trophic group's wet mass per unit area. For mussels, diet matrices were updated by considering the fraction of phytoplanktonic and non-phytoplanktonic carbon available (Brigolin *et al.* 2009). The fraction of carbon of non-phytoplanktonic origin was equally distributed between micro-, macro- and bacterial plankton, assuming non-selective filtration. Assuming the longevity of an average individual of *Mytilus galloprovincialis* in a mussel farm to be one year, and the reciprocal of P/B being an estimate of the longevity of an individual (Christensen *et al.* 2008), we assumed P/B = 1. We estimated an average biomass of 180 tkm-2 in a mussel farm, as the average biomass of an individual in a farm is about 0.6 g, while the weight at harvest is about 1 g (Brigolin *et al.* 2009); knowing that, at harvest, the total biomass produced is 300 tkm-2 (Brigolin *et al.* 2009), it follows that average individual weight * n' individuals = 0.6*300 = 180 tkm-2 is the average biomass present in a year. The process of balancing the network consisted of gradually changing the biomass and/or parameters and/or diets of the most unbalanced trophic groups, initially changing the parameter whose estimate was most uncertain (Heymans *et al.* 2016). It is important to note that the biomasses and parameters taken from the published version for the North Adriatic refer to biomass estimates and trophic relationships attributable to the North Adriatic Sea. Maintaining the same biomass and diet matrices within the Chioggia area, we assume that our study site is comparable to the trophic network described for the North Adriatic.

3.4.2.2 Spatialisation in Ecospace

Three different basemaps were inserted from the outset: the primary productivity map as the mass concentration of chl-a in the water column normalised between 0 and 1 (Oceancolour-MED-CHL-L4; CMS), the bathymetric profile (EMODnet Digital Bathymetry DTM) and the study area as a grid of cells at a resolution of 1 km.

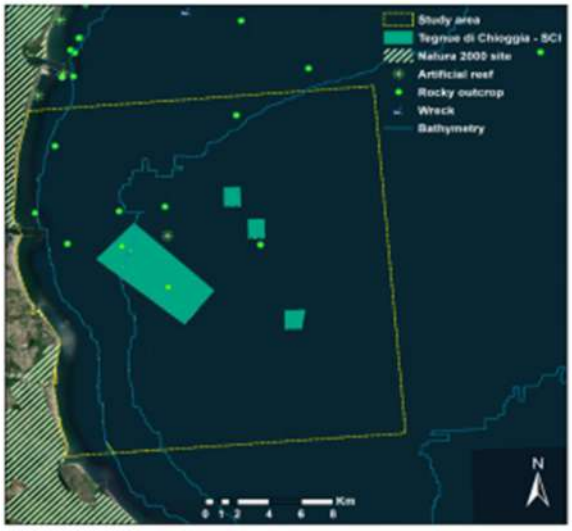

Figure 59. The study area modelled in Ecospace is enclosed by the yellow square. In green are the polygons representing the SCI area, while the green points represent the rocky outcrops.

Four different habitats were considered in the study area based on the type of seabed and the presence or absence of mussel farms:

- Mussel farms: habitat characterised by the presence of mussel farms in the water column (% cell coverage (Mariculture - Adriatic Sea - Tools4MSP, from Adriatic ATLAS of SHAPE Project).
- Sandy bottom: habitats with a predominantly sandy bottom (% cell coverage; EMODnet Seabed substrates Multiscale FOLK 7)
- Muddy bottom: habitats with a predominantly muddy bottom (% cell coverage; EMODnet Seabed substrates Multiscale FOLK 7)
- Rocky outcrops: habitats characterised by the presence of rocky outcrops (% cell coverage; Ponti 2020 (a)(b)(c); Fortibuoni *et al.* 2020 (a)(b); Gordini & Ciriaco 2020; Andreoli *et al.* 2010)

The groups sensitive to the presence of these environments were assigned with a preference coefficient from 0 to 1 for each habitat, based on previous knowledge (Table 14).

For trophic groups *Chamelea gallina*, PEC, BFD, CPH, FFS, NFD, PLT, *Diplodus annularis, Spicara smaris, Pagellus erythrinus* (see Appendix I) environmental responses to bathymetry were included following Bentley et al. (2016) (Figure 61). The environmental response describes the suitability of the parameter (bathymetry) for the presence of the species and contributes, through a linear combination, to define the capacity of the cell to forage the trophic group (Christensen *et al.* 2014; Hernvann *et al.* 2020). Curves were obtained following the approach described by Bentley *et al.* (2017) with data provided by Aquamaps. From the minimum and maximum bathymetric optimum provided by Aquamaps, the mean value of these two bathymetric limits was calculated to obtain

the bathymetric optimum for each species. For trophic groups with more than one species, the bathymetric minimum and maximum optimum, and therefore also the optimum, were calculated by averaging the species-specific values within the trophic group to obtain the optimal bathymetric range for the entire trophic group.

Table 14. habitat preference coefficients for trophic groups

Group	All	Rocky	Farms	Sandy	Muddy
PPT	0	1	0	0	0
PFT	0	1	0	0	0
FFT	0	1	0	0	0
MDT					
T	0	1	0	0	0
DIP	0	1	0,2	0,6	0,6
SPI	0	1	0,5	0,5	0,5
PAG	0	1	0,5	0,6	0,6
MYT	0	0	1	0	0
NFD	1	0	0	0	0
CPH	0	0,7	0,7	0,7	1
FFS	0	0	0,8	0,7	1
BFD	1	0	0	0	0
PLT	1	0	0	0	0
MOP	1	0	0	0	0
MMF	0	0,5	0,5	1	1
MFF	0	1	0,5	0,8	0,6
PEC	0	0	1	1	1
CHA	0	0	1	1	1
MZP	1	0	0	0	0
MDT	0	0,4	0,5	0,8	1
MHR	1	0	0	0	0
MEI	1	0	0	0	0
JEL	1	0	0	0	0
MIZ	1	0	0	0	0
BPL	1	0	0	0	0

From the occurrence data of each species and its bathymetry (occurrence cells in Aquamaps.org), the standard deviation between the minimum bathymetric optimum and all the shallowest depths

at which the species was observed was calculated (SD left) and repeated for the maximum bathymetric optimum (SD right). In this way, we obtained the "left and right" standard deviation of the bathymetric optimum. This allowed us to draw the skewed normal bathymetry tolerance curve for the trophic group to be included in the "environmental responses" module in Ecosim. As the % species composition of biomass and catch in the area was not available, it was necessary to assume that each species contributed equally to the bathymetric suitability profile for the trophic group. The same procedure was replicated for the environmental temperature tolerance data. In this case, the environmental suitability curves obtained were not used to model the biomass distribution of the groups in Ecospace, but to assess the vulnerability of the trophic groups to temperature variations (Figure 62).

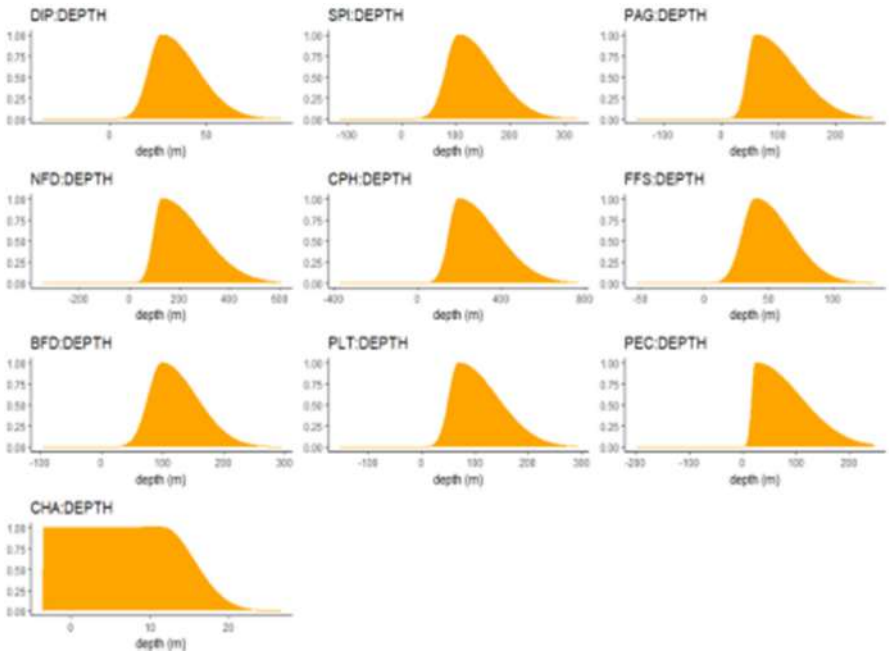

Figure 60. Environmental tolerance curves to bathymetry, used in Ecospace to distribute the biomass of trophic

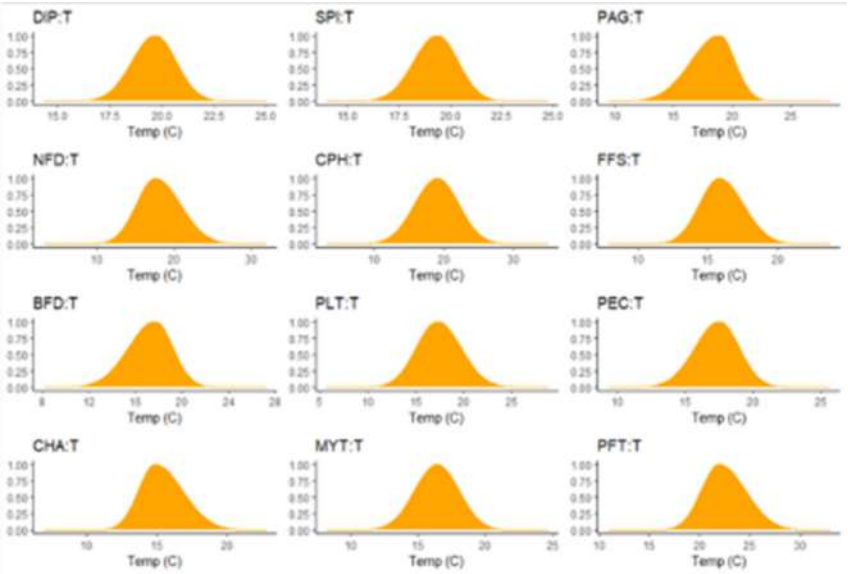

Figure 61. Environmental temperature tolerance curves, used in Ecosim to estimate the vulnerability of the system to climate change scenarios.

Within the study area, 3 fishing closure zones have been mapped through the creation of shapefiles:

- Tegnùe di Chioggia SCI, closed to fishing all year round for any boat;
- Coast within 3 miles, closed all year round to bottom trawling (Volante, Rapido, Coccia);
- area closed to clamming within 3 metres of bathymetry where *Chamelea gallina* cannot be taken.

The biomass of each group within the cells can move to adjacent cells depending on food availability and vulnerability to predation, influenced, for instance, by the presence of unfavourable environmental conditions, and on their intrinsic rate of mobility, due to random population movements, defined as dispersal (Fouzai *et al.* 2012). Based on the study by Fouzai *et al.* 2012, a dispersal rate of 300 was set for pelagic species, a dispersal rate of 30 for demersal species and 3 for sessile or poorly mobile species.

3.4.3 Model corroboration

Prior to the extraction of the indicators and the development and analysis of the climatic and management scenarios, the results for fishing effort obtained at steady state for the Ecospace base model were compared with those observed in situ using the Automated Identification System of the Volante and Rapido fleets (Russo *et al.* 2020). In particular, the fishing effort maps simulated at steady state by Ecospace for the base model at the scale of the Tegnùe di Chioggia were compared with the fishing effort maps obtained from AIS data for the Volante and Rapido di Chioggia (Russo *et al.* 2020). Fishing effort indices were compared on an annual average basis for each 1kmx1km

cell. The correlation between simulated effort and effort observed through AIS was estimated by repeating a correlation test (default cor.test() in the stats package of R 4.1.2) 1000 times on subsamples of 100 cells randomly extracted from the study area. This procedure should exclude the occurrence of spurious correlation due to large sample sizes (Calude & Longo 2015). At the end of the process, the average correlation and the percentage of significant correlations out of the 1000 tests carried out was calculated.

3.4.4 Selection and extraction of indicators of ecosystem structure and functioning

Part of the indicators used for estimating system vulnerability and evaluating the effectiveness of management measures were obtained through the ECOIND plugin available with the free version of the software (Coll & Steenbeek 2017). The plugin produces tables, time-plots or indicator maps, for Ecopath, Ecosim and Ecospace respectively. In addition, through interaction with Pierre-Yves Hernvann, it was possible to acquire a post-processing algorithm for the spatial data of Ecospace not included in the basic software suite. By means of this additional tool, starting from the absolute biomass distribution maps of trophic groups per km2 obtained from Ecospace, and from Ecopath's estimates (Trophic Level and Omnivory Index), it was possible to calculate the System omnivory index (SOI), which measures the distribution of trophic interactions between the trophic levels of the networks, thus SOI allows to assess the complexity and connectivity of trophic networks (Libralato 2018; Hernvann *et al.* 2020). The complete set of indicators considered is resumed in Table 15.

Table 15. Indicators used to summarize outputs and assess vulnerability of the pilot area and effects of management scenarios on the ecosystem.

Indicator	Unit	Description
Total B	t/km^2	Total biomass (B)
Commercial B	t/km^2	Biomass (B) of commercial species
Invertebrates / Fish B		Biomass (B) of invertebrates over fish biomass
Kempton's Q		Kempton's diversity index (Q)
Shannon		Shannon diversity index
Total C	t/km^2/year	Total catch (C)
TL catch		Trophic level (TL) of the catch
SOI		System Omnivory Index of the food web (Hernvann *et al.* 2020)
MTI		Marine Trophic Index of catch with TL >= 3.25

3.4.5 Exploring effects of increased sea-surface temperature, primary productivity, and fishing effort: scenarios for vulnerability assessment

To estimate the vulnerability of the system, time simulations were implemented in Ecosim, through the input of climatic-biological and fishing effort (trawl fleets) time series into the software, aimed at reproducing scenarios of temperature increase (vulnerability to climate change), primary productivity and fishing effort (vulnerability to overfishing). The time span considered is 40 years, from 2014 to 2053. Following the implementation of the climate and management simulations, the temporal variation of the indicators and biomass of the trophic groups was quantified compared to the baseline scenario, i.e., without climate or management forcing, at steady state. The proposed scenarios are designed to simulate the effect of the anthropogenic and environmental pressures identified for the study area. The magnitude of the indicator change and the direction of this change (increase or decrease) will provide an assessment of the vulnerability of the study site to the assumed pressure scenarios.

3.4.6 Model application to the exploration of management options

The management options include both measures to protect the biodiversity of the study system and measures to enhance socio-economic activities of the area. The measures considered are:

A) SCI expansion: the expansion of the SCI would allow for greater connectivity and dispersion of organisms within its perimeter (D3.2.1 Report, ECOSS Project 2020). A protected natural area should in fact be large enough to allow free movement of larger organisms within it (Lundquist & Granek 2005). Enlarging the boundaries of the SCI could also reduce the impact of some human activities in the area, such as the release of waste from boats, illegal fishing, noise pollution and the burial of benthic communities due to trawling activities in areas near the site, among the main threats identified for the Tegnùe di Chioggia (D3.2.1 Report, ECOSS Project 2020; Piazzi *et al.* 2012).

B) Controlled opening of artisanal, recreational and sport fishing in the SCI in the winter period; examples of marine protected areas and other natura 2000 sites have concessions of controlled fishing from small boats in some areas of the natural site, such as the MPA "Secche di Tor Paterno" (Disciplinare integrativo al regolamento di esecuzione ed organizzazione dell'area marina protetta "Secche di Tor Paterno" 2021) and the SCI Torre del Cerrano (Vallarola *et al.* 2015). By controlling and limiting recreational and sport fishing in the area, it would be possible to minimise impacts on fish stocks, and to create a synergic relationship with fishermen aimed at collaboration in controlling major offences.

For the evaluation of the management proposals, a multi-criteria analysis was carried out for each one (MCA; Antunes *et al.* 2011; Khalili & Duecker 2013), i.e., a linear combination of information layers useful for synthesizing the information produced by complex management scenarios acting on the ecosystem and multiple production sectors. Multi-criteria analysis identifies criteria for evaluating a management proposal, and indicators aimed at quantifying the performance of those criteria. In our case, to evaluate the efficiency of a management measure within the natural and socio-economic context of the area, four evaluation criteria and related indicators were identified:

- Nature criterion: Kempton, System Omnivory Index, Marine Trophic Index;
- Fisheries criterion: Total Catch, Commercial Biomass of fish fauna;
- Chamelea criterion: Chamelea gallina catches, Chamelea gallina biomass;
- Mussel farm performance criterion: Mussel farm biomass.

The indicators for each criterion were calculated within sub-regions of the study area (see Figure 63), where we wanted to estimate the performance of the criterion to be maximised. The indicators for the fishery criterion will be calculated in the area surrounding the SCI (Region 1) and outside the 3 miles from the coast (Region 3); the mussel farm performance indicators will be calculated exclusively within the portion of space occupied by mussel farms (Region 2); the indicators for the Chamelea criterion will be calculated within 3 miles from the coast (Region 4), while the biodiversity indicators will be calculated for all sub-areas. For each sub-area, the mean value of the indicator on its spatial cells and the respective standard deviation were calculated. The biodiversity criterion indicators were first averaged over the cells within the sub-areas and then averaged across regions to obtain an overall estimate of criterion performance for each scenario. Subsequently, each indicator was normalised between 0 and 1, dividing the relative values by the maximum value observed on each indicator for each scenario. Finally, for each criterion, the normalised indicators were averaged, so that the criteria contribute equally to determining the score of the management scenario, regardless of the number of indicators that compose them. The final score resulting from the multi-criteria analysis will be the result of the linear combination of the performance of the different criteria through the sum of the average values of each indicator in the relevant sub-areas:

$$S_{scenario} = P_{\ \ nature} + P_{fishing} + P_{mussel-farms} + P_{chamelea} =$$

$$mean\left(K_m^{1,2,3,4}, MTI_m^{1,2,3,4}, SOI_m^{1,2,3,4}\right) + mean\left(B_m^{3,fish}, C_m^{3,fish}\right) + B_m^{2,myt} + \ mean(B_m^{4,Cha}, C_m^{4,Cha})$$

The equation is the linear combination equation for the multi-criteria analysis of the proposed management scenarios; each criterion performance (Pbiodiversity, Fishing, Pmitiliculture, Pchamelea) consists of the average of the indicator values (pedicem) belonging to each criterion,

calculated in the relevant regions, and normalised between 0 and 1. At the top of each indicator the region (1,2,3,4) and the relevant trophic group.

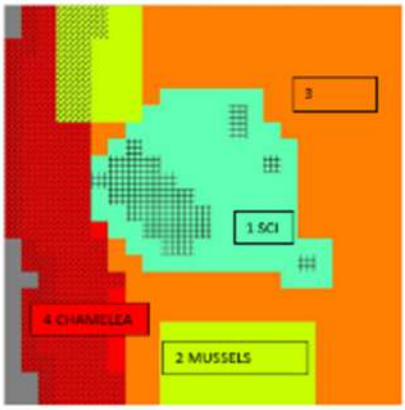

Figure 62. Study area divided into the sub-regions where the sets of performance indicators of the criteria for multi-criteria analysis were calculated.

3.4.7 Temporal scenarios: climate change and management combined effects

Two climate scenarios were produced using sea surface temperature and Chl-a-a values in water column timeseries produced according to the global emissions scenarios RCP4.5 and RCP8.5:

For the Sea Surface Temperature variable, temperature data (Celsius) simulated by the Coordinated Downscaling Experiment EURO-CORDEX for the CS 15A Region from the ClimeFish project (corresponding to the North Adriatic coasts) are used, according to the RCP4.5 and RCP8.5 scenario. The EURO-CORDEX simulations consider global climate simulations from the long-term CMIP5 experiments up to the year 2100 (Jacob *et al.* 2014; http://www.euro-cordex.net). They are based on greenhouse gas emission scenarios (Representative Concentration Pathways, RCPs) that correspond to the stabilisation of radiative forcing after the 21st century at 4.5 W/m² (RCP4.5), the increase of radiative forcing to 8.5 W/m² at the end of the 21st century (RCP8. 5), and to the peak of radiative forcing by the 21st century at 3.0 W/m² and subsequent decline (RCP2.6, also referred to as RCP3-PD) (van Vuuren *et al.* 2008; Moss *et al.* 2010; Nakicenovic *et al.*2000). For both scenarios, the daily temperatures of 14 available simulations were averaged. Subsequently, the daily temperatures were averaged to obtain the average annual temperature over the period 2014 - 2054. The annual average temperatures obtained in this way were entered into Ecosim as climate forcings (Figure 64).

With respect to primary productivity, Chl-a concentration trend scenarios (ug/L) were obtained from PolcomsErsem model data on combined European GCOMS domains (POLCOMS-AMM v6.3 and ERSEM 15.06) and processed to be representative of the CS15A region (North Adriatic Coastal

Zone). These timeseries were input into the model as temporal forcings of the total phytoplankton biomass within the trophic network, and it was therefore necessary to trace the corresponding t/km2 from the ug/L values. To do this, a homogenous concentration was assumed throughout the model study area (Atot = 514 km2, mean bottom bathymetry = 20 m, V (km3) of H20 = 1, L H20 = 1*10^12). From the L concentration of Chl-a-a in ug, the total tonnes of Chl-a-a in the estimated volume of water in the study area were calculated. Using two conversion factors (C phyto = 50*Chl-a-a and 10*cphyo = B phyto) (ref), it was possible to calculate the total phytoplankton biomass over the reference area (t/km2). Both climate scenarios (RCP4.5 and RCP8.5) were combined with two different fishing effort scenarios, in order to explore the cumulative effects of changes in fishing intensity and climate change:

1. Increase in fishing effort of professional fleets (bottom trawling and clam dredges) by 30% in 10 years.
2. Decrease in fishing effort of the professional fleets (trawling and clam dredges) by 30% in 10 years. All simulations lasted 40 years for a total of 480 monthly time steps (January 2014 - December 2053). Simulations carried out for vulnerability assessment are resumed in Table 16.

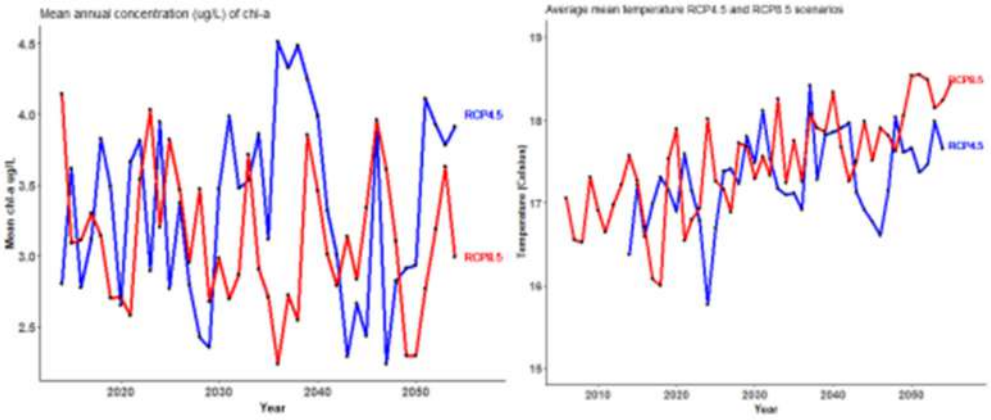

Figure 63. Annual mean sea surface temperature and Chl-a-a ug/L trends for the RCP4.5 and RCP8.5 scenarios

Table 16. simulations for the vulnerability assessment.

Name of the simulation	Climate change scenario	Fishing effort scenario
Baseline	-	-
RCP4.5	SST and Chl-a-a RCP4.5 scenarios	-
RCP8.5	SST and Chl-a-a RCP8.5 scenarios	-
RCP4.5_eff30	SST and Chl-a-a RCP4.5 scenarios	Increased professional fleets fishing effort by 30% in 10 years
RCP8.5_eff30	SST and Chl-a-a RCP8.5 scenarios	Increased professional fleets fishing effort by 30% in 10 years

RCP4.5_eff_low30	SST and Chl-a-a RCP4.5 scenarios	Decreased professional fleets fishing effort by 30% in 10 years
RCP8.5_eff_low30	SST and Chl-a-a RCP8.5 scenarios	Decreased professional fleets fishing effort by 30% in 10 years

3.4.8 Model results: baseline simulation and model spatialization

The balanced trophic network obtained from Ecopath comprises several trophic groups below trophic level 3. The contribution of the detritus and carcass compartment in terms of biomass is important (Figure 65). Regarding spatialisation in Ecospace, the timeplot of the average biomass in the study area reaches steady state after an initial biomass settling. At steady state, there is a strong decrease in the available biomass of *Chamelea gallina*, with a restriction of the area occupied by the species (Figures 66 - 67). The species is concentrated in the bathymetry zone where its extraction is not allowed and in the northwestern area of the SCI (Figure 67). The structuring species that can be traced back to the presence of woodlots (ISPRA 2010), such as *Diplodus annularis, Pagellus erythrinus and Spicara smaris*, are located near the outcrops (Figure 67).

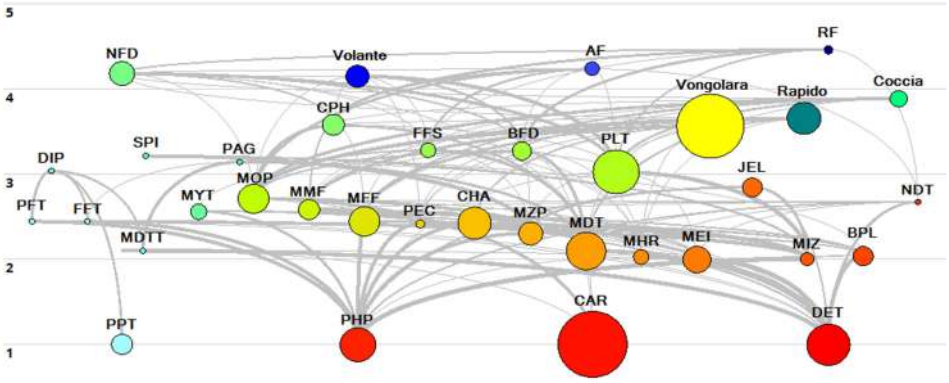

Figure 64. Structure of the trophic network. The width of the circles and the thickness of the links are directly proportional to the abundance of the trophic group (t*km-2)) and to the amount of matter exchanged in the prey-predator relationship, respectively. On the left, in numbers, are the trophic level bands within which the groups are positioned.

Table 17. Set of indicators obtainable from ECOIND for Ecopath, Ecosim and Ecospace. In this case, the values shown have been calculated on the balanced Ecopath base model.

Indicators extracted from ECOIND plug-in

Indicator	Value	Units	Description
Biomass-based			
Total B	85.32	t/km^2	Total biomass (B)
Commercial B	28.34	t/km^2	Biomass (B) of commercial species
Invertebrates / Fish B	2.32		Biomass (B) of invertebrates over fish
Kempton's Q	2.78		Kempton's diversity index (Q)
Shannon diversity	2.79		Shannon diversity index
Catch-based			
Total C	29.56	t/km^2/year	Total catch (C)
Trophic-based			
TL catch	2.67		Trophic level (TL) of the catch
System Omnivory Index	0.18		System Omnivory Index of the food web (Hernvann et al. 2020)
Marine Trophic Index	3.67		Marine Trophic Index of TG with TL >= 3.25 (Hernvann et al.2020)

The total commercial biomass constitutes about 1/3 of all available biomass in the study area per 1kmx1km cell (Table 17). However, the total annual catch exceeds the available commercial biomass, probably due to the share of bycatch. Invertebrates are twice the size of the fish fauna in the study area and the trophic level of the catch is relatively low, despite CPH, FFS, NFD and BFD (commercial fish fauna) having a TL >= 3.25.

Table 18. Baseline estimates provided by Ecopath following balancing.

Balanced food web parameters

GT	TL	Hab area prop	B in hab area (t/km^2)	Biomass (t/km^2)	P/B	Q/B	EE	P/Q	BA (t/km^2)	BA rate
PPT	1.00	0.001	300.00	0.30	0.02392137	-	0.9000000	-	-	-
PFT	2.44	0.001	6.00	0.01	4.77	23.85	0.3320115	0.2	-	-
FFT	2.44	0.001	6.00	0.01	4.77	23.85	0.2444793	0.2	-	-
MDTT	2.10	0.001	12.00	0.01	7.46	37.3	0.1346261	0.2	-	-
DIP	3.04	0.001	6.00	0.01	1.57	4.917006	0.0000000	0.3193	-	-
SPI	3.22	0.001	2.00	0.00	1.65	4.946043	0.0000000	0.3336	-	-
PAG	3.14	0.001	2.00	0.00	1.57	4.917006	0.0000000	0.3193	-	-
MYT	2.56	1.000	1.30	1.30	1	5	0.0622238	0.2	-	-
NFD	4.18	1.000	2.60	2.60	0.57	2.132586	0.5771918	0.2672811	-	-
CPH	3.58	1.000	2.14	2.14	1.68	5.599999	0.4818867	0.3	-	-
FFS	3.28	1.000	1.16	1.16	1.47	7.35	0.3166440	0.2	-	-
BFD	3.27	1.000	1.69	1.69	1.57	4.917137	0.7059611	0.3192915	-	-
PLT	3.03	1.000	8.40	8.40	1.65	4.946178	0.4426750	0.3335909	-	-
MOP	2.71	1.000	3.70	3.70	4.96	12.4	0.9616659	0.4	-	-
MMF	2.58	1.000	1.99	1.99	9.22	46.1	0.9879994	0.2	-	-
MFF	2.44	1.000	3.80	3.80	4.77	23.85	0.9602443	0.2	-	-
PEC	2.42	1.000	0.30	0.30	0.8	4	0.9201441	0.2	-	-
CHA	2.42	1.000	4.50	4.50	1.41	7.05	0.3940111	0.2	-	-
MZP	2.31	1.000	2.50	2.50	20.087	100.435	0.8408422	0.2	-	-
MDT	2.10	1.000	6.05	6.05	7.46	37.3	0.9874836	0.2	-	-
MHR	2.02	1.000	1.13	1.13	7	35	0.9424067	0.2	-	-
MEI	2.00	1.000	3.10	3.10	13.704	68.52	0.9978908	0.2	-	-
JEL	2.85	1.000	1.75	1.75	14.6	50.48	0.1727209	0.2892235	-	-
MIZ	2.00	1.000	0.83	0.83	219	438	0.8084751	0.5	-	-
BPL	2.04	1.000	1.86	1.86	34.348	171.74	0.8245362	0.2	-	-
NDT	2.67	1.000	0.05	0.05	0.54	23.5	0.4068317	0.02297872	-	-
PHP	1.00	1.000	4.90	4.90	155.13	-	0.8268452	-	-	-
CAR	1.00	1.000	22.12	22.12	-	-	0.2589362	-	-	-
DET	1.00	1.000	7.40	7.40	-	-	0.9880917	-	9.527832	1.287807

Table 19. Balanced diet matrix obtained from Ecopath estimates.

Diet Matrix of the balanced food web

Prey	PFT	FFT	MDTT	DIP	SPI	PAG	MYT	NFD	CPH	FFS	BFD	PLT	MOP	MMF	MFF	PEC	CHA	MZP	MDT	MHR	MEI	JEL	MIZ	BPL	NDT	PHP	CAR	DET
PPT	-	-	-	0.01	-	-	-	-	-	-	-	-	-	-	-	-	-	-	-	-	-	-	-	-	-	-	-	-
PFT	-	-	-	0.01	-	-	-	-	-	-	-	-	-	-	-	-	-	-	-	-	-	-	-	-	-	0.05	-	-
FFT	-	-	-	0.01	-	-	-	-	-	-	-	-	-	-	-	-	-	-	-	-	-	-	-	-	-	0.05	-	-
MDTT	-	-	-	0.01	-	-	-	-	-	-	-	-	-	-	-	-	-	-	-	-	-	-	-	-	-	0.17	-	-
DIP	-	-	-	-	-	-	-	-	-	-	-	-	-	-	-	-	-	-	-	-	-	-	-	-	-	0.02	-	-
SPI	-	-	-	-	-	-	-	-	-	-	-	-	-	-	-	-	-	-	-	-	-	-	-	-	-	0.01	-	-
PAG	-	-	-	-	-	-	-	-	-	-	-	-	-	-	-	-	-	-	-	-	-	-	-	-	-	0.01	-	-
MYT	-	-	-	-	-	-	-	-	-	-	0.08	-	-	-	-	-	-	-	-	-	-	-	-	-	-	2.52	-	-
NFD	-	-	-	-	-	-	-	0.55	-	-	-	-	-	-	-	-	-	-	-	-	-	-	-	-	-	1.73	-	-
CPH	-	-	-	-	-	-	-	0.72	0.36	-	-	-	-	-	-	-	-	-	-	-	-	-	-	-	-	4.27	-	-
FFS	-	-	-	-	-	-	-	0.17	-	-	-	-	-	-	-	-	-	-	-	-	-	-	-	-	-	2.87	-	-
BFD	-	-	-	-	-	-	-	0.83	-	-	0.16	-	-	-	-	-	-	-	-	-	-	-	-	-	-	2.44	-	-
PLT	-	-	-	-	-	-	-	2.77	1.2	0.26	-	-	-	-	-	-	-	-	-	-	-	-	-	-	-	16.03	-	-
MOP	-	-	-	-	-	-	-	0.05	5.4	1.2	1.15	-	0.91	-	-	-	-	-	-	-	-	-	-	-	0.1	9.88	-	-
MMF	-	-	-	-	-	-	-	-	1.56	0.68	0.82	-	2.29	3.63	-	-	-	-	-	-	-	-	-	-	0.1	18.57	-	-
MFF	-	-	-	-	-	-	-	-	0.24	0.43	1.15	-	2.29	9.18	-	-	-	-	-	-	-	-	-	-	0.1	22.83	-	-
PEC	-	-	-	-	-	-	-	-	-	-	0.08	-	-	-	-	-	-	-	-	-	-	-	-	-	-	0.26	-	-
CHA	-	-	-	-	-	-	-	-	-	-	-	-	-	-	-	-	-	-	-	-	-	-	-	-	-	11.78	-	-
MZP	-	-	-	-	0.01	-	1.09	-	-	0.85	0.08	4.95	-	-	2.72	0.06	1.58	-	-	-	-	30.86	-	-	-	-	108.43	-
MDT	-	-	-	-	-	-	-	0.44	2.28	4.27	3.7	-	21.09	11.93	-	-	-	-	-	-	-	-	-	-	0.05	56.98	-	-
MHR	-	-	-	-	-	-	-	-	0.96	0.83	0.82	-	-	4.59	-	-	-	-	-	-	-	-	-	-	0.1	12.34	-	-
MEI	-	-	0.04	-	-	-	-	-	-	-	-	1.25	0.92	16.52	-	-	-	-	22.57	0.99	-	-	-	-	0.1	-	63.81	-
JEL	-	-	-	-	-	-	-	-	-	-	-	-	-	-	-	-	-	-	-	-	-	4.41	-	-	-	-	38.8	-
MIZ	0.04	0.04	-	-	-	-	1.09	-	-	-	-	54.93	-	-	27.19	0.36	9.52	37.66	-	-	-	26.53	-	9.59	-	-	180.23	-
BPL	0.01	0.01	-	-	-	-	1.09	-	-	-	-	-	-	-	9.06	0.06	1.59	37.66	-	-	-	-	-	3.2	-	-	139.01	-
NDT	-	-	-	-	-	-	-	-	-	-	-	-	-	-	-	-	-	-	-	-	-	-	-	-	-	0.58	-	-
PHP	0.08	0.08	-	-	-	-	2.13	-	-	-	-	0.42	-	-	50.75	0.71	17.45	175.76	-	0.99	-	13.27	363.54	3.2	0.14	-	131.62	-
CAR	-	-	0.02	-	-	-	-	-	-	-	0.25	-	18.38	18.36	-	-	-	-	11.28	-	-	-	-	-	-	-	138.19	-
DET	-	-	0.38	-	-	-	1.09	-	-	-	-	-	-	27.53	0.91	0.01	1.59	-	191.82	37.62	212.41	13.27	-	303.53	0.42	-	-	-
Import	-	-	-	-	-	-	-	-	-	-	-	-	-	-	-	-	-	-	-	-	-	-	-	-	-	-	-	-
Sum	0.14	0.14	0.45	0.03	0.01	0.01	6.5	5.54	12	8.54	8.32	41.55	45.88	91.74	90.63	1.2	31.73	251.09	225.66	39.6	212.41	88.34	363.54	319.51	1.13	163.38	800.1	-

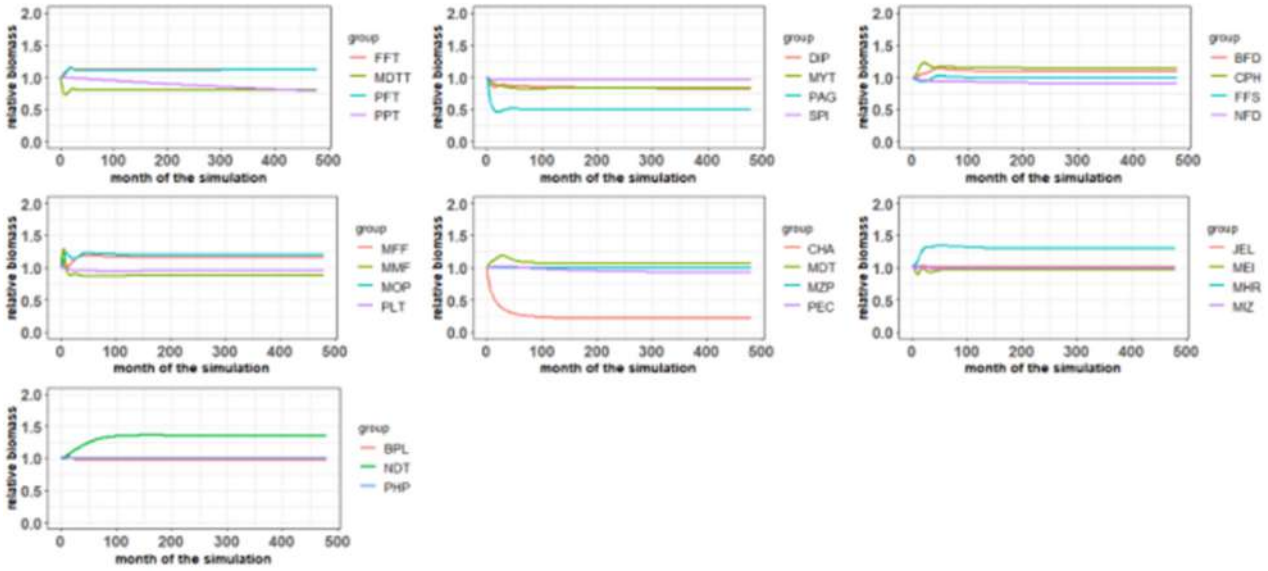

Figure 65. Relative biomass trends for trophic groups following spatialization in Ecospace. After an initial biomass adjustment, the network reaches a steady state, where the biomass variation is zero.

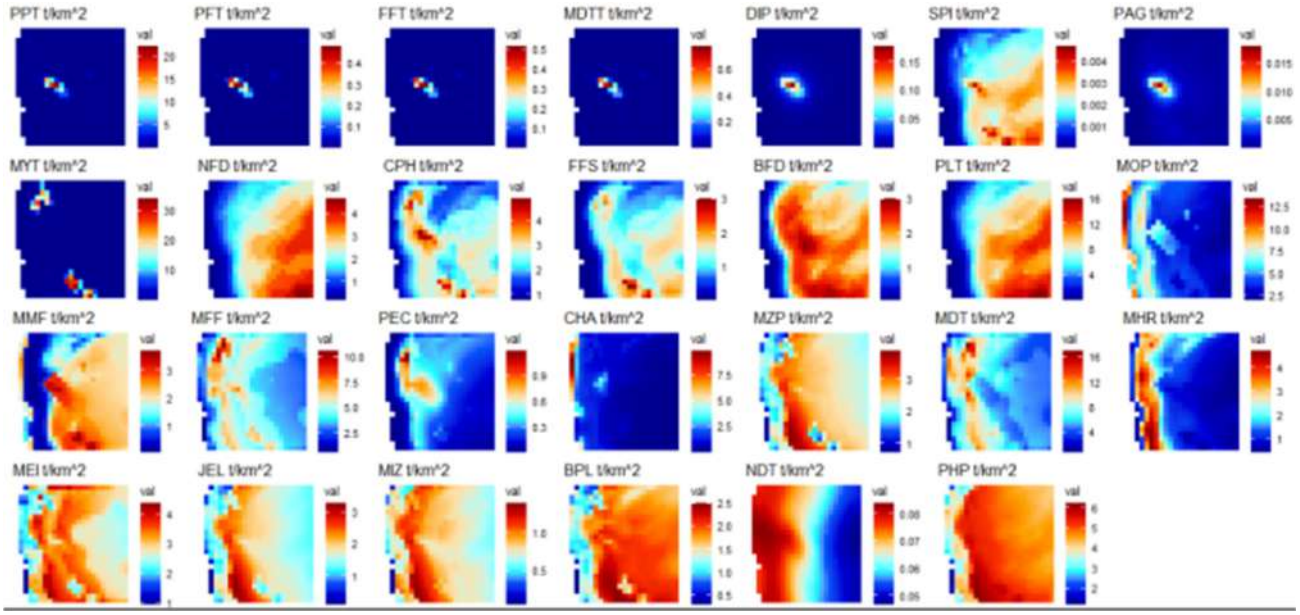

Figure 66. Absolute biomass maps for trophic groups following spatialization in Ecospace.

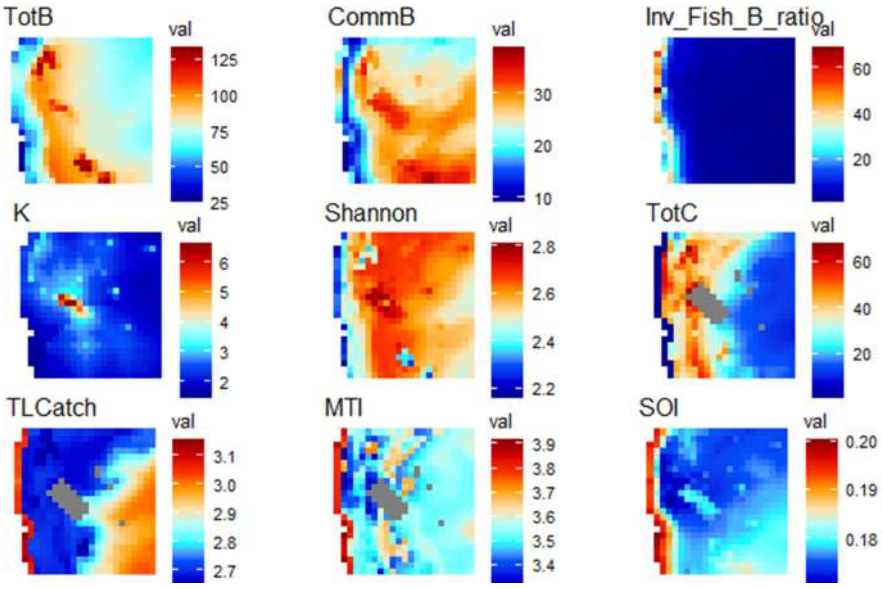

Figure 67. Absolute values for ecosystem indicators with baseline scenario at steady state.

From Figure 68 the highest biomass values occur near the reefs. Most of the invertebrates are in the sub-coast within 3 miles, while the distribution of commercial biomass is the opposite. Nevertheless, most catches are concentrated in areas closer to the coast.

3.4.9 Corroborations

The average correlation for otter trawl was 0.70 with 100% significant correlations. However, this value is reduced to 0.36 (97.5% of significant correlations) when cells with 0 effort are not considered (Table 20). It can therefore be deduced that the fishing effort simulated by the base model in Ecospace is only partially positively correlated with the fishing effort data obtained through the Automated Identification System (Russo *et al.* 2020). In the case of the Rapido, the average correlation was 0.45, with 100% of the correlations significant, but it dropped to just 0.17 (37.1% significant correlations) when only cells with positive effort values were considered.

Table 20. Results of model corroboration analysis, performed on otter trawl and beam trawl catches.

Cor.test() results for Volante Fleet

	mean_cor	sign_percentage
No land cells	0.70	100.0
No land + no empty cells	0.36	97.5

Cor.test() results for Rapido Fleet

	mean_cor	sign_percentage
No land cells	0.45	100.0
No land + no empty cells	0.17	37.1

3.4.10 Model application: exploration of management proposals through Multi-criteria analysis

Although the variability of the proposed indicators for each criterion, calculated for each region, is minimal, the multi-criteria analysis approach, even without prioritization of criteria and/or indicators, has made it possible to rank the management proposals, comparing the Final Scores with each other and with the base scenario (Table 21). The opening to artisanal fishing within the SCI during the winter period does not show significant differences in the performance of the proposed indicators (base FS = 3.87, artisanal fishing FS = 3.87). Interestingly, however, the expansion of the SCI produces a maximization of fishing performance (val = 1), when compared with the base and artisanal fishing scenarios, while a reduction in the performance of the *C. gallina* criterion (val = 0.88). The first observation is probably due to the so-called spill-over effect produced by marine protected areas, according to which an increase in the biomass of fish in the protected area and the consequent removal of some specimens from its boundaries would promote higher catches by fishing fleets. On the other hand, the decline in the performance of the criterion *C. gallina* is attributable to both a decline in biomass in Region 4 and a decline in catch. The decline in biomass may be produced by an increase in predator biomass due to the marine protected area effect, while the decline in catch can be attributed to the no-take-zone effect induced by the expansion of the SCI area into the sub-shore, where clam boats normally operate. Overall, results suggest the interest in applying this type of analysis for comparing scenarios

produced by alternative management choices. Nonetheless, given the restricted difference in the values calculated for the different indicators in the regions considered, it seems of relevance to extend the effort, by performing an uncertainty analysis of the results obtained.

Table 21. Values of the indicators estimated in the different regions, under the 3 scenarios considered (baseline + 2 scenarios of change).

	scenario	Bcha	Ccha	Bfish	Cfish	Bmyt	Btegnua	TotBSIC	K	MTI	SOI
Region1:SIC	base	-	-	-	-	-	1.16	123.51	2.833	3.591	0.175
Region2:MYT	base	-	-	-	-	7.09	-	-	2.414	3.587	0.178
Region3:FISHING	base	-	-	18.42	4.28	-	-	-	2.158	3.586	0.176
Region4:CHA	base	2.5	1.91	-	-	-	-	-	2.209	3.584	0.183
Region1:SIC1	expSIC	-	-	-	-	-	1.16	123.87	2.799	3.589	0.174
Region2:MYT1	expSIC	-	-	-	-	7.07	-	-	2.413	3.588	0.179
Region3:FISHING1	expSIC	-	-	18.38	5.07	-	-	-	2.157	3.588	0.177
Region4:CHA1	expSIC	2.19	1.69	-	-	-	-	-	2.203	3.585	0.183
Region1:SIC2	fishSIC	-	-	-	-	-	1.16	123.48	2.834	3.591	0.175
Region2:MYT2	fishSIC	-	-	-	-	7.09	-	-	2.414	3.587	0.178
Region3:FISHING2	fishSIC	-	-	18.43	4.29	-	-	-	2.158	3.586	0.176
Region4:CHA2	fishSIC	2.5	1.91	-	-	-	-	-	2.209	3.584	0.183

Table 22. Intermediate-level values for the different criteria, and final score achieved under the three scenarios considered.

Scenario	Criteria	St.indicators	Final scores
Base	Nature	0,95	3,87
	Fishery	0,92	
	Mussels	1	
	Clams	1	
Artisanal fishing in SCI in winter	Nature	0,95	3,87
	Fishery	0,92	
	Mussels	1	
	Clams	1	
Expansion of the SCI area	Nature	0,95	3,83
	Fishery	1	
	Mussels	1	
	Clams	0,88	

3.4.11 Model application: climate change and management combined effects

Modelling activities performed reported a high sensitivity of food web indicators to changes in water temperature and primary production phenology in the area. Results obtained (Figure 69)

from the model suggest that, overall, fishery pressure have a more confined impact with respect to climate induced pressure on food web functioning indicators. Nonetheless, a sensitivity to a reduced fishery pressure is visible in specific indicators (total catch, System Omnivory Index). Further model testing is required, by extending the set of scenarios considered (i.e., changes in fishery pressure in the area) and including the estimation of additional ecological network analysis indicators (e.g., Finn cyclic index). Further development of modelling activities in the area should also include an uncertainty analysis of the results.

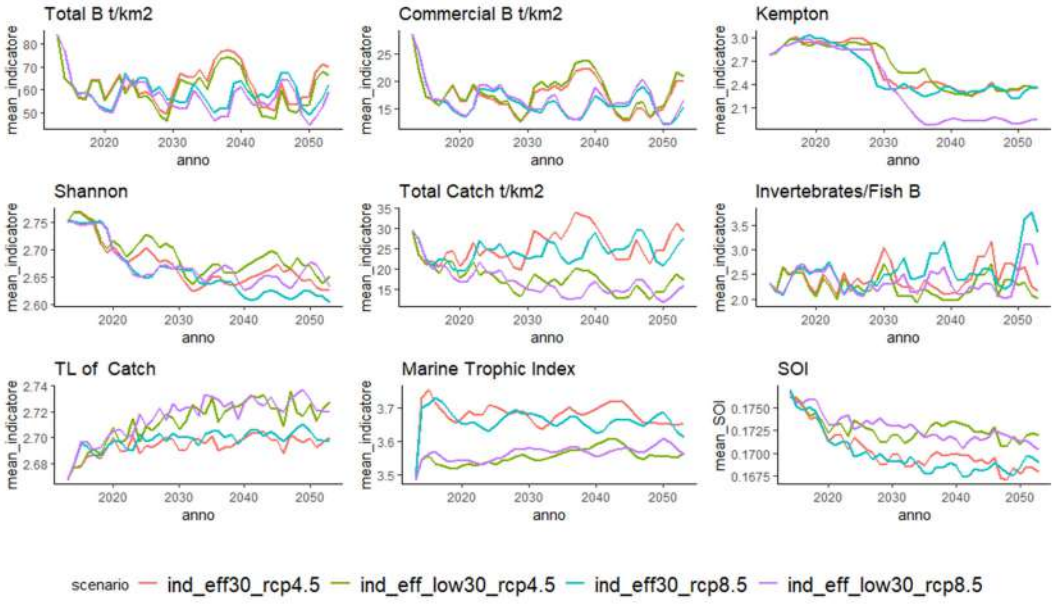

Figure 68. Food web model at Tegnùe di Chioggia area. Forecasted indicators of food web functioning under climate change and fishery pressure scenarios (ind_eff: increase in fishery pressure in the surroundings of the SCI; ind_eff_low: decrease in fishery pressure in the surroundings of the SCI).

3.5 Miljašić Jaruga river mouth, Nin bay (HR)

Numerical model was implemented for the purposes of analysing the flow in the Nin Bay and the section of the Miljašić Jaruga river under the conditions of the current state of construction and under the conditions of the planned state of construction with the arrangement of the Miljašić Jaruga river according to the project solution defined by DUEL PROJEKT (2019). The model of the current state of construction was established and parameterized based on measured water temperature/salinity data, sea currents data, sea level data, discharge/level data in the measurement section of the Miljašić Jaruga river, and wind speed/direction data from open data sources. Numerical simulations of flow in the existing state of construction were carried out for

three basic scenarios, which are associated with extremely high sea levels with return periods of 5 and 100 years. Data on extremely high sea levels were obtained from statistical processing of numerical model simulation results of sea circulation for the entire Adriatic basin during the period 1991-2021, and measured sea levels at tide stations along the Croatian coast in the same period.

3.5.1 Modelling approach

The numerical model Mike 3fm is used to model the circulation in the Bay of Nin and the flow of the Miljašić Jaruga river. This model is based on the flexible mesh approach, and its hydrodynamic module solves the 3D RANS equations using the Boussinesq and hydrostatic approximations. The model uses a free surface, and vertical model discretization is carried out using the standard sigma coordinate approach Song et al. (1994). Governing equations are solved within a finite volume frame, based on a single cell division and continuum discretization with non-overlapping elements Sleigh et al. (1998). An unstructured mesh is used in the horizontal and a combined sigma-z structured mesh in the vertical direction. An approximate Riemann solver (Roe, 1981; Toro, 1997) is used to calculate convective terms, enabling computation in cases of discontinuous solutions with steep gradients. For time integration, the model uses a semi-implicit approach – explicitly in the horizontal and implicitly in the vertical. The Smagorinsky scheme (1993) and *k-ε* model (Rodi, 1987) are used for turbulence closure formulation in the horizontal and vertical directions, respectively.

3.5.1.1 Spatial domain of the model

The numerical model spatial domain shown in Figure 70 was selected for the purpose of modelling the Miljašić Jaruga river flow as well as the sea circulation in Nin Bay. The open boundaries of the model are indicated by black lines. Solid boundaries correspond to the contact line of water with the line of the "natural" or "artificial" coast. These boundaries are impermeable and there is no flux through them.

The bathymetry was obtained based on free available nautical charts (www.navionics.com, Figure 70), and by applying bilinear interpolation for the positions of numerical nodes where there are no defined depths. The depth data for the part of the Miljašić Jaruga river up to the station 0+435m, presented within the scope of the conceptual solution project Duel Project (2019) (Figure 71), were used in the numerical simulation for the current state of construction. For the simulation scenarios in the planned state of construction, the depth data presented in Duel Project (2019) were also used, with characteristic sections shown in Figure 71. The designed solution described in the Duel Project (2019) was extended and complemented with the variant solutions of the planned state of construction of the Miljašić Jaruga river mouth Carević et al. (2021). This study will focus on the

variant solution which considers both groynes at the Miljašić Jaruga mouth designed as vertical wall type surrounded with sloped rock armour (Figure 72).

The model spatial domain is discretized with an unstructured mesh of finite volumes where triangular elements are used to describe the seabed and quadrilateral elements for the river geometry (Figure 73). The spatial increment between the numerical nodes, located in the centre of each finite volume, is variable, from 3 [m] in the river of the Miljašić Jaruga to 65 [m] in the area of the greatest depths of Nin Bay. In the vertical direction 5 sigma layers with a thickness of 1 [m] up to a depth of -3 [m] were used, and below it a "z" coordinate with a cell thickness of 1 [m].

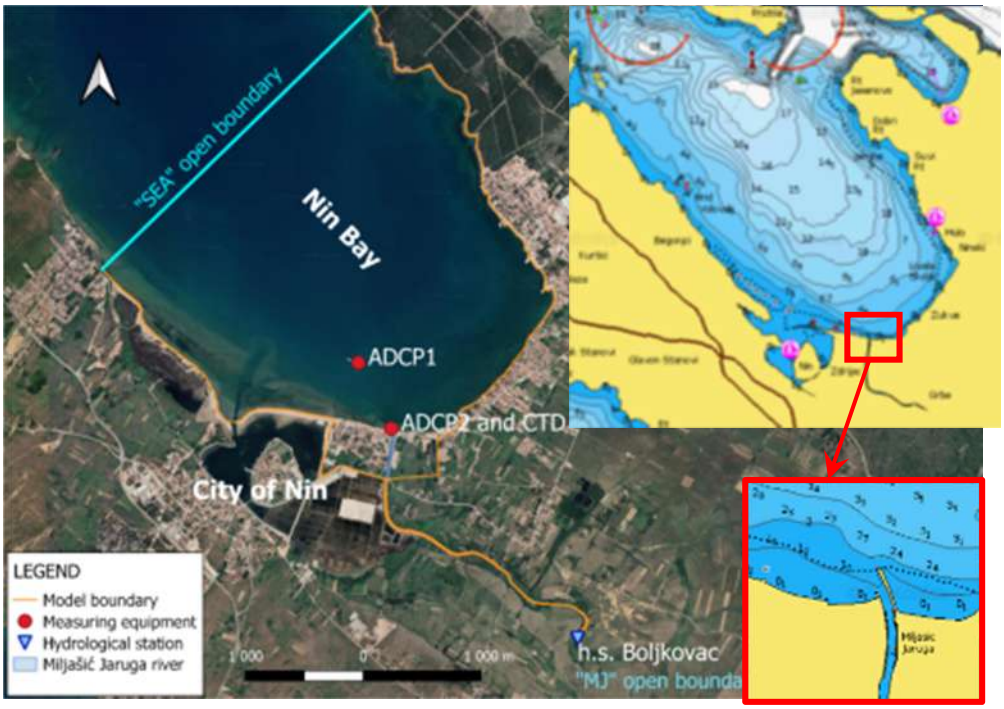

Figure 69 The study area plan view with a bathymetric base of Nin Bay and extracted detail of bathymetry downstream of Miljašić Jaruga river mouth used for defining the model bathymetry within the bounds of spatial domain of the numerical model, locations of deployed ADCPs and CTD probe during field measurement campaign, and a location of hydrological station Boljkovac

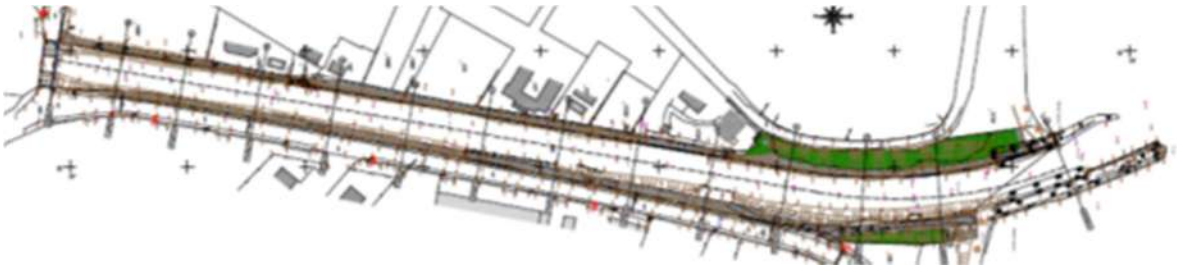

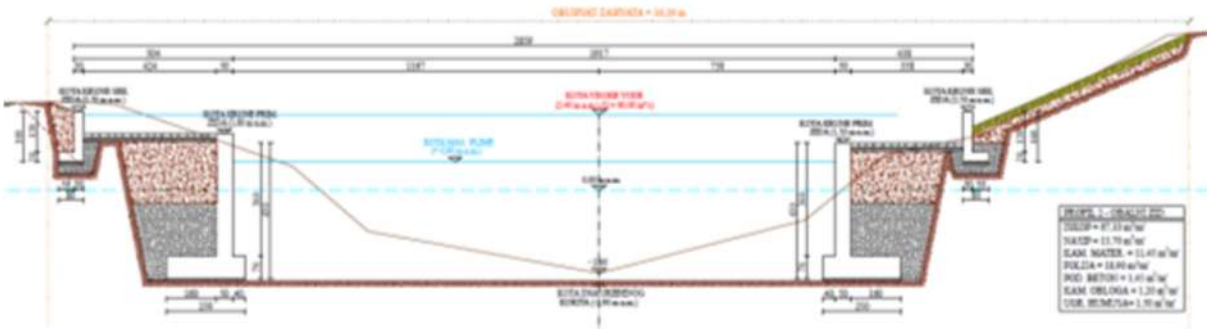

Figure 70 The ground plan with depths in the current state of the Miljašić Jaruga up to the station 0+435m and the characteristic section 2 (0+120.73) in the planned state of construction.

Figure 71 The analysed variant solution of Miljašić Jaruga river mouth (variant 3 - both groynes as combination of vertical wall type and sloped rock armour)

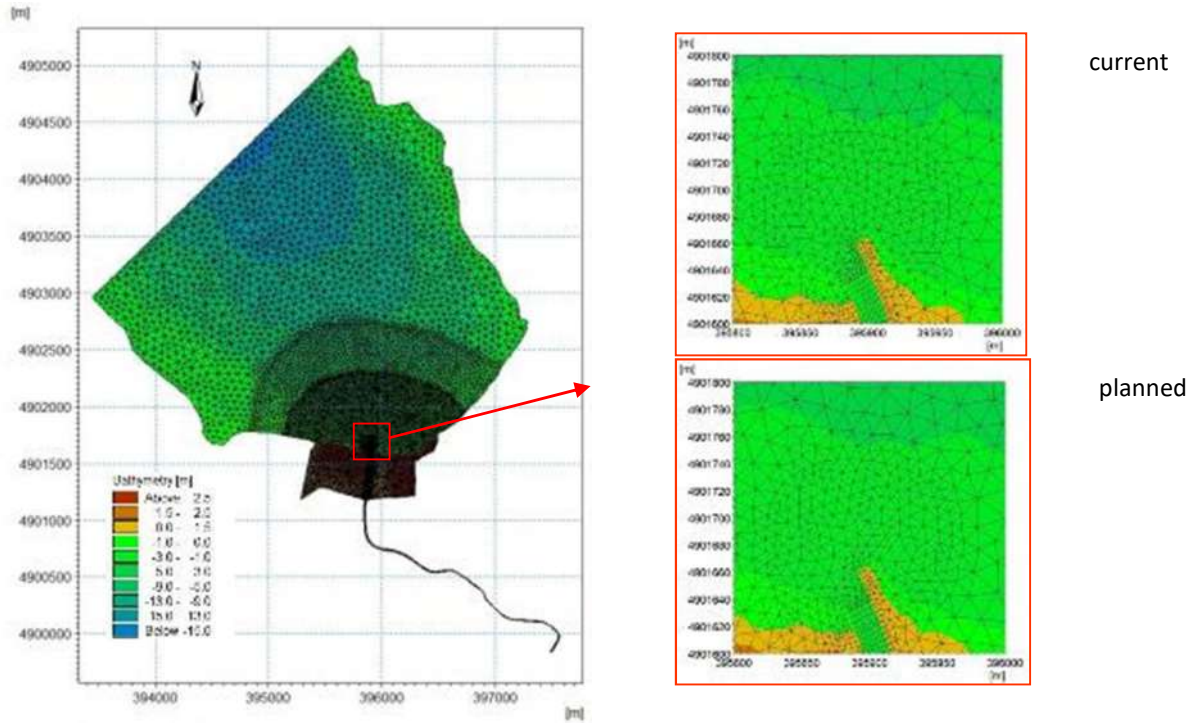

Figure 72 The area covered by the spatial domain of the numerical flow model (applied model discretization with triangular and quadrilateral finite cells-volumes on a bathymetric base) with details of Miljašić Jaruga mouth in current (up right) and planned state of construction (down right)

3.5.1.2 Initial/boundary conditions and model parametrisation

3.5.1.3 Simulations for current state of construction

In the analysis related to the current state of construction a combination of the estimated and recorded sea level dynamics was imposed on the open boundary "SEA" during the period December 11th, 2022 – February 2nd, 2023 (74). The estimated component was defined as a combination of the tidal constituents for the Zadar location (Janeković and Kuzmić, 2005) and sea level residuals obtained from the results of the NEMO-v3.6 oceanographic model developed and operated by Copernicus Marine Service (Escudier et al., 2020). Such sea level dynamics was defined for the period between the simulation start and field measurement campaign start (December 16th, 2022). The previously described data were supplied with the recorded sea level time series from the results of the measurements at the station ADCP1 (Figure 70).

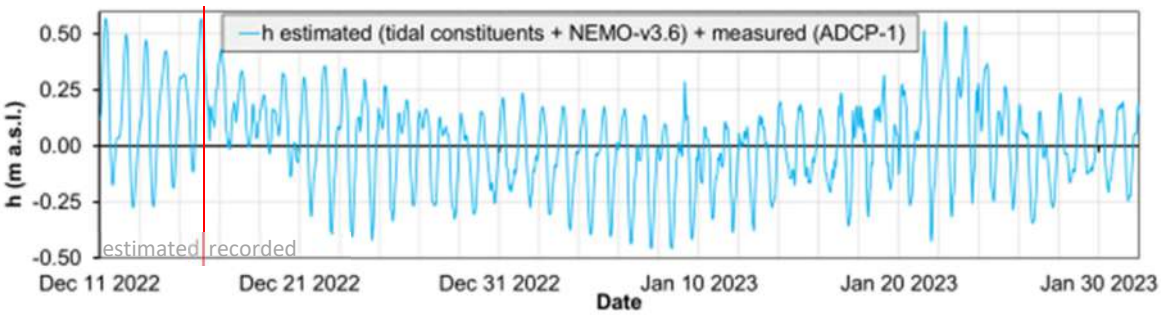

Figure 73 Time series of sea levels defined at the numerical model open boundary condition "SEA" during the period December 11th, 2022 – February 2nd, 2023 (combination of the estimated and recorded sea level dynamics, Figure 70)

Numerical integration started on December 11th, 2022, at 10 AM, by initiation with the sea temperature (T) and salinity (S) fields obtained from NEMO-v3.6 oceanographic model (Escudier et al., 2020). The vertical profile of temperature and salinity at the date mentioned above were imposed as an initial condition the open boundary "SEA". Furthermore, the model was forced with the T and S fields according to the hourly vertical distributions of the two parameters from the results of the NEMO v3.6 model between December 11th, 2022 and February 2nd, 2023, see (Figure 75 – Figure 77).

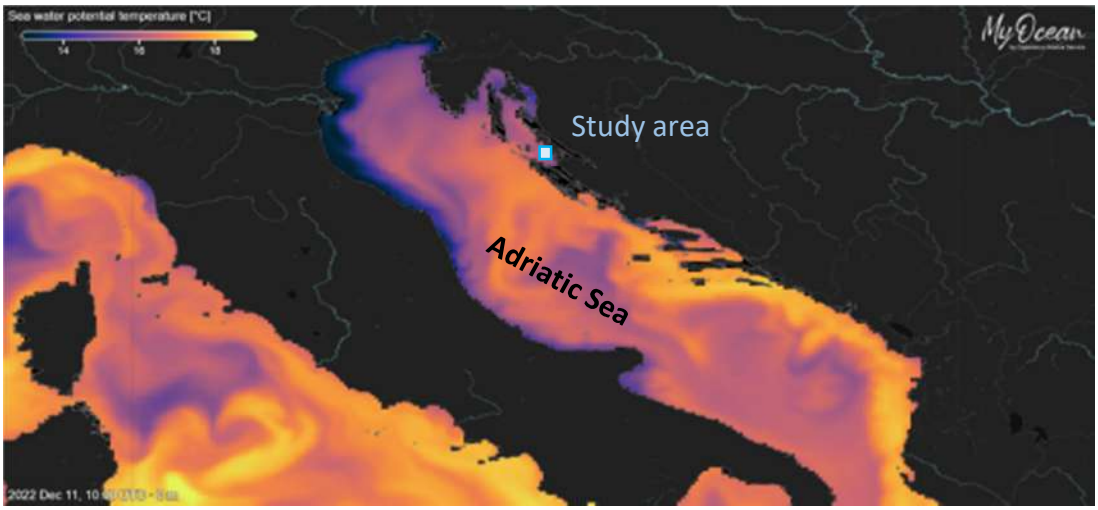

Figure 74 Sea temperature (up) and salinity (down) fields for December 11th, 2022, in the surface layer for the area of the entire Adriatic based on the results of NEMO-v3.6 model

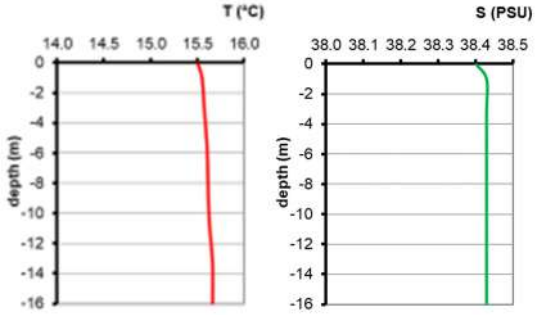

Figure 75 Vertical profile of sea temperature (left) and salinity (right) for December 11th, 2022, defined as initial condition at the open boundary "SEA" for the initiation of numerical model simulation for current state based on the results of NEMO-v3.6 model

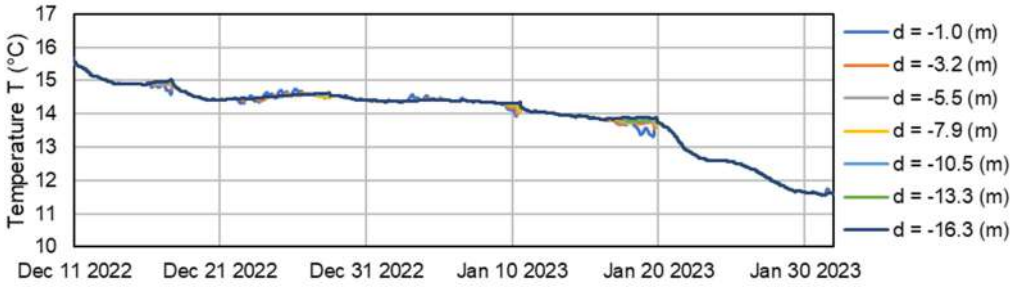

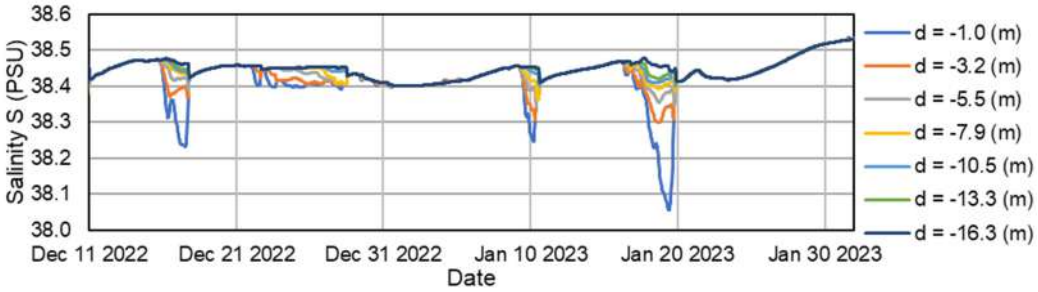

Figure 76 Hourly time series Vertical distributions of sea temperature and salinity at the edges of "SEA" open boundary in terms of Dec 11th, 2022, and Feb 2nd, 2023, according to results of NEMO-v3.6 model

A homogeneous and non-stationary wind field was applied at sea-atmosphere interface during the period of numerical simulations for the current state of construction. The displayed values (Figure 78) refer to 30-minute averages for the location of Zadar-Zemunik airport.

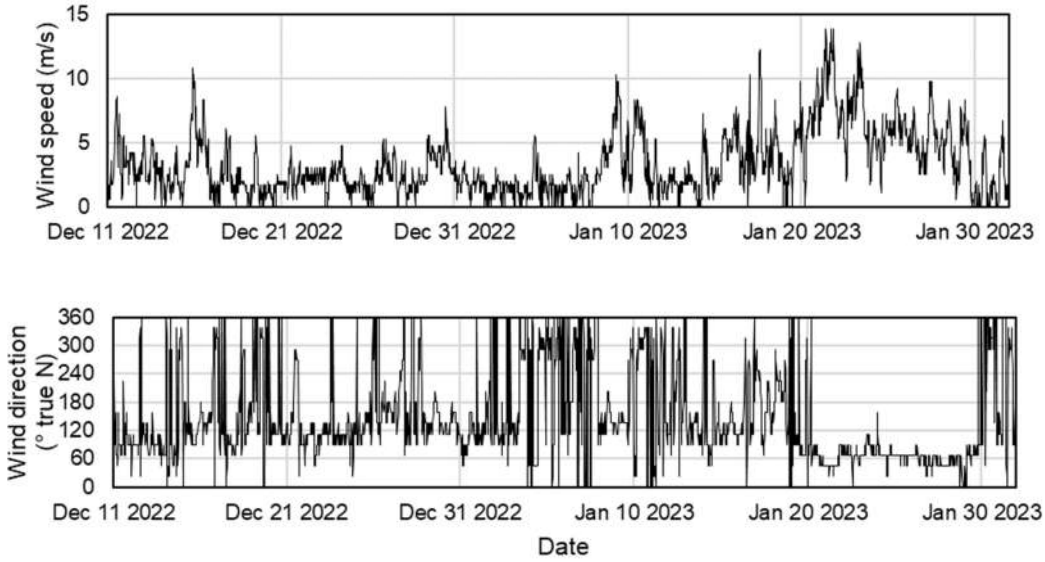

Figure 77 Time series of wind speed (above) and direction (below) on location of Zadar-Zemunik airport during the period of numerical simulations for the current state of construction (Dec 11th, 2022-February 2nd, 2023)

At the open boundary "MJ" model is forced with hourly discharge time series at hydrological station Boljkovac (see Figure 70) in the period between December 11th, 2022, and February 2nd, 2023. The time series of water level up to January 13th, 2023 were delivered by Hrvatske vode – Croatian national authority for water management. A discharge was calculated based on the historical rating curves up to the mentioned date while the rest of the discharge time series were estimated based on the velocity measurements and cross section data at the ADCP2 location. Water temperature is

defined according to measured time series of temperature ADCP2 station in hourly resolution (Figure 75) while salinity was defined as a constant of 0 PSU during the whole simulation period.

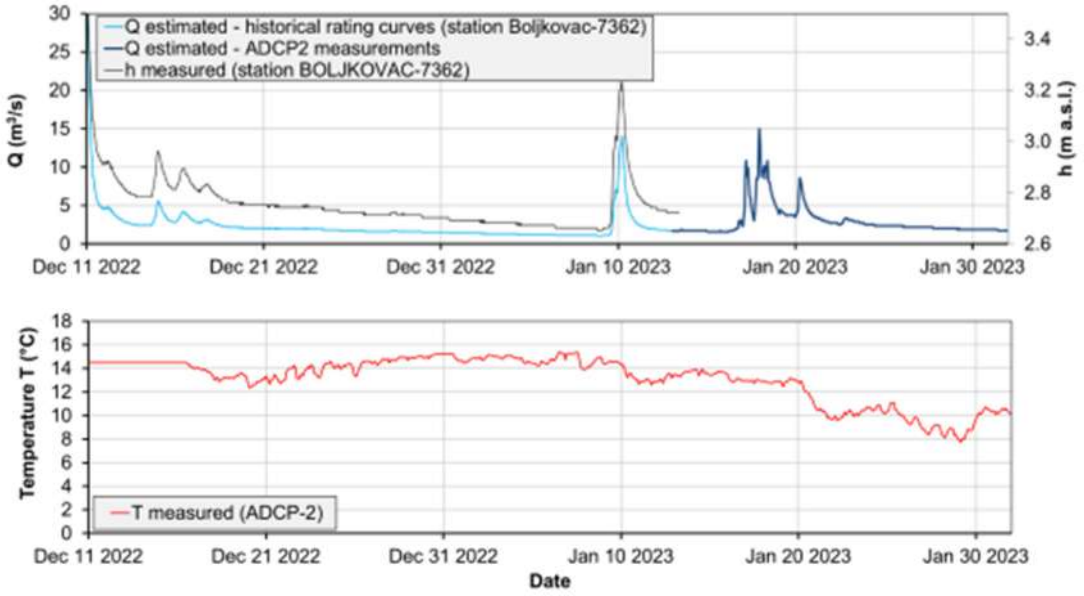

Figure 78 Hourly water level and estimated discharge at the hydrological station Boljkovac (above) with and water temperature/salinity at the locations ADCP2 (below) for the period December 16th, 2022 to February 2nd, 2023

Simulations were run using the following parameter values: minimum time step of external mode *Dt*=0.1 s, maximum time step of internal mode *Dt*=30s with a critical threshold Courant-Friedrich-Levy (CFL) number of 0.8. Dispersion coefficients for the scalar *T*, *S* fields were defined as proportional to the scaled eddy viscosity with factors 0.1 in the vertical and 1.0 in the horizontal. proportionality factors for the dispersion coefficients of turbulent kinetic energy *(TKE)* and dissipation of TKE (*e*) were used with the values 1 for the *TKE* and 1.3 for the horizontal and vertical directions. Smagorinsky coefficient was set as spatially and temporally constant value of 0.2. The value of 0.0013 (Wu, 1994) was used for the wind friction coefficient.

Hydrodynamic model uncertainty is examined by the Pearson correlation coefficient (*R*), the corrected indicator *HH* proposed by Hanna and Heinold (1985), the normalized bias (*NBIAS*), and the normalized root mean square error (*NRMSE*), defined in equations (1)-(4), respectively:

$$R = \frac{\sum_{i=1}^{N}\left(\left(P_i-\overline{P}\right)\left(O_i-\overline{O}\right)\right)}{\left[\left(\sum_{i=1}^{N}\left(P_i-\overline{P}\right)^2\right)\left(\sum_{i=1}^{N}\left(O_i-\overline{O}\right)^2\right)\right]^{1/2}} \quad (1)$$

$$HH = \sqrt{\frac{\sum_{i=1}^{N}(P_i - O_i)^2}{\sum_{i=1}^{N} P_i O_i}} \quad (2)$$

$$NBIAS = \frac{\overline{P} - \overline{O}}{\overline{O}} \quad (3)$$

$$NRMSE = \sqrt{\frac{\sum_{i=1}^{N}(P_i - O_i)^2}{\sum_{i=1}^{N} O_i^2}} \quad (4)$$

where P_i is the ith prediction, O_i the ith observation, the overbar refers denotes the mean values, as in $\overline{P}$ is the mean of all prediction values, and $\overline{O}$ is the mean of all observation values. HH is generally recommended when quantifying dispersion errors because it is unbiased toward simulations with negative biases, which contrasts with normalized root mean square error (*NRMSE*) and its variants (Mentaschi, 2013). For both *HH* and *NRMSE* performance indicators, a larger value indicates a higher dispersion error, while a lower value points to a lower dispersion error when comparing measured and modelled data. Both indicators are always non-negative and show perfect alignment between measured and modelled data at a value of 0.

An important calibration parameter is the roughness, especially in the section of the Miljašić Jaruga river. Adoption of the appropriate value for roughness was based on the comparison of measured and modelled sea levels at the Miljašić Jaruga river mouth (ADCP2 site, Figure 80). After the simulations conducted within the calibration procedure, the roughness value of 0.005 [m] was adopted.

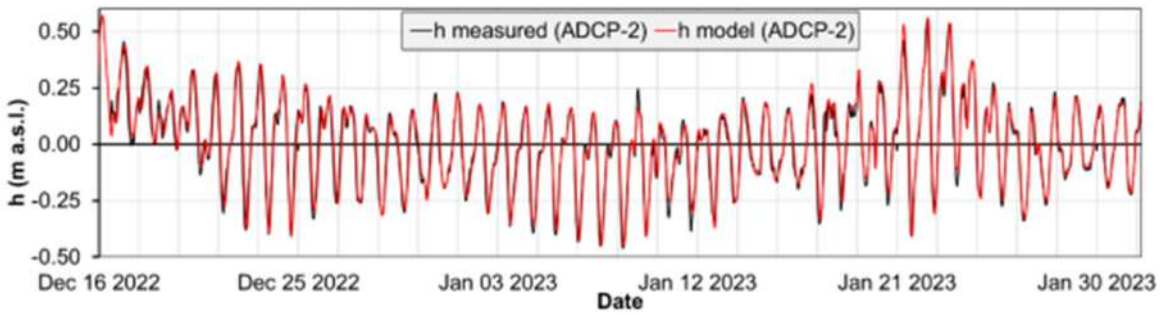

Figure 79 Time series of measured and modelled water level dynamics at the ADCP2 site for the measurement period Dec 16th, 2022 – Feb 2nd, 2023

Comparison of the measured and modelled time series of water temperature at the ADCP2 location for the measurement period December 16th, 2022, to February 2nd, 2023, is shown in Figure 81.

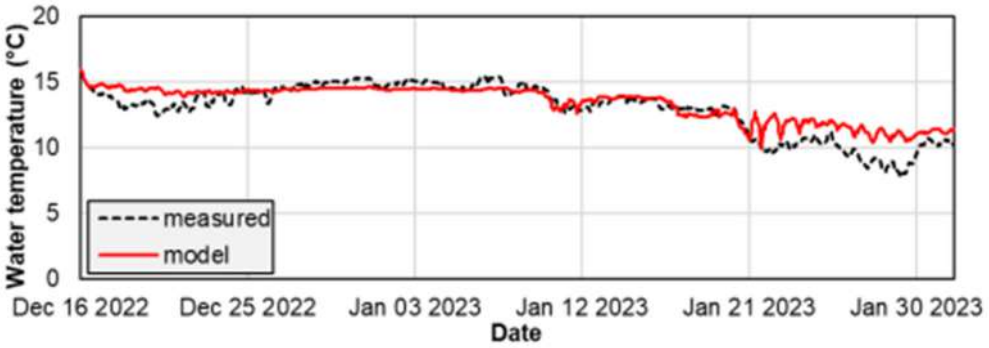

Figure 80 Time series of measured and modelled water temperature at the ADCP2 site for the measurement period Dec 16th, 2022 – Feb 2nd, 2023

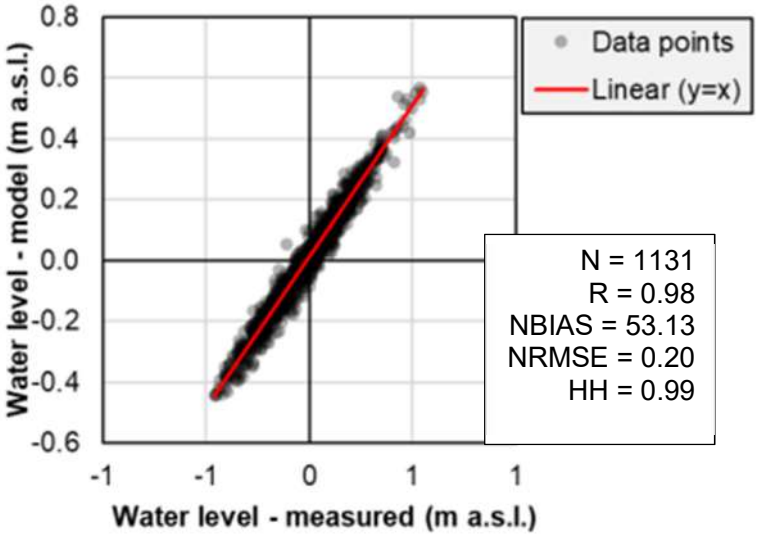

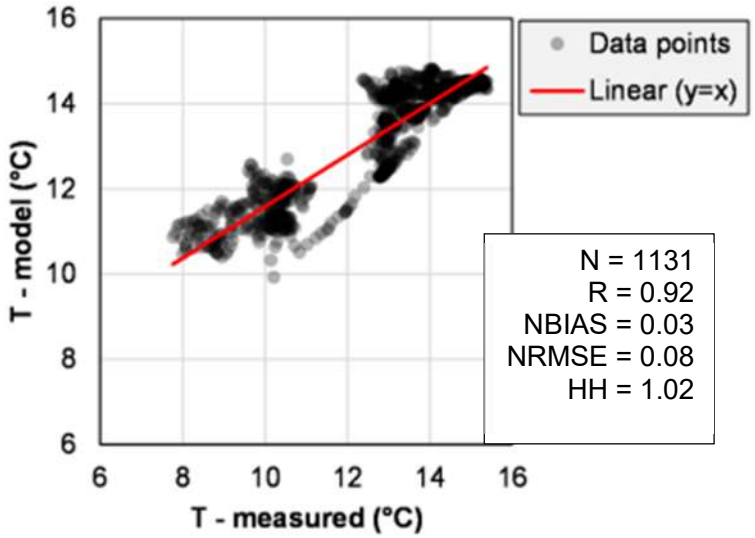

Figure 81 Scatter diagram and performance metrics showing the agreement between the simulated and measured water level (above) and temperature at depth of -2.5 m at the location ADCP2 during the period December 16th, 2022 and February 2nd, 2023

Model generally provides similar values of water temperature when compared to the measurements. However, the modelled temperature overestimates measured values in periods between December 16th and 20th, 2022 as well as after January 21st, 2023.

Measured values of current velocity components at ADCP1 and ADCP2 stations were also used for calibration control. Figure 83 – Figure 89 show comparisons of measured and modelled time series for the eastward U and northward V component of flow velocity at depths of -0.5 [m] and -1.5 [m], and depth averaged values, respectively. A detailed analysis of the measurements is conducted and presented in the deliverable D.4.1.1 which served as a basis for the calibration procedure of the flow velocities presented in the following graphs.

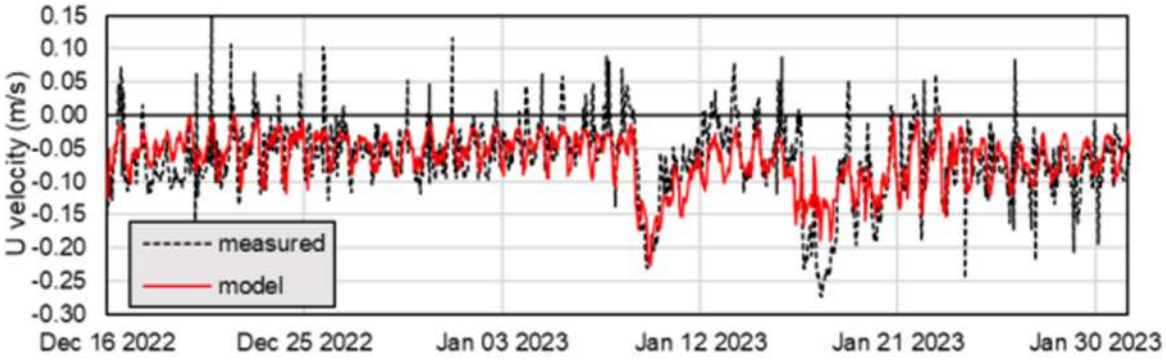

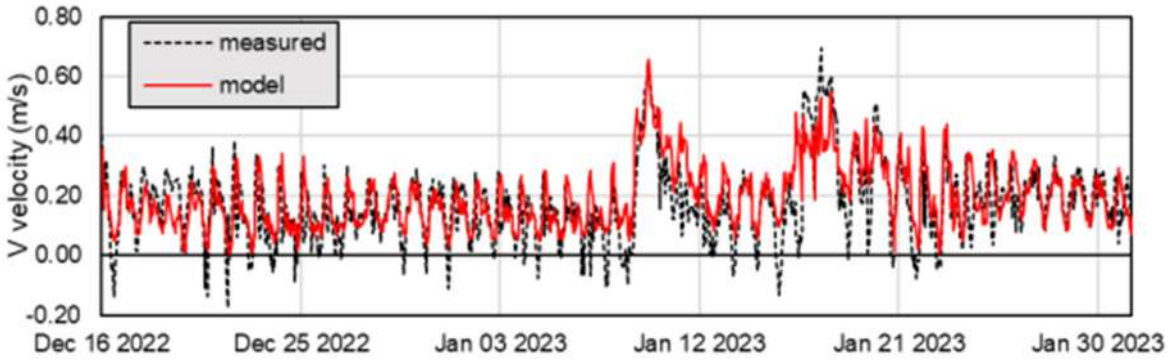

Figure 82 Comparison of measured and modelled hourly average current velocity components (eastward U and northward V) at a depth of -0.5 [m] for the position of ADCP1 site in the period of the numerical simulation December 16th, 2022 and February 2nd, 2023 (above - u component; below - v component)

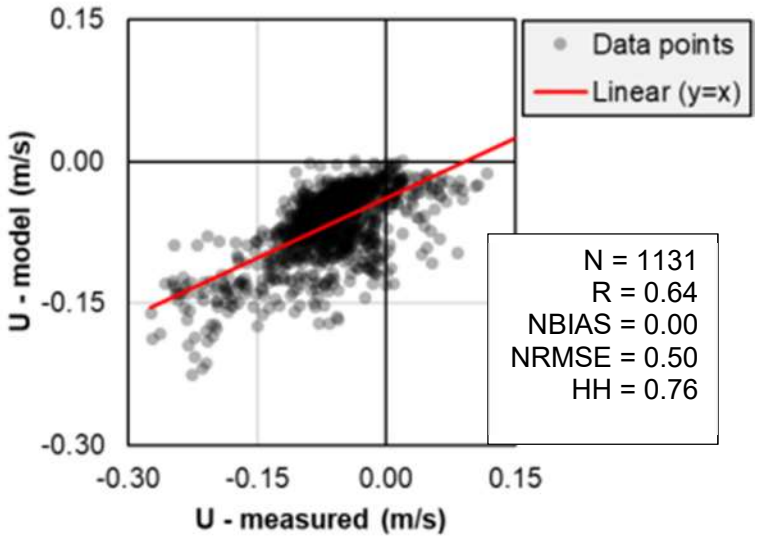

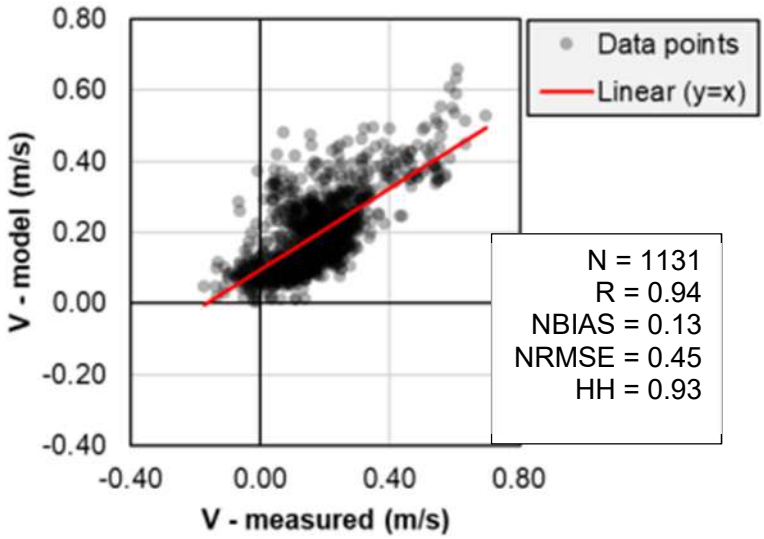

Figure 83 Scatter diagram and performance metrics showing the agreement between the simulated and measured eastward U (above) and northward V (below) flow velocity components at depth of -0.5 m at the location ADCP2 during the period December 16th, 2022 and February 2nd, 2023

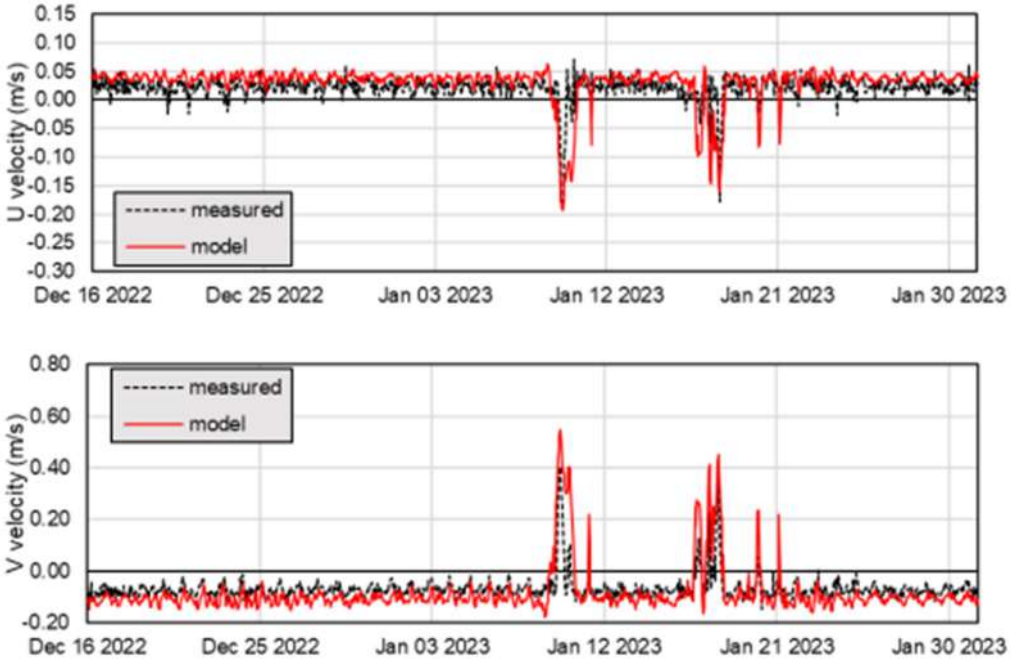

Figure 84 Comparison of measured and modelled hourly average current velocity components (eastward U and northward V) at a depth of -1.5 [m] at the location ADCP2 during the period December 16th, 2022 and February 2nd, 2023

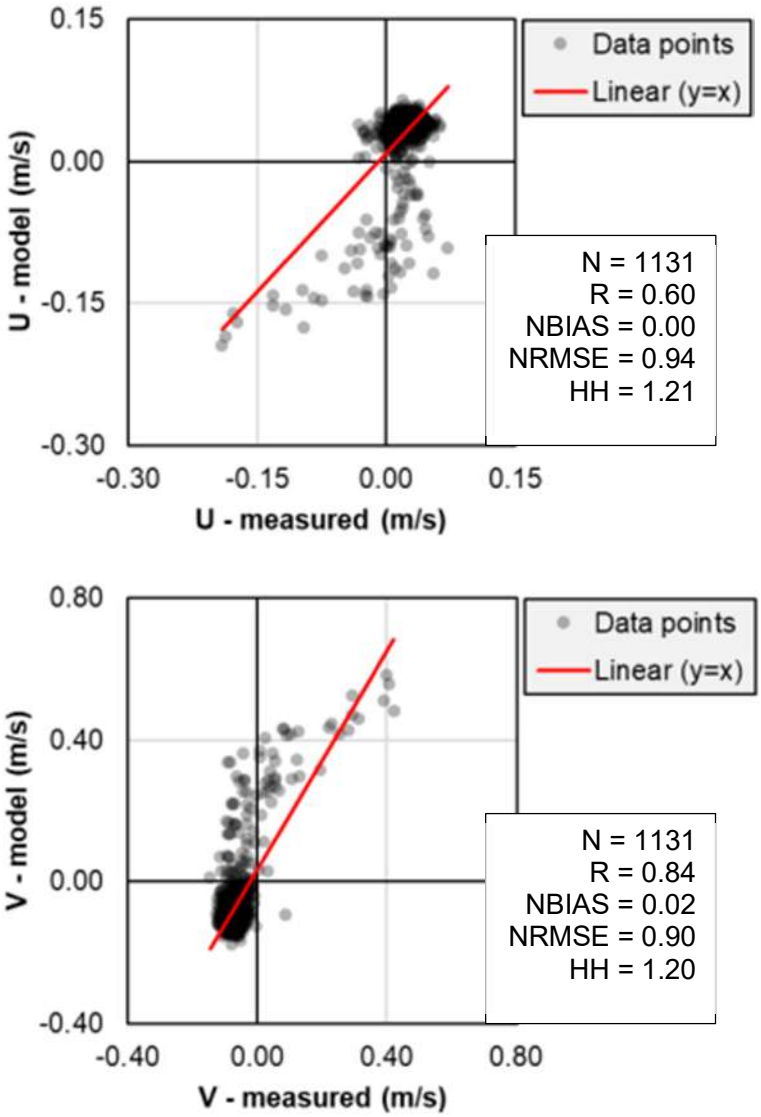

Figure 85 Scatter diagram and performance metrics showing the agreement between the simulated and measured eastward U (above) and northward V (below) flow velocity components at depth of -1.5 m at the location ADCP2 during the period December 16th, 2022 and February 2nd, 2023

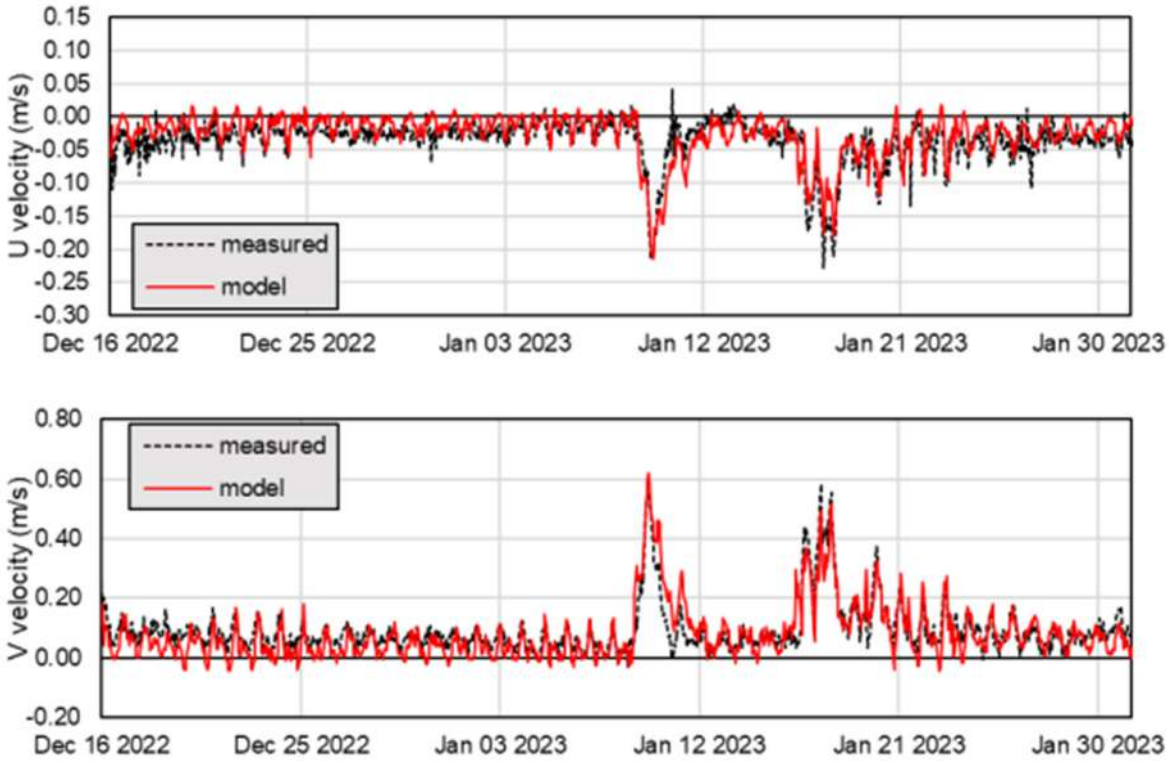

Figure 86 Comparison of depth averaged measured and modelled hourly average current velocity components (eastward U and northward V) at the location ADCP2 during the period December 16th, 2022 and February 2nd, 2023

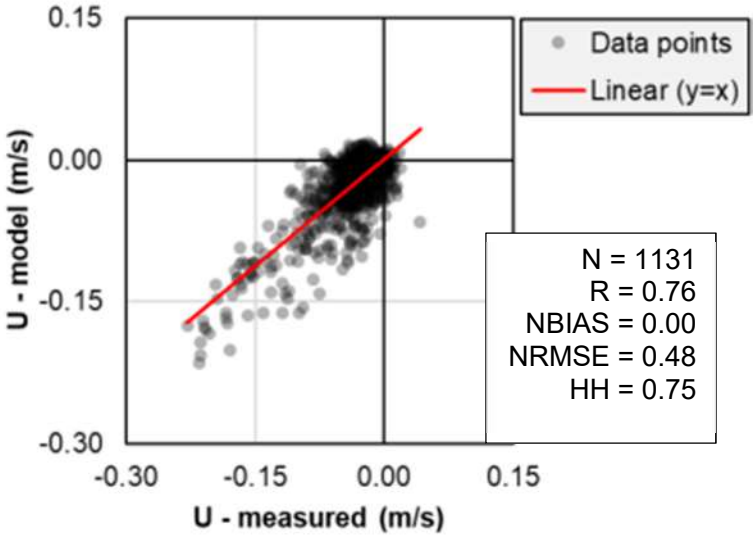

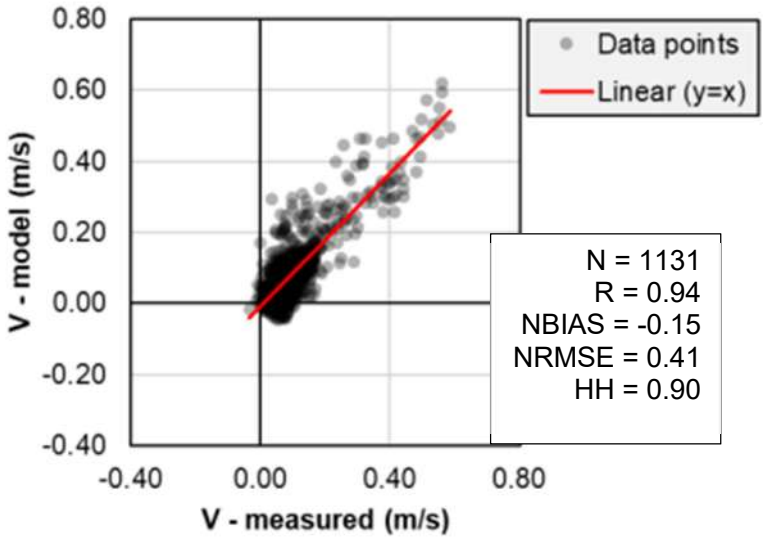

Figure 87 Scatter diagram and performance metrics showing the agreement between the simulated and measured eastward U (above) and northward V (below) depth averaged flow velocity components m at the location ADCP2 during the period December 16th, 2022 and February 2nd, 2023

Figure 78 - Figure 87 show that the model satisfactorily simulates the changes in U and V flow velocity components for the considered depths (-1.5 m and -0.5 m) as well as for depth averaged values. Below is presented a table which compares maximum, average and standard deviation of the modelled and observed velocities at depths of -1.5 and -0.5 m, and depth averaged values.

Table 23 Statistical parameters of the measured and modelled sea current velocities at depths -1.5 and -0.5 m, and depth averaged for the location ADCP2 in period Dec 2022 – Feb 2023

Depth	-1.5 m		-0.5 m		depth-avg	
	measured	model	measured	model	measured	model
Maximum velocity (cm/s)	45.6	59.4	74.6	68.4	62.8	66.0
Average velocity (cm/s)	8.2	11.7	19.5	18.6	13.3	18.0
Standard deviation (cm/s)	3.5	9.1	12.5	12.2	8.0	8.4

In average model overestimates the measured velocities what is seen from the Table 23 except for the subsurface layer (-0.5 m). Highest error in standard deviation of the modelled velocities occurs for the depth of -1.5 m while for depth averaged and depth of -0.5 m this parameter is similar to the values calculated based on the measurements. Modelled maximum velocities are

overestimated mostly at the depth of -1.5 m while at -0.5 m model underestimates the measured values. Depth averaged maximum velocity is higher for modelled than the measured values.

As the flow conditions during the measurement period did not cause the overbank flooding, additional analysis has been conducted related to the flood event that happened in September 2017 (further referred as Sep2017). Below is presented the discharge time series that was defined as the upstream boundary condition on the "MJ" open boundary. This hydrograph is replicated based on the graphical representation of the same flood event recorded on hydrological station Boljkovac presented in DUEL PROJEKT (2019).

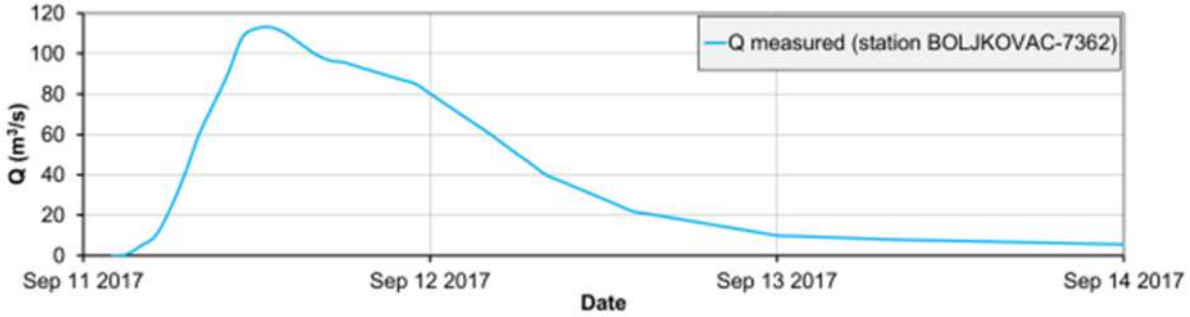

Figure 88 Discharge time series for September 2017 flood event imposed at "MJ" open boundary in hourly data resolution based on the reference [0]

The model was forced with a constant temperature of 10 °C and salinity of 0 PSU at the "MJ" open boundary while at the "SEA" open boundary constant temperature of 17°C and 38.5 PSU were imposed. Also, at the "SEA" open boundary the model was forced with sea level dynamics estimated as a superposition of tidal constituents for Zadar (Janeković and Kuzmić, 2005) and sea level residuals obtained from NEMO v3.6 model (Escudier et al., 2020). Wind was defined as a homogenous and nonstationary field according to 30-minute average speeds and directions for the location of Zadar-Zemunik airport.

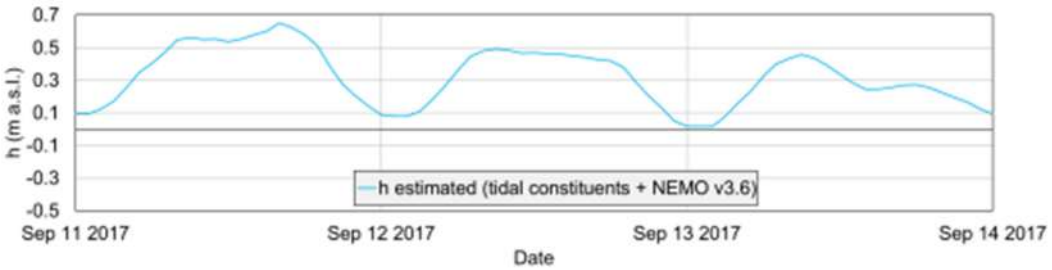

Figure 89 Hourly time series of sea levels defined at the numerical model "SEA" open boundary condition during the period September 11th-14th, 2017, (estimated based on the tidal constituents for Zadar and sea level residuals from the results of NEMO v3.6 model)

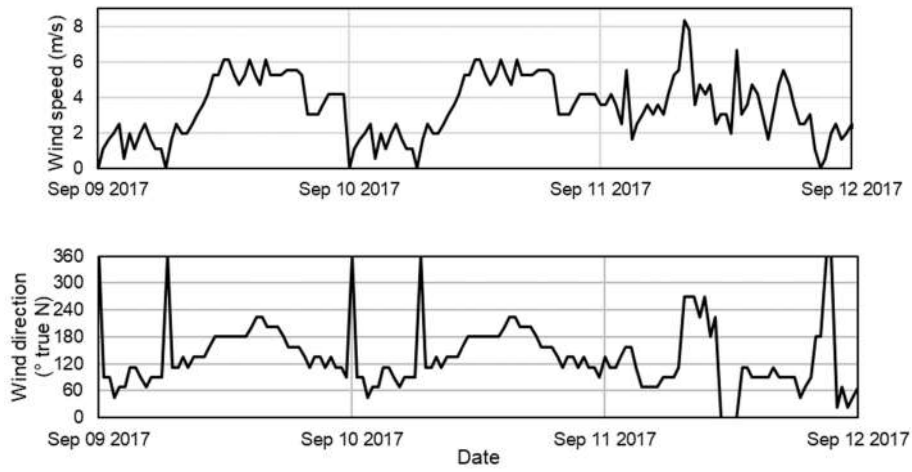

Figure 90 Time series of wind speed (above) and direction (below) on location of Zadar-Zemunik airport (www.wunderground.com/history/daily/hr/zemunik-donji/LDZD) during the period of numerical simulation of Sep2017 flood event for the current state of construction (Sep 9th – 12th, 2017)

The results will be presented through the comparison of the recorded flood extent at the moment of peak discharge of Q = 113 m^3/s. The flood extent was estimated based on the existing video record and the extent obtained from the hydrodynamic model what is presented below.

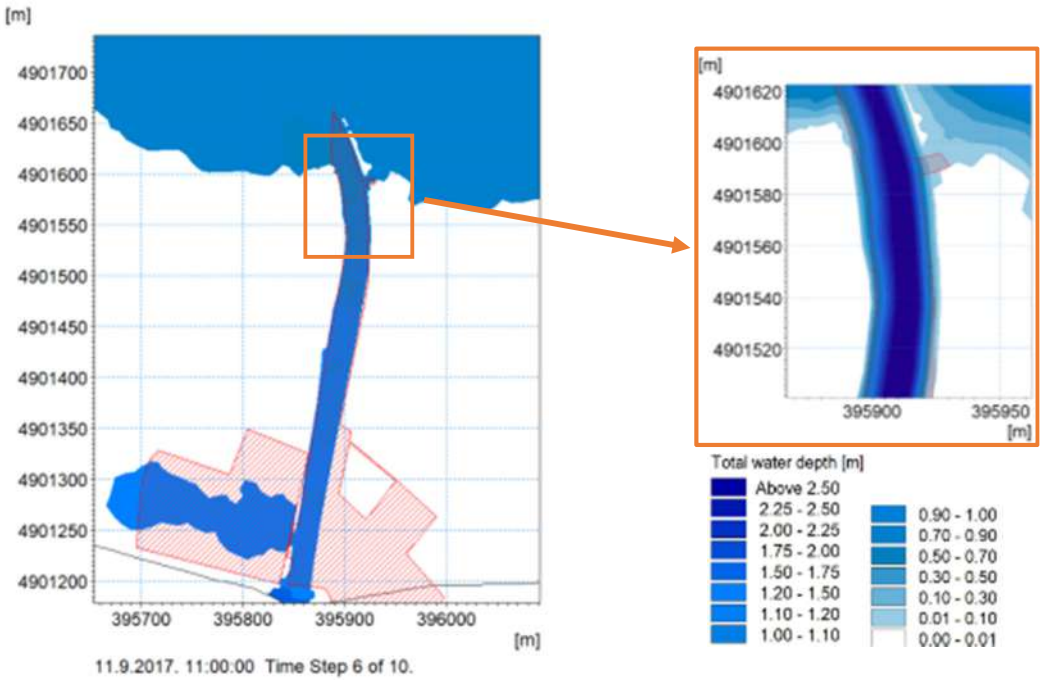

Figure 91 A comparison of estimated flood extent (left) based on the video record (red hatch) and extent obtained by hydrodynamic model (blue fill) with detail of total water depth field during the overbank flow upstream of the river mouth (right) for a peak discharge of Q = 113 m^3/ during flood event Sep2017

As it can be seen from the map above, the model successfully simulates the flooding of the left overbank area approximately 40 metres downstream of the road bridge during the Sep2017 flood event as well as right overbank flow approximately 20 meters upstream of the river mouth. The model failed to simulate the right overbank flow downstream the bridge. However, after inspecting the publicly available video recordings, it can be assumed that this area was flooded because the water approaching from the upstream sections, which were not covered by the domain of this model. Furthermore, it is important to note that the model results indicate that the bankfull discharge of the Miljašić Jaruga river at the analysed section is 99 m^3/s. The bankfull discharge represents a threshold value of discharge above which flooding occurs.

3.5.1.4 Simulations for future-planed state of construction

The Adriatic Sea is infamous for its storm surges (Cavaleri, 2000; Cavaleri et el., 2020). This relates to the northernmost Adriatic Sea, i.e., to Venice and the surrounding area where storm surges are known by a local name of Acqua Alta (It. High water) (Cavaleri, 2000). It is less known that high storm surges can flood and damage the eastern (Croatian) coast of the Adriatic Sea as well (Međugorac et al., 2015; 2018). Given the expected sea level rise of ~60 cm by the end of 21st century (IPCC, 2022), it is likely that events of extreme sea level will become more common and more intense and destructive. Šepić et al. (2022) were focused on analysing extreme sea level events recorded along the eastern (Croatian) coast of the Adriatic Sea. Hourly sea level data from 9 tide gauge stations spread evenly along the eastern Adriatic coast (Figure 93) were quality controlled; all spurious peaks were removed. Tidal oscillations were removed from sea level time series using procedure described in Medvedev et al. (2020). Three strongest sea level extremes per year were extracted for each station and Generalized Value Extremes (GEV) analysis (Tsimplis et al., 1997) was applied to estimate values of extreme sea level heights for periods from 2 to 1000 years. It should be noted that values for return periods longer than 100 years are likely non-reliable; mostly due to sea level and atmospheric forcing climate shifts that occur over longer time scales.

SCHISM ocean model (Zhang et al., 2016b) was used to reproduce selected episodes of sea level extremes. Ocean model was forced at surface by mean sea level pressure and 10-m wind fields originating from the ALADIN meteorological model run by Croatian Meteorological and Hydrological Service. Model outputs were compared with observations, and spatial distributions of extreme sea levels obtained from model were used to estimate spatial distributions of extreme sea levels for return periods of 25 and 100 years.

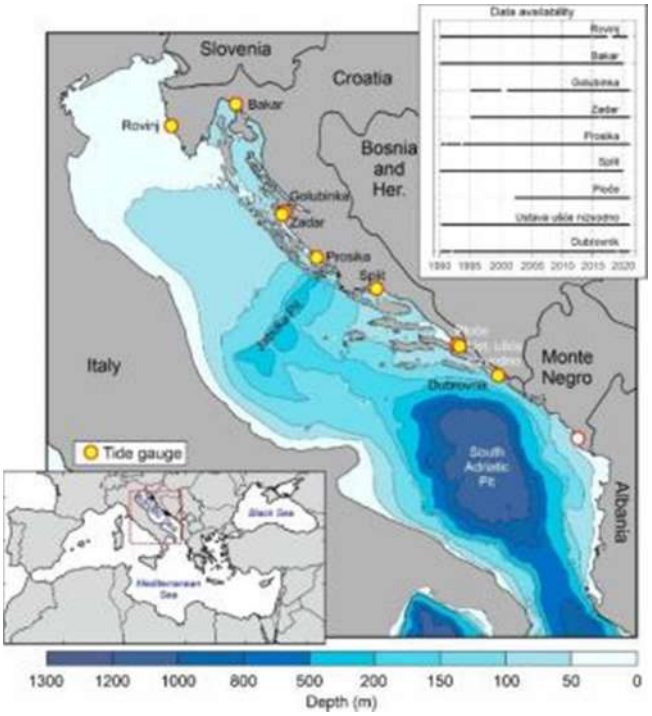

Figure 92 Study area with tide gauges marked with yellow circles and data availability is shown in the upper subplot

Results of GEV analysis, for return periods of 2 to 1000 years, are shown in (Figure 94-left). The most extreme values are estimated for the northern Adriatic (stations Bakar and Rovinj), and the least extreme for the middle and southern Adriatic (Dubrovnik). Given that there are no changes of atmospheric forcing parameters within the next 80 years, one might expect to see 60 cm higher extreme events at all stations by 2100 (Figure 94-right).

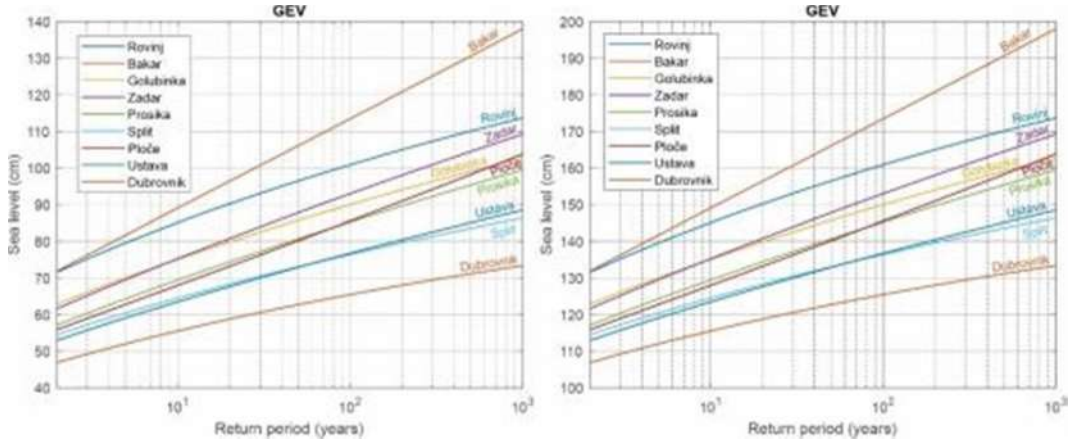

Figure 93 Return period of extreme sea level episodes (left) and return period values of extreme sea level episodes under an assumption of climate change characterized by a uniform sea level rise of 60 cm (right)

Observed and modelled sea level time series for the storm surge event of 29-30 October 2018 are shown in Figure 95. One can see that most extreme heights, both in term of value and timing, have been reproduced with a great skill at all stations. However, after the first storm surge maxima model appears to have a negative bias of ~10-20 cm – this is likely due to our choice of Otranto boundary conditions. Figure 95 also shows maximum modelled sea level along the Adriatic coast during the same 29-30 October event. A characteristic south-to-north sea level height gradient is reproduced clearly revealing the most endangered parts of the Adriatic coast.

Finally, spatial distributions of extreme sea level heights for 25-years and 100-years return periods are shown in Figure 96. It is clear that, in addition to the northern Adriatic, much wider stretches of the eastern and the western Adriatic coast are endangered by extreme sea levels.

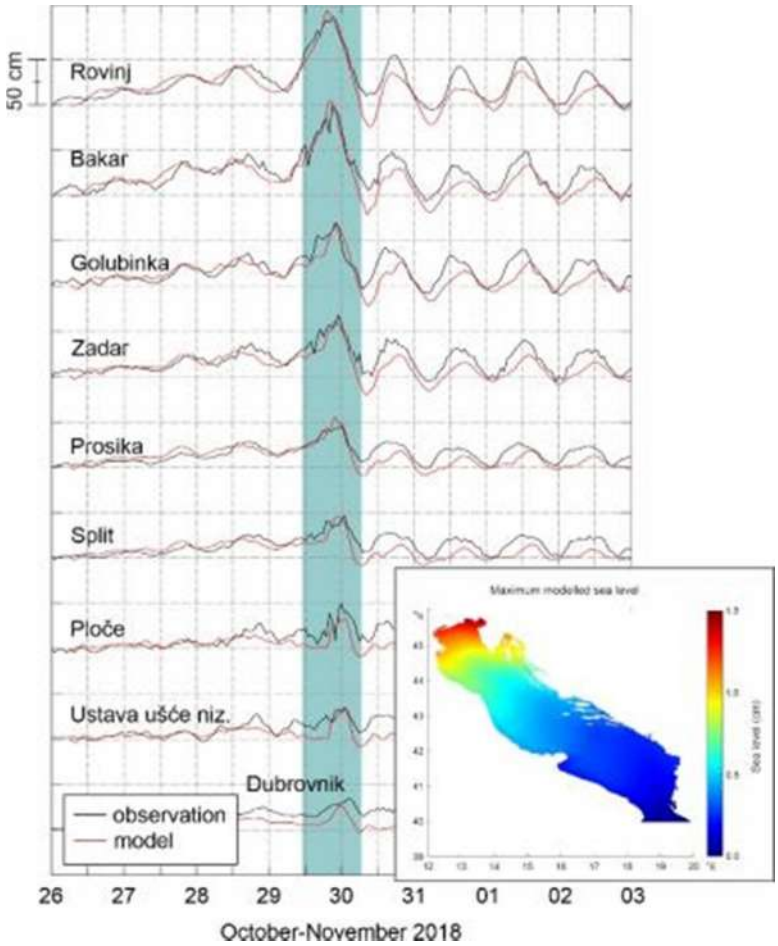

Figure 94 Observed (black) and modelled (red) hourly residual sea level time series during the storm surge event of 29-30 October 2018. Spatial distribution of maximum modelled sea levels is given in inset (Zhang et al., 2016b).

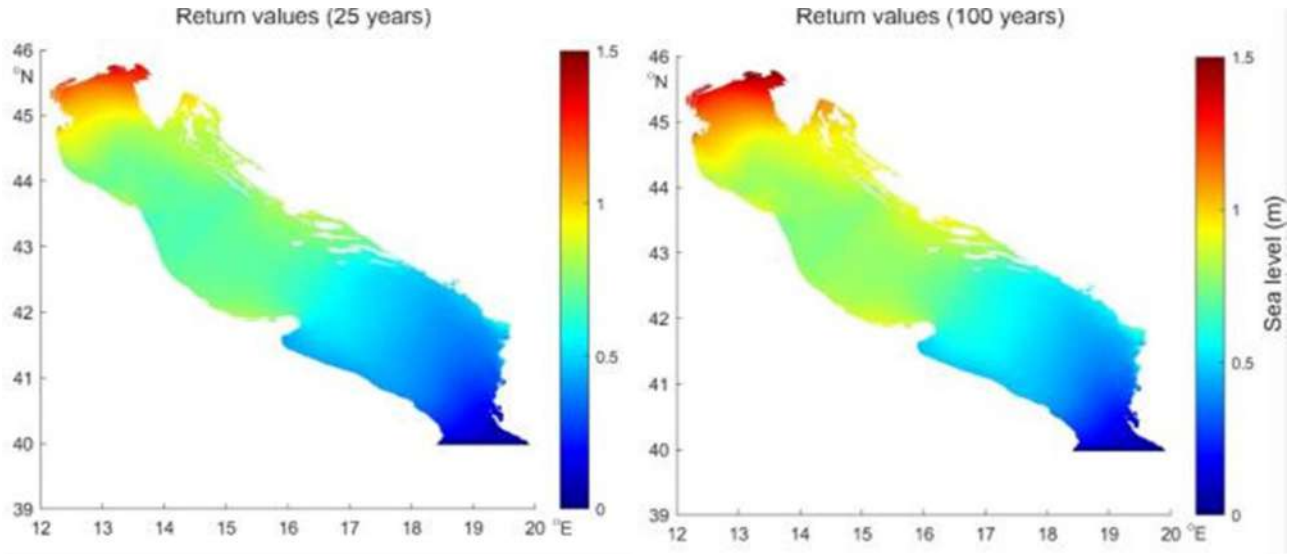

Figure 95 Extreme sea levels for: (left) 25-year return period; (right) 100-year return period

In conclusion, extreme sea levels for the return periods of 5 and 100 years were imposed on "SEA" open boundary (see Figure 69) with the values given in Table 24 (city of Zadar without the influence of climate change).

Table 24 Extreme sea levels for return periods of 5 and 100 years for the position of the city of Zadar (imposed at "SEA" open boundary)

Return period (year)	5	100
Extreme sea level – Zadar (cm)	70.1	93.0

At the "SEA" open boundary a constant sea temperature of 17 °C and salinity of 38.5 PSU were defined as a boundary condition for the whole period of simulation in the analysis of Miljašić Jaruga flow pattern for the planned state of construction. The initial conditions for sea temperature and salinity were taken from the results of previous simulations for the current state of construction on January 5th, 2023 (Figure 97). Wind was not considered during these simulations.

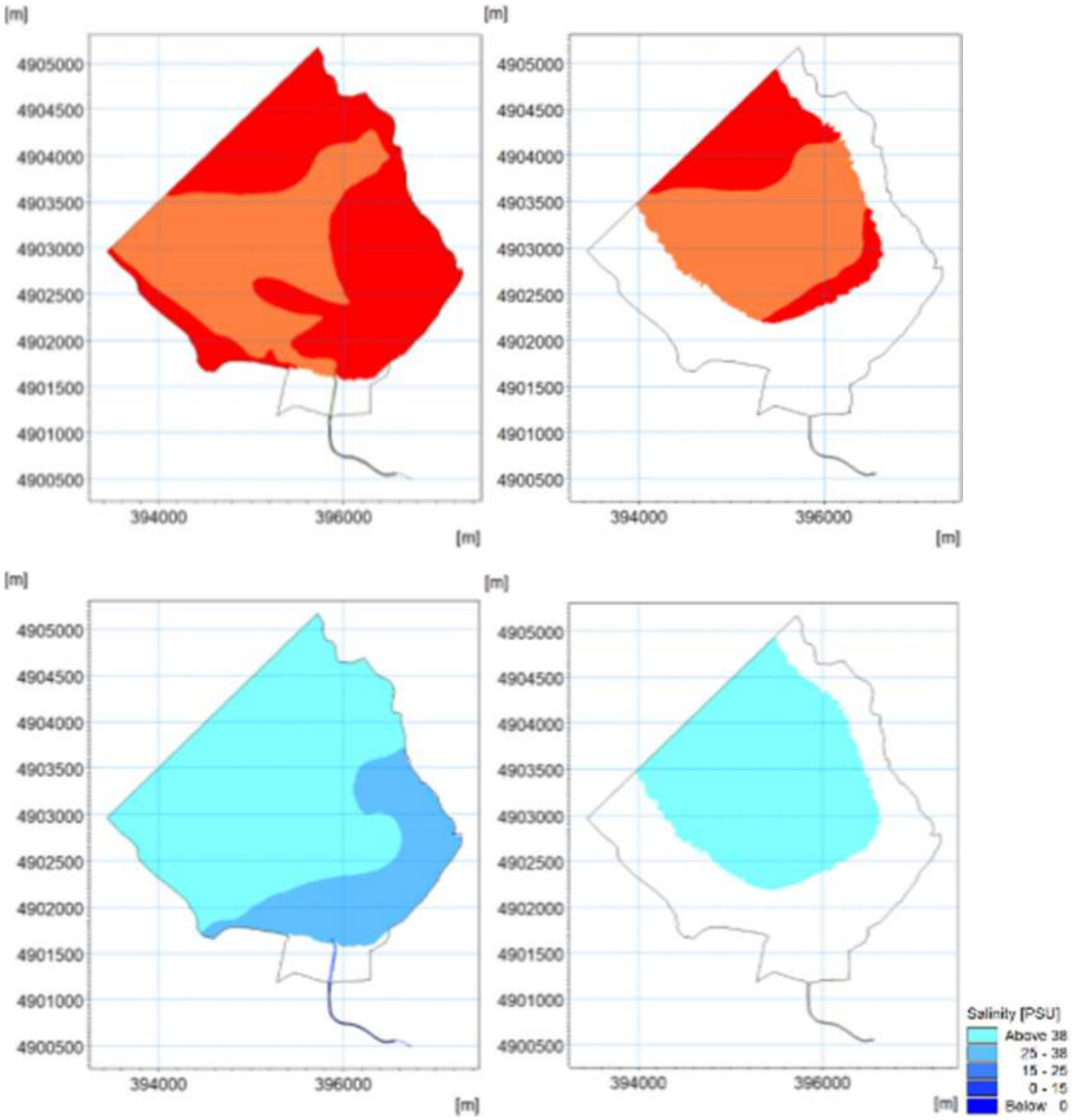

Figure 96 The spatial distribution of sea temperature and salinity at depths of -1 and -8 m used as initial conditions for simulations in the planned state of construction (taken from the results of previous simulations in the current state of construction at the term January 5th, 2023)

At the "MJ" open boundary a constant water temperature of 10 °C and salinity of 0 PSU were defined as a boundary condition. Discharge boundary condition was imposed according to the graph below (Figure 98) according to the following procedure.

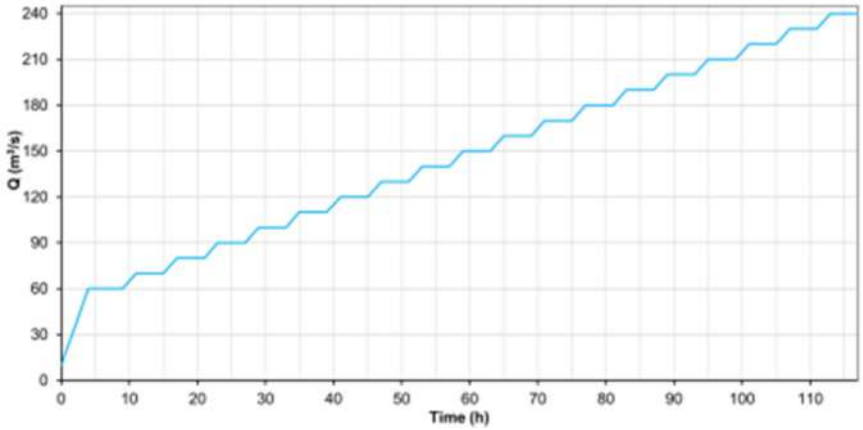

Figure 97 Discharge time series imposed at the "MJ" open boundary of the model simulations of the planned state of construction

The results of the model simulation for the planned state of construction will be presented in section 3.5.1.5 for each of the extreme sea level imposed on boundary condition presented in Table 24 and for the extreme discharge values presented in DUEL PROJEKT (2019). The extreme discharges are split into two sets of values that flood frequency analysis was performed on (Table 25). The first one was conducted based on the historical flood events which considered the transformation of the flood waves from the upstream river sections to the study section of the Miljašić Jaruga river (in further text referred as set 1). The second set is based on the analysis of hypothetic hydrographs obtained from the SCS method which do not consider the transformation process of the flood wave from the upstream river sections to the study area (in further text referred as set 2) covered within this analysis.

Table 25 Extreme discharges of Miljašić Jaruga river based on the flood frequency analysis [0] used for the presentation of the hydrodynamic model results for the planned state of construction

	Return period (year)			
	10	25	50	100
	Extreme discharge of Miljašić Jaruga river in (m^3/s)			
based on historical flood events	57	81	101	120
based on SCS method	81	103	159	236

As it can be seen from the Table 25 a 25-year extreme discharge from the set 1 corresponds to the 10-year value from the set 2. The same pattern is evident when 50-year discharge from set 1 is compared to 25-year extreme discharge from set 2. Therefore, the results for the pairs of similar

extreme discharge values will be presented in the same graphs per each pair what will be further discussed in chapter 3.5.1.5.

The parameterization of k-ε turbulence model and roughness is the same as previously adopted in the simulation for the existing state of construction.

3.5.1.5 Numerical model simulation results

Figure 99-Figure 108 show the hourly average current fields at depths of -1 m and -8 m for several dates within the simulation period December 16th, 2022, to February 2nd, 2023, which cover different meteorological conditions related to wind as well as the peak discharge value that occurred in Miljašić Jaruga during this period.

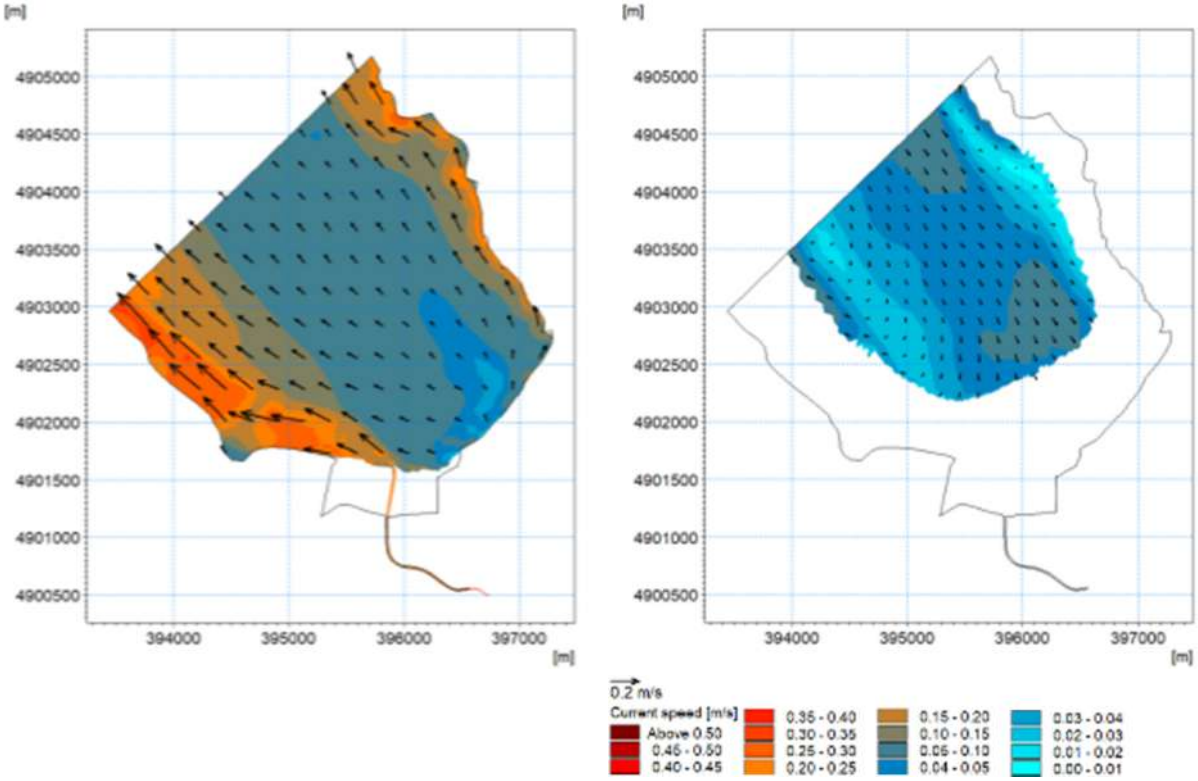

Figure 98 Hourly averaged current field at the depth of -1 m (left) and -8 m (right) for January 9th, 2023, at 10:00 (current state of construction) for SE wind with speed of 9.7 m/s and Miljašić Jaruga discharge of 1.1 m^3/s

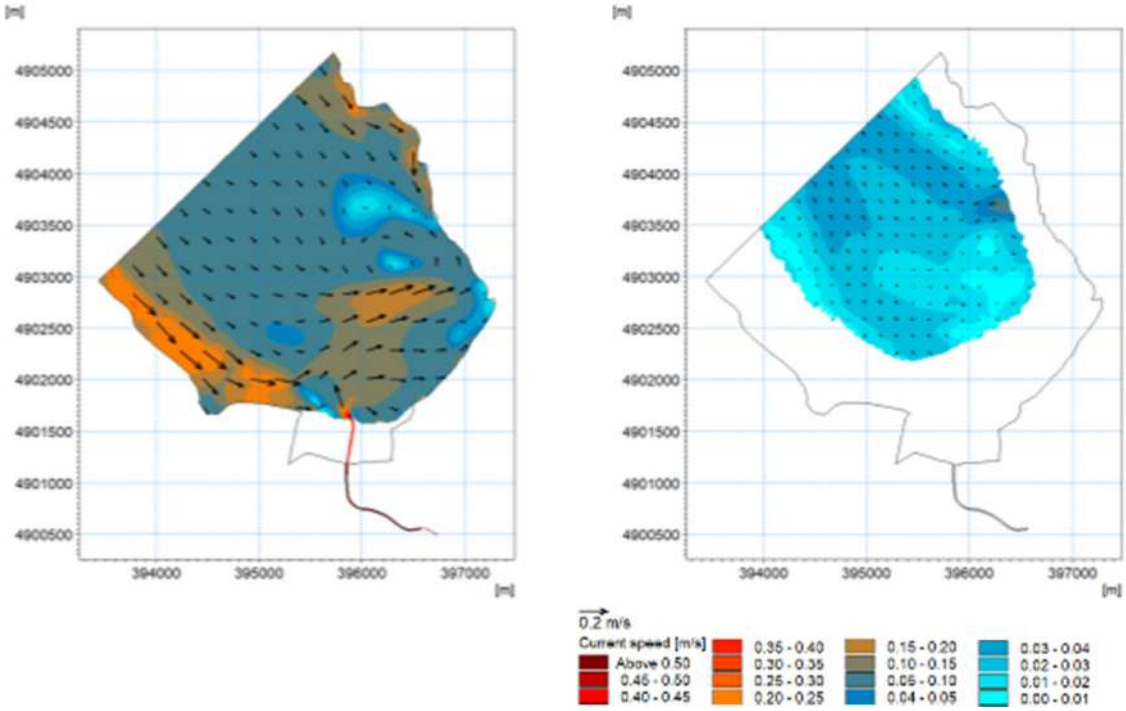

Figure 99 Hourly averaged current field at the depth of -1 m (left) and -8 m (right) for on January 10th, 2023, at 13:00 (current state of construction) for NW wind with speed of 7.8 m/s and Miljašić Jaruga discharge of 4.6 m^3/s

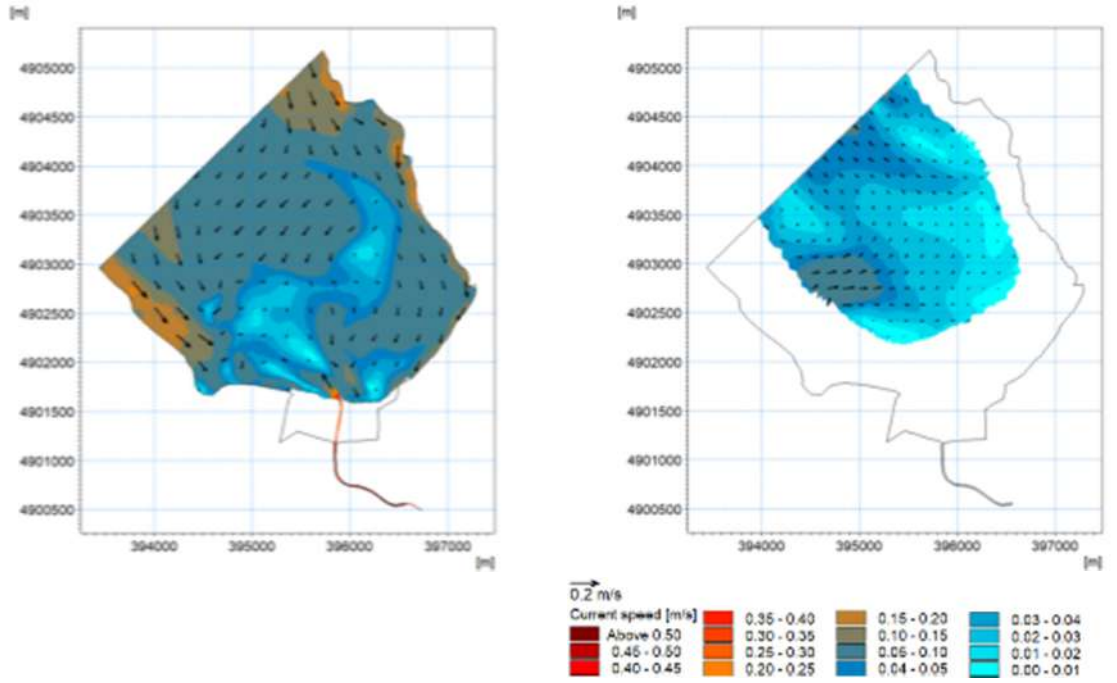

Figure 100 Hourly averaged current field at the depth of -1 m (left) and -8 m (right) for on January 10th, 2023, at 19:00 (current state of construction) for N wind with speed of 7.8 m/s and Miljašić Jaruga discharge of 3.3 m^3/s

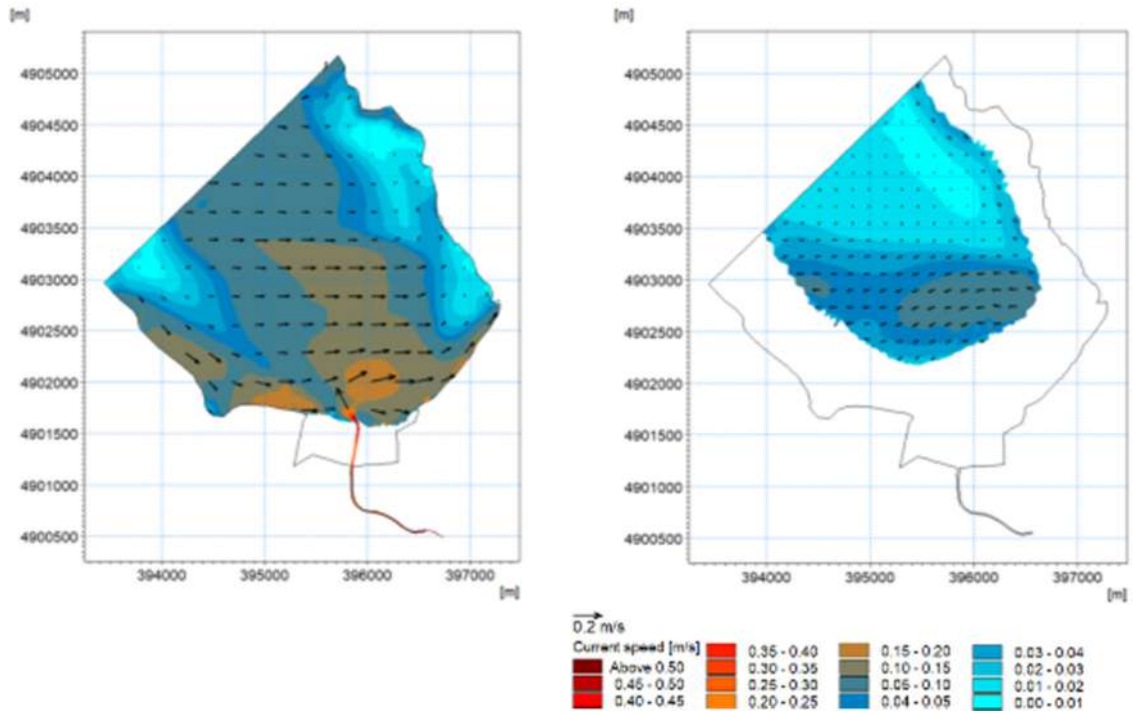

Figure 101 Hourly averaged current field at the depth of -1 m (left) and -8 m (right) for on January 10th, 2023, at 01:00 (current state of construction) for W wind with speed of 10.3 m/s and Miljašić Jaruga discharge of 2.4 m^3/s

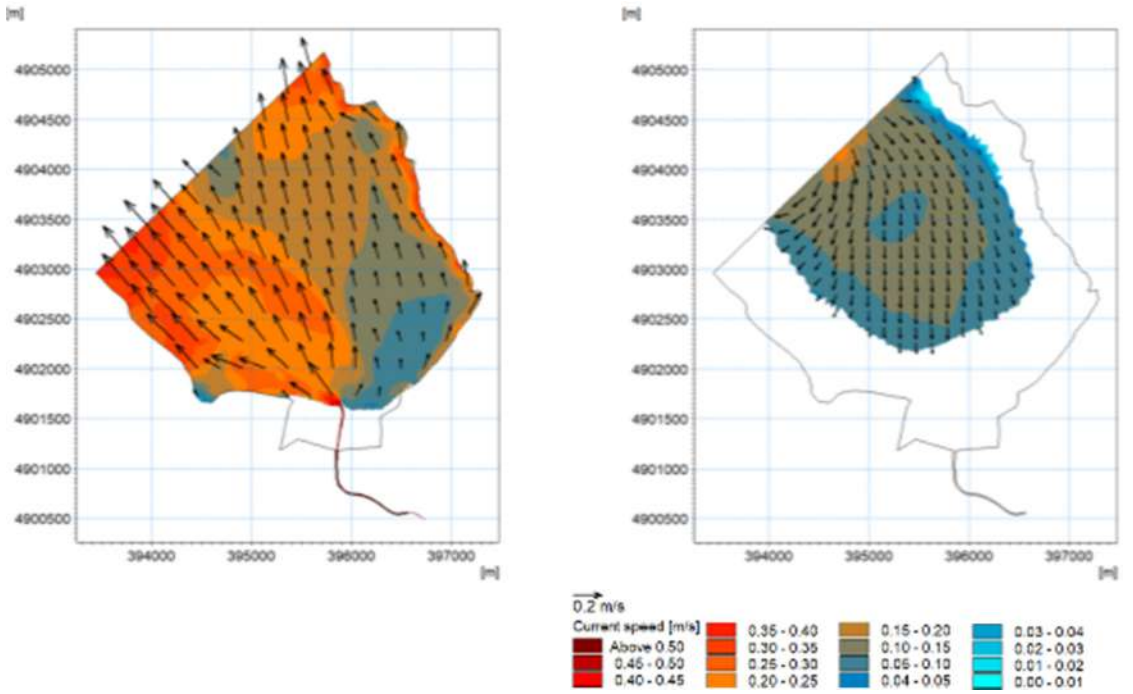

Figure 102 Hourly averaged current field at the depth of -1 m (left) and -8 m (right) for on January 17th, 2023, at 14:00 (current state of construction) for S wind with speed of 11.4 m/s and Miljašić Jaruga discharge of 4.0 m^3/s

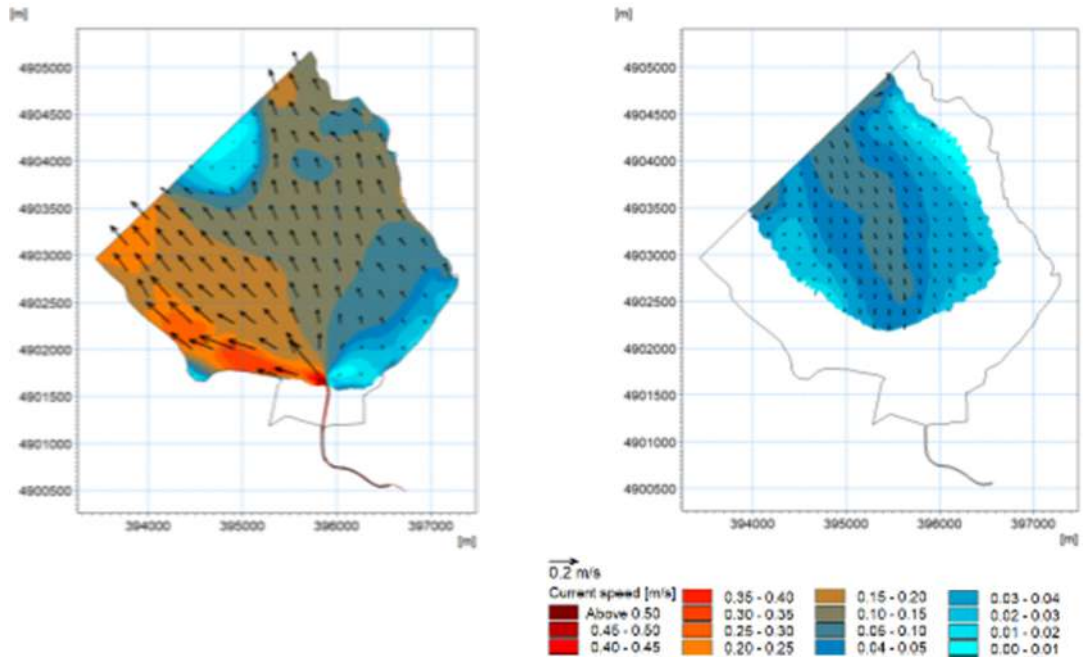

Figure 103 Hourly averaged current field at the depth of -1 m (left) and -8 m (right) for on January 17th, 2023, at 23:00 (current state of construction) for SE wind with speed of 4.7 m/s and peak Miljašić Jaruga discharge of 14.9 m^3/s that occurred during the simulation period

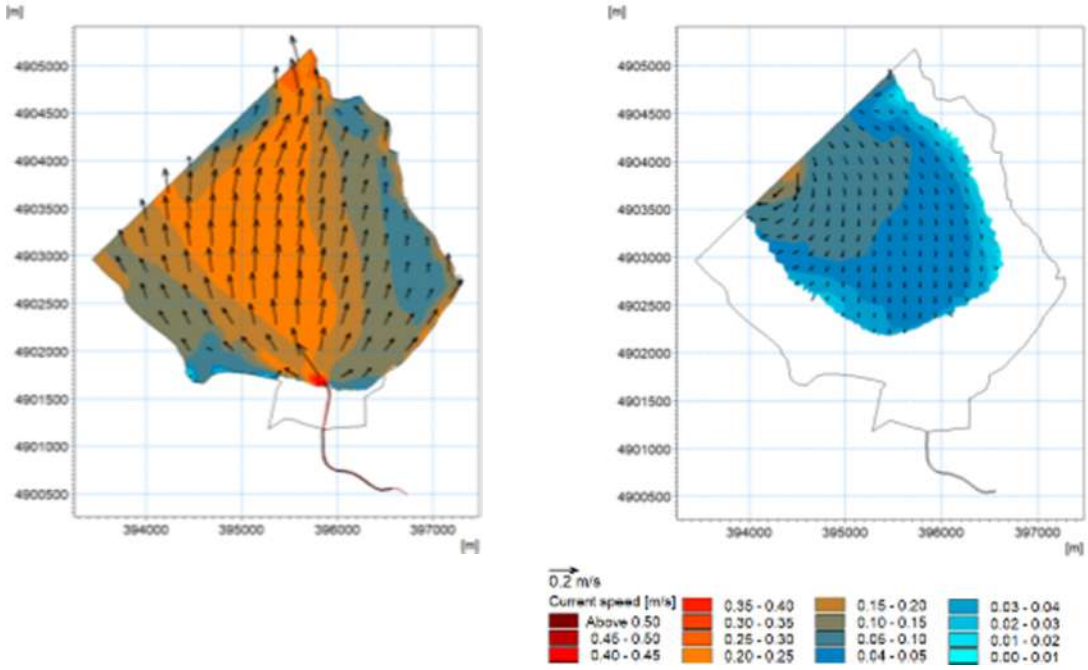

Figure 104 Hourly averaged current field at the depth of -1 m (left) and -8 m (right) for on January 17th, 2023, at 23:00 (current state of construction) for SW wind with speed of 8.3 m/s and Miljašić Jaruga discharge of 8.1 m^3/s

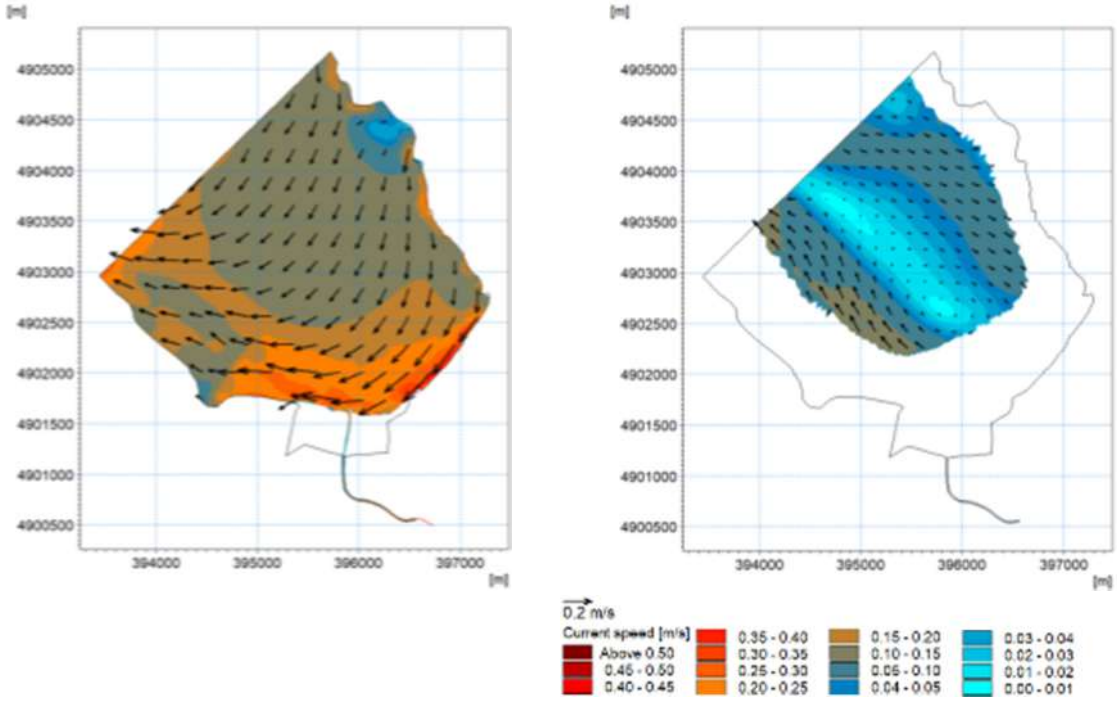

Figure 105 Hourly averaged current field at the depth of -1 m (left) and -8 m (right) for on January 21st, 2023, at 18:00 (current state of construction) for NE wind with speed of 12.2 m/s and Miljašić Jaruga discharge of 2.9 m^3/s

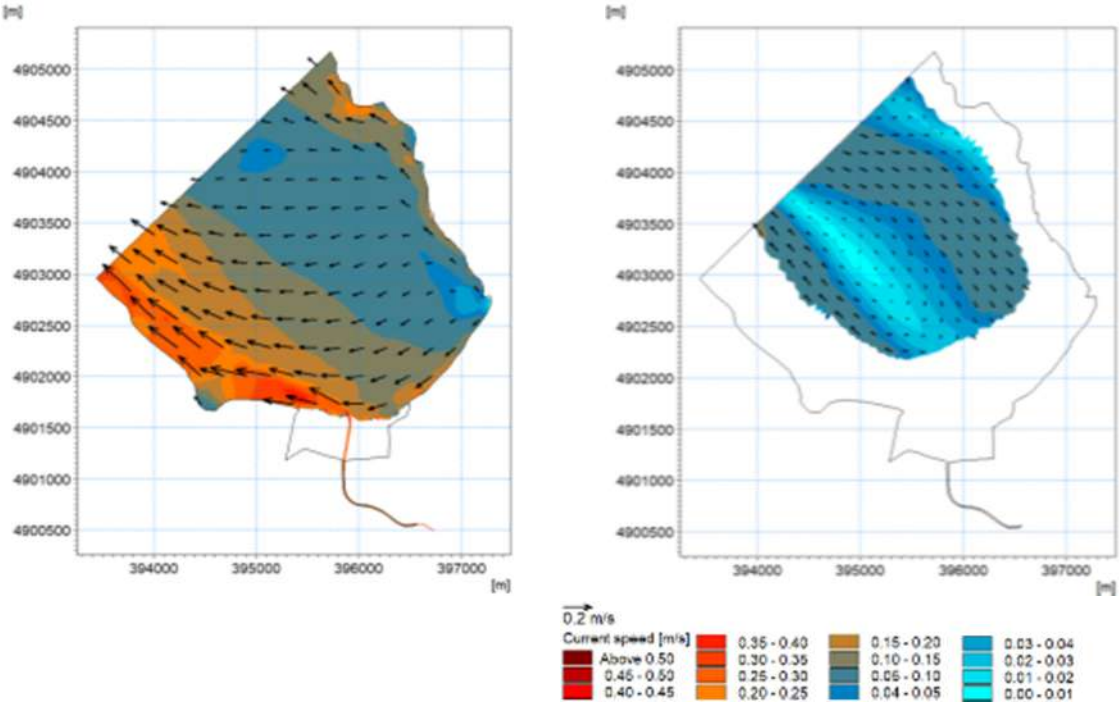

Figure 106 Hourly averaged current field at the depth of -1 m (left) and -8 m (right) for on January 23rd, 2023, at 12:00 (current state of construction) for E wind with speed of 10.3 m/s and Miljašić Jaruga discharge of 6.1 m^3/s

In the graphs below the results of the model simulation for the planned state of construction of the flood event Sep2017 is presented through the flood extent during the peak discharge value of 113 m^3/s (see Figure 92). The boundary conditions at the "SEA" and "MJ" open boundaries as well as the homogenous and non-stationary wind field have been defined in the same way as for the model simulations of the current state of construction.

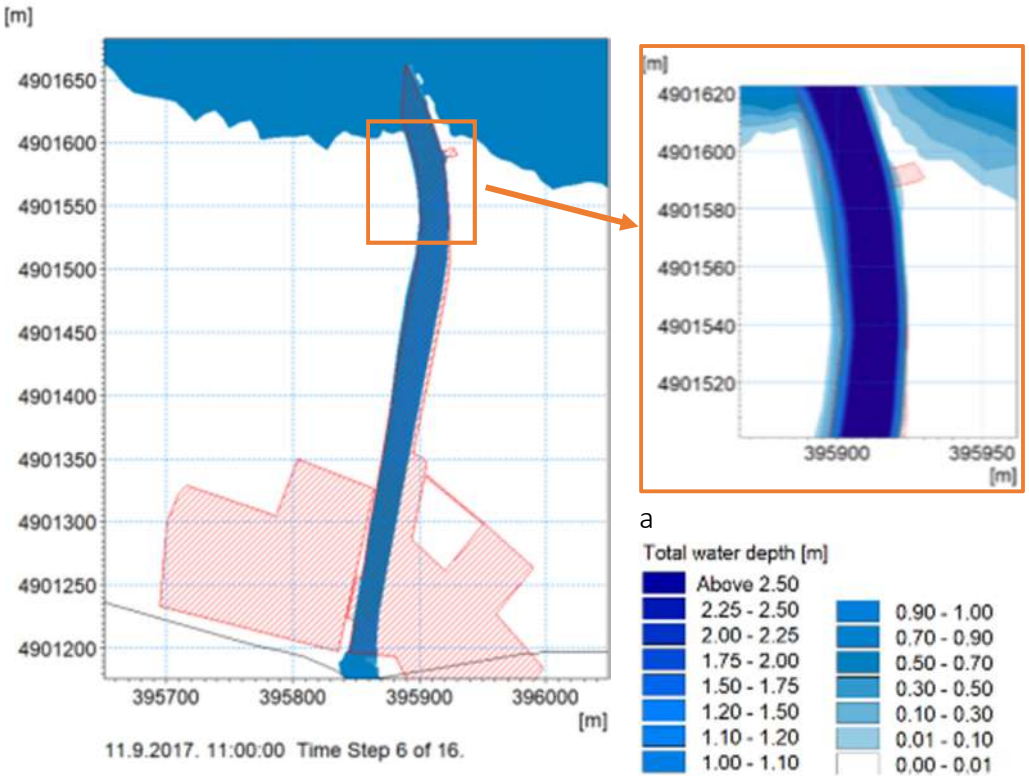

Figure 107 A comparison of flood extent (left) estimated from the video recordings (red hatch) and extent obtained by hydrodynamic model for planned state of construction (blue fill) with detail of total water depth field during the overbank flow upstream of the river mouth (right) for a peak discharge of Q = 113 $m^3/$ during flood event Sep2017

The direct benefit of the planned state of construction along the analysed Milašić Jaruga river section is evident through the lack of overbank flow and lack of flooding of the area out of the riverbanks what occurred during the Sep2017 flood event for the current state of construction.

The following graphs show the steady state flow fields in Miljašić Jaruga river for the simulations during the 5- and 100-year extreme sea level values (see Table 24) and two sets of extreme discharges of Miljašić Jaruga river (see Table 25).

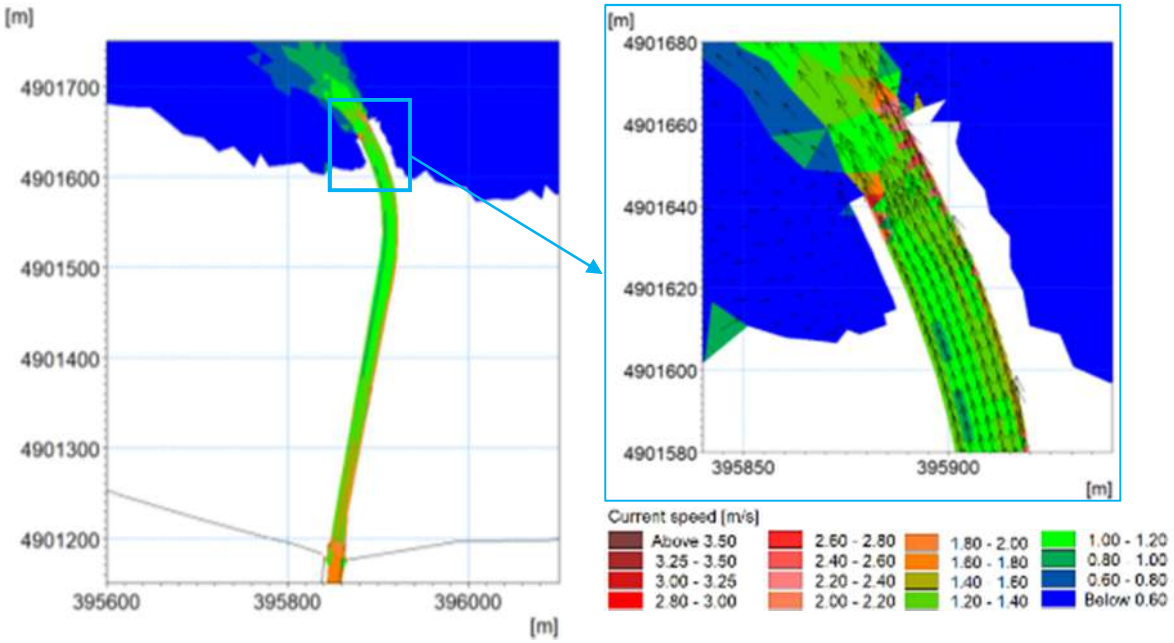

Figure 108 Flow velocity field and water extent in study section of the Miljašić Jaruga river for 5-year extreme sea level value of 70.1 cm and Miljašić Jaruga discharge of 57 m3/s what corresponds to 10-year extreme discharge from set 1 (planned state of construction)

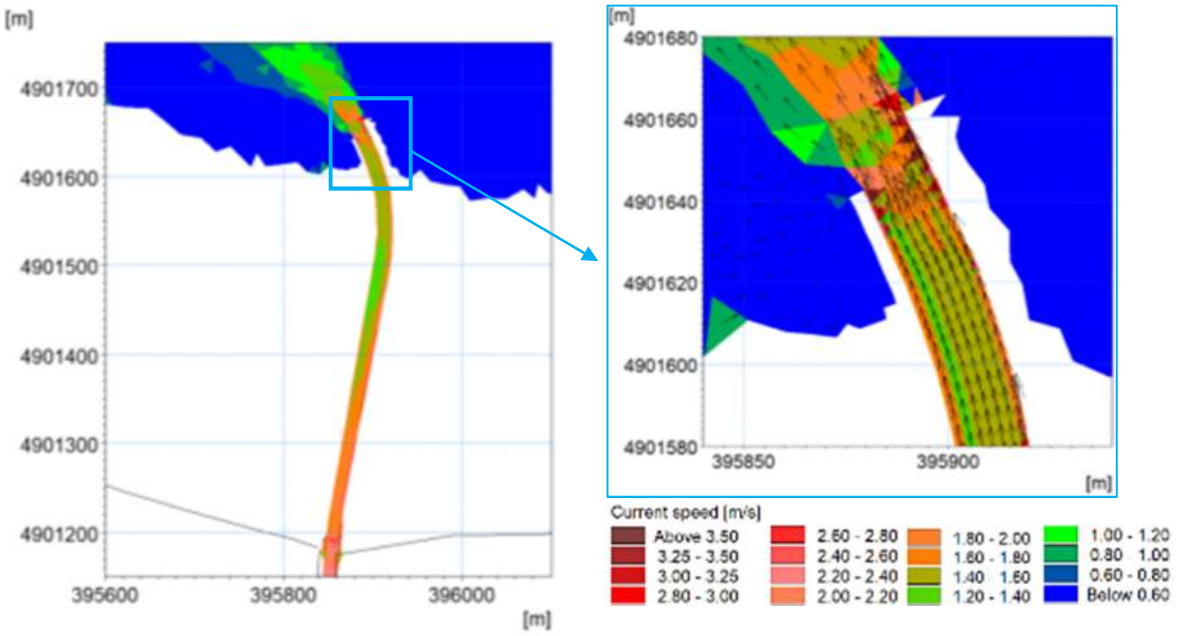

Figure 109 Flow velocity field and water extent in study section of the Miljašić Jaruga river for 5-year extreme sea level value of 70.1 cm and Miljašić Jaruga discharge of 81 m^3/s what corresponds to 25-year for set 1 or 10-year extreme discharge from the set 2 (see Table 25, planned state of construction)

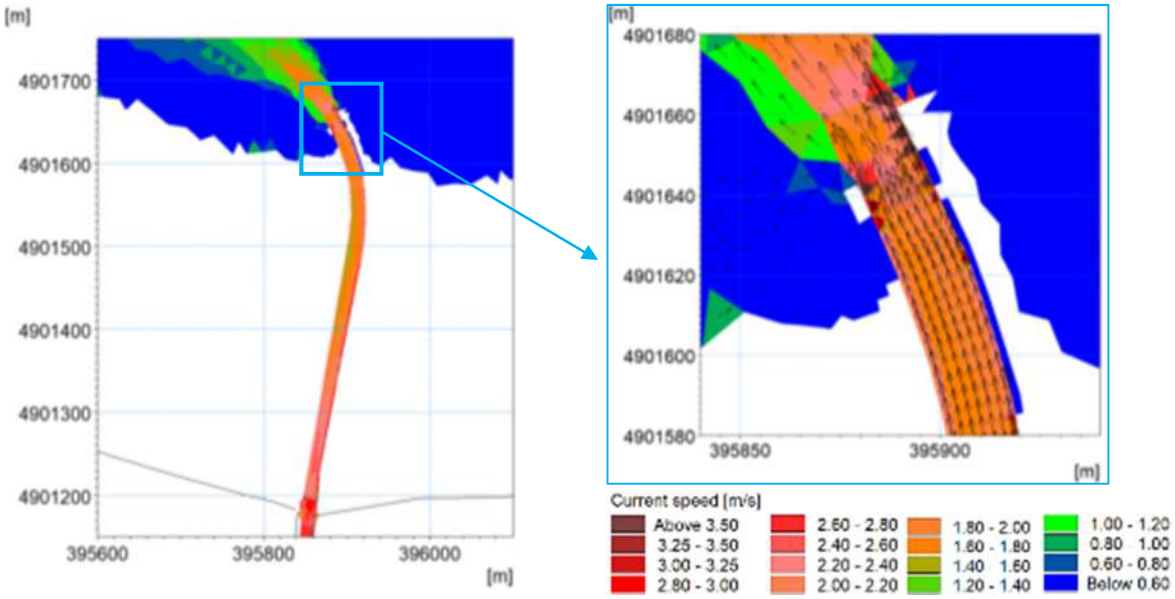

Figure 110 Flow velocity field and water extent in study section of the Miljašić Jaruga river for 5-year extreme sea level value of 70.1 cm and Miljašić Jaruga discharge of 101 m^3/s what corresponds to 50-year for set 1 or nearly 25-year extreme discharge from the set 2 (see Table 25, planned state of construction)

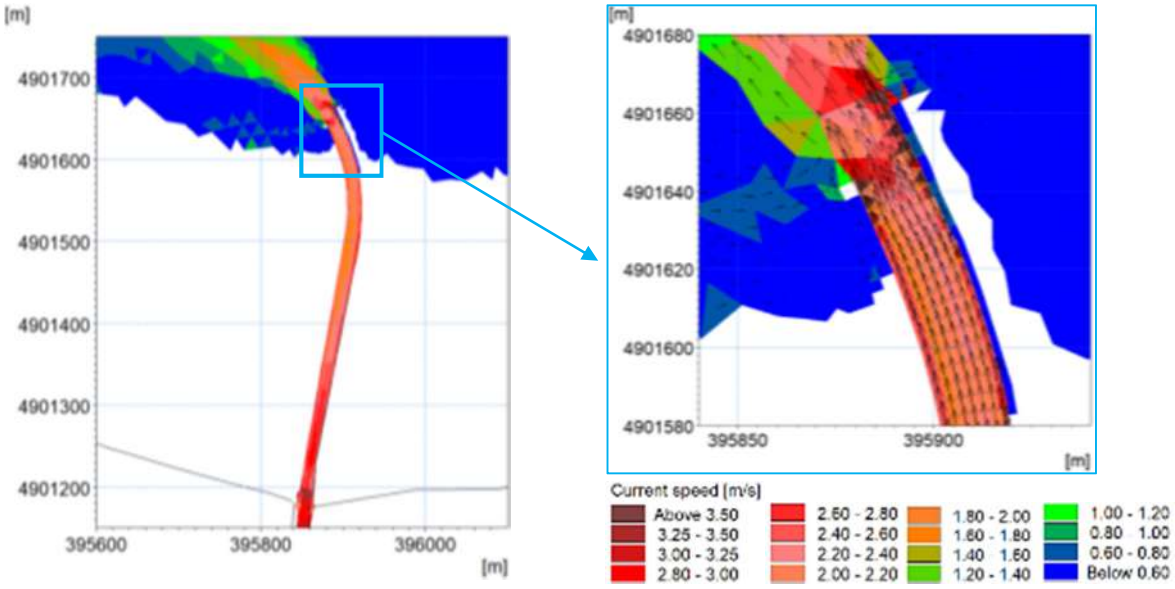

Figure 111 Flow velocity field and water extent in study section of the Miljašić Jaruga river for 5-year extreme sea level value of 70.1 cm and Miljašić Jaruga discharge of 120 m^3/s what corresponds to 100-year extreme discharge from set 1 (see Table 25, planned state of construction)

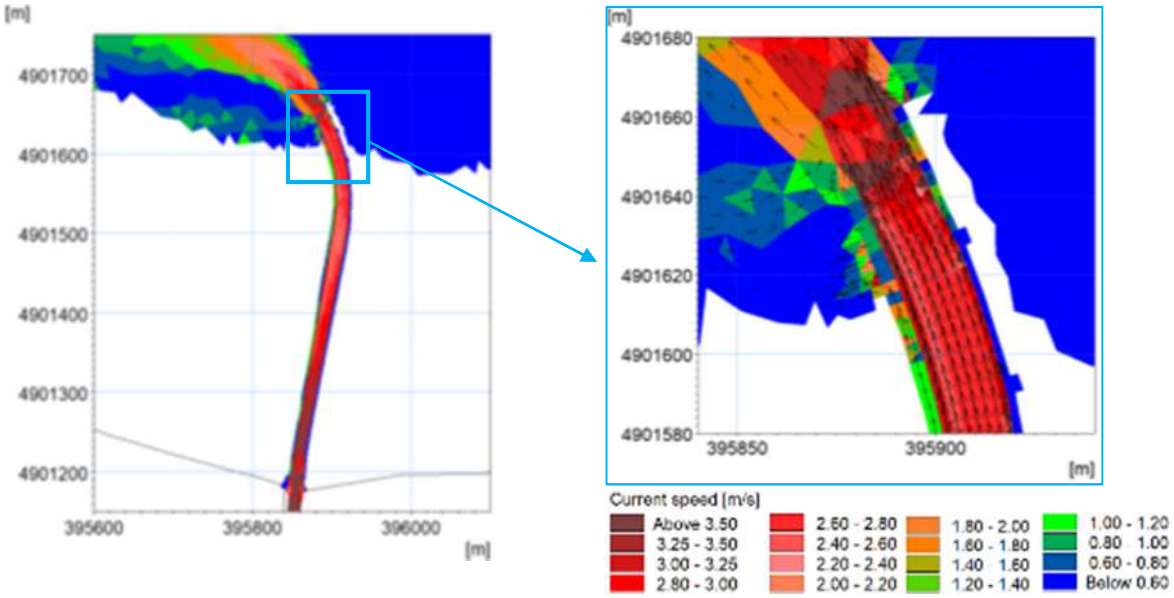

Figure 112 Flow velocity field and water extent in study section of the Miljašić Jaruga river for 5-year extreme sea level value of 70.1 cm and Miljašić Jaruga discharge of 159 m^3/s what corresponds to 50-year extreme discharge from set 2 (planned state of construction)

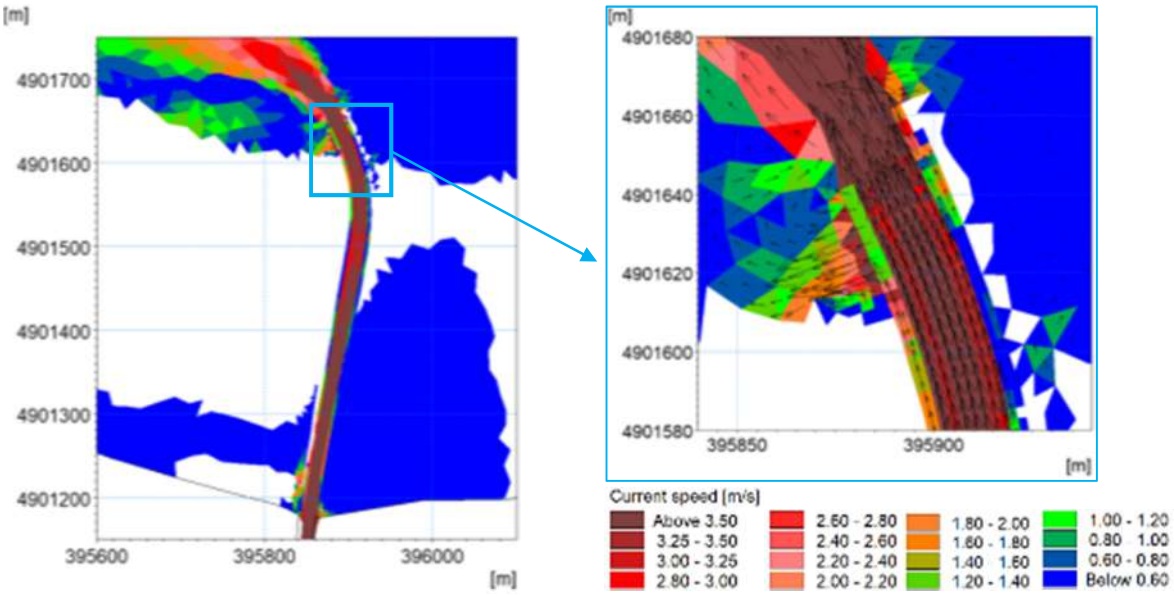

Figure 113 Flow velocity field and water extent in study section of the Miljašić Jaruga river for 5-year extreme sea level value of 70.1 cm and Miljašić Jaruga discharge of 236 m^3/s what corresponds to 100-year extreme discharge from set 2 (planned state of construction)

Based on the simulation results for the 5-year extreme sea level value of 70.1 cm (Table 24) which is imposed at the "SEA" open boundary in combination with extreme discharges from DUEL

PROJEKT (2019) imposed at the "MJ" open boundary, the following can be concluded. Also, it is important to note that the two sets of the extreme discharges are presented in Table 25. For sea water level of 70.1 cm (5-year return period), the river exceeds its bankfull conditions at the discharge of 195 m^3/s what is approximately twice as high as the bankfull discharge in the current state of construction. In terms of flood frequency analysis conducted by DUEL PROJEKT (2019), the bankfull discharge return period is between 50 and 100 years in set 2 of extreme discharge values (calculated by using synthetic SCS hydrographs which do not consider flood wave transformation). The overbank flow occurs around 10 metres upstream and downstream of the road bridge profile, but it does not happen along the Miljašić Jaruga river section that is the focus of this project. The water spills over the left groyne of the planned state of construction defined based on the Carević et al. (2021) after reaching 95 m^3/s what corresponds to nearly 50-year discharge if set 1 is considered (flood frequency analysis based on historical flood events) and nearly 25-year discharge for set 2 of extreme discharge values (see Table 25). Interestingly, right groyne does not get flooded neither during the highest discharge (Figure 79) for 5-year extreme sea level.

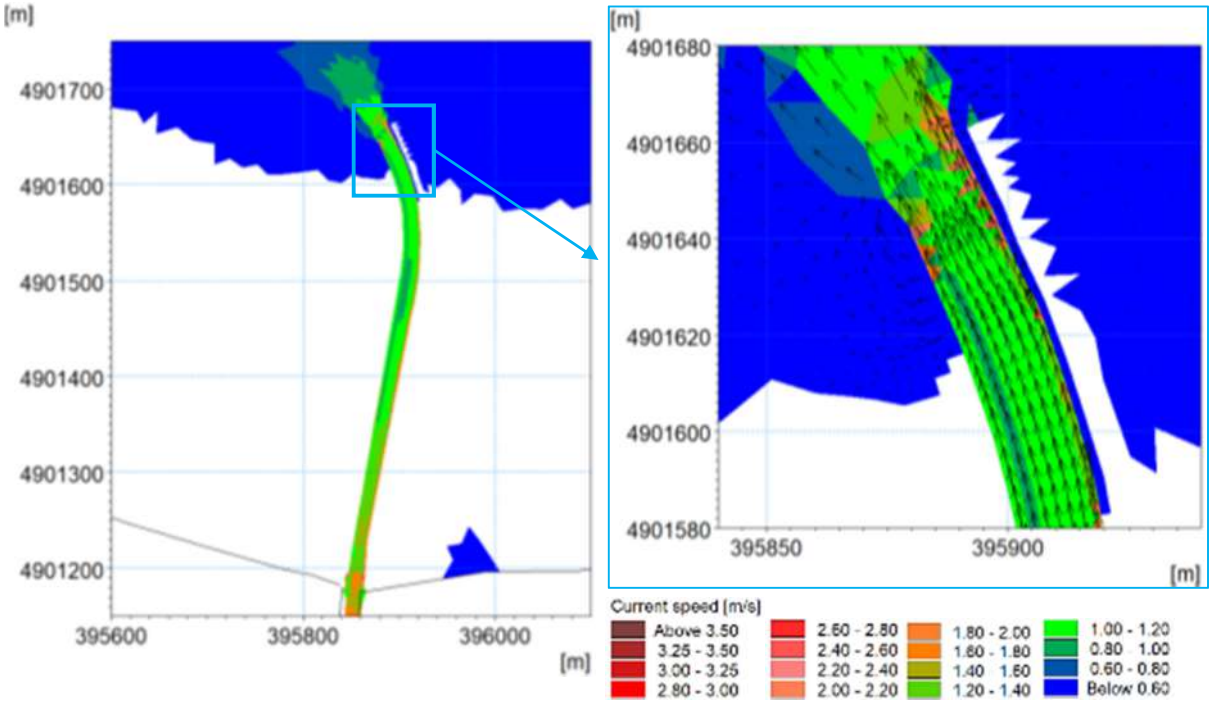

Figure 114 Flow velocity field and water extent in study section of the Miljašić Jaruga river for 100-year extreme sea level value of 93 cm and Miljašić Jaruga discharge of 57 m^3/s what corresponds to 10-year extreme discharge from set 1 (planned state of construction)

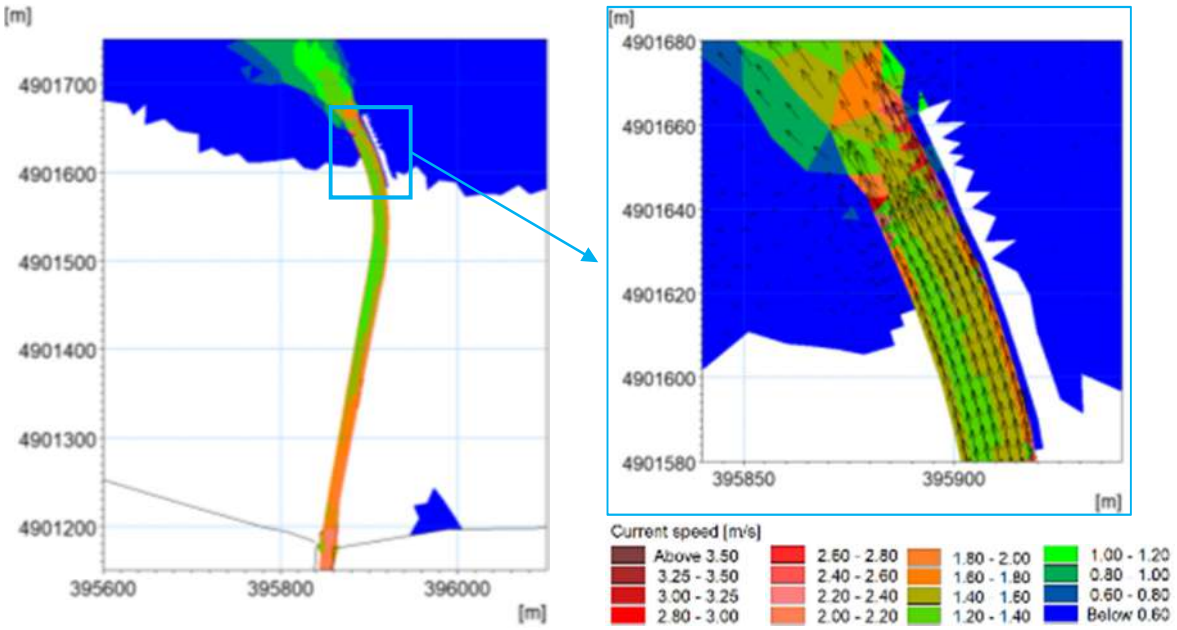

Figure 115 Flow velocity field and water extent in study section of the Miljašić Jaruga river for 100-year extreme sea level value of 93 cm and Miljašić Jaruga discharge of 81 m^3/s what corresponds to 25-year for set 1 or 10-year extreme discharge from the set 2 (see Table 25, planned state of construction)

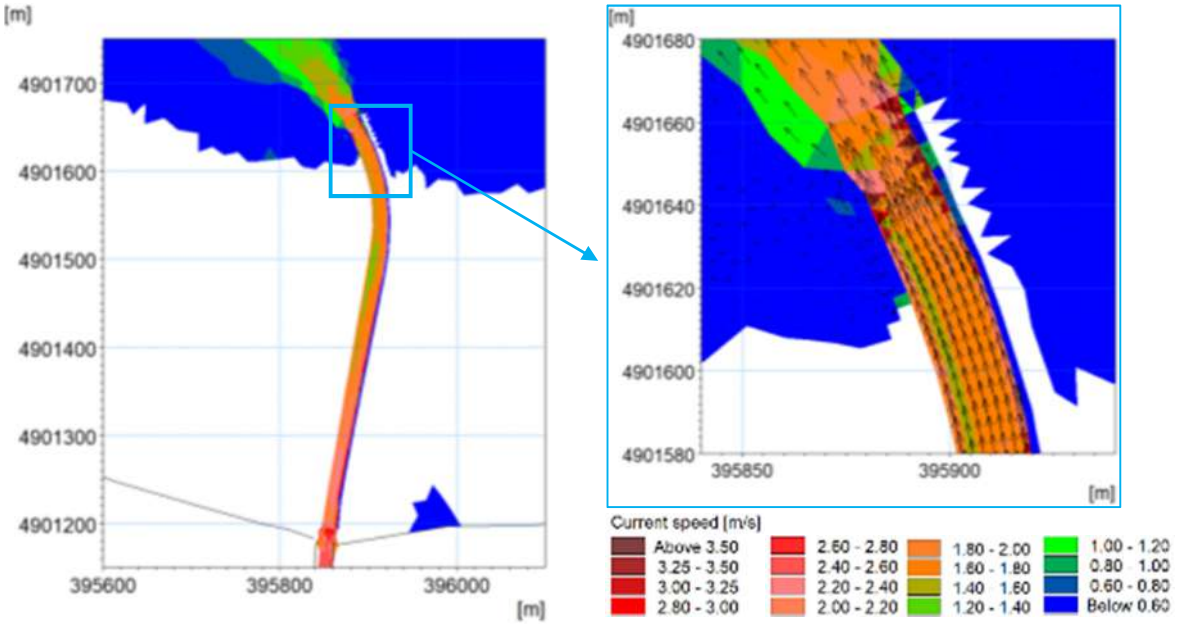

Figure 116 Flow velocity field and water extent in study section of the Miljašić Jaruga river for 100-year extreme sea level value of 93 cm and Miljašić Jaruga discharge of 101 m^3/s what corresponds to 50-year for set 1 or nearly 25-year extreme discharge from the set 2 (see Table 25, planned state of construction)

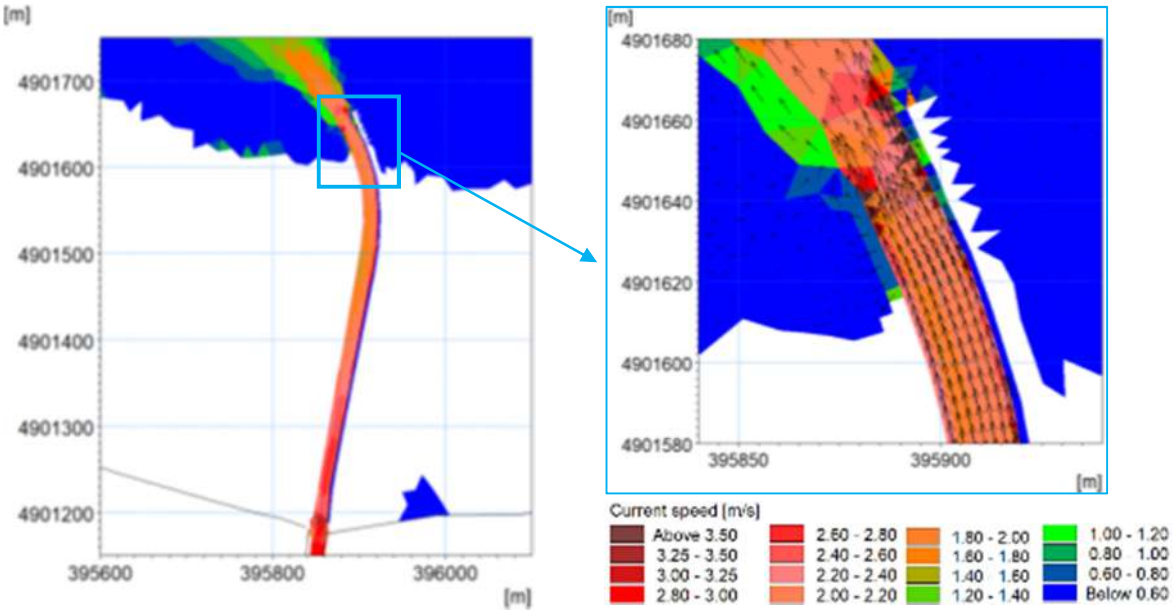

Figure 117 Flow velocity field and water extent in study section of the Miljašić Jaruga river for 100-year extreme sea level value of 93 cm and Miljašić Jaruga discharge of 120 m^3/s what corresponds to 100-year extreme discharge from set 1 (planned state of construction)

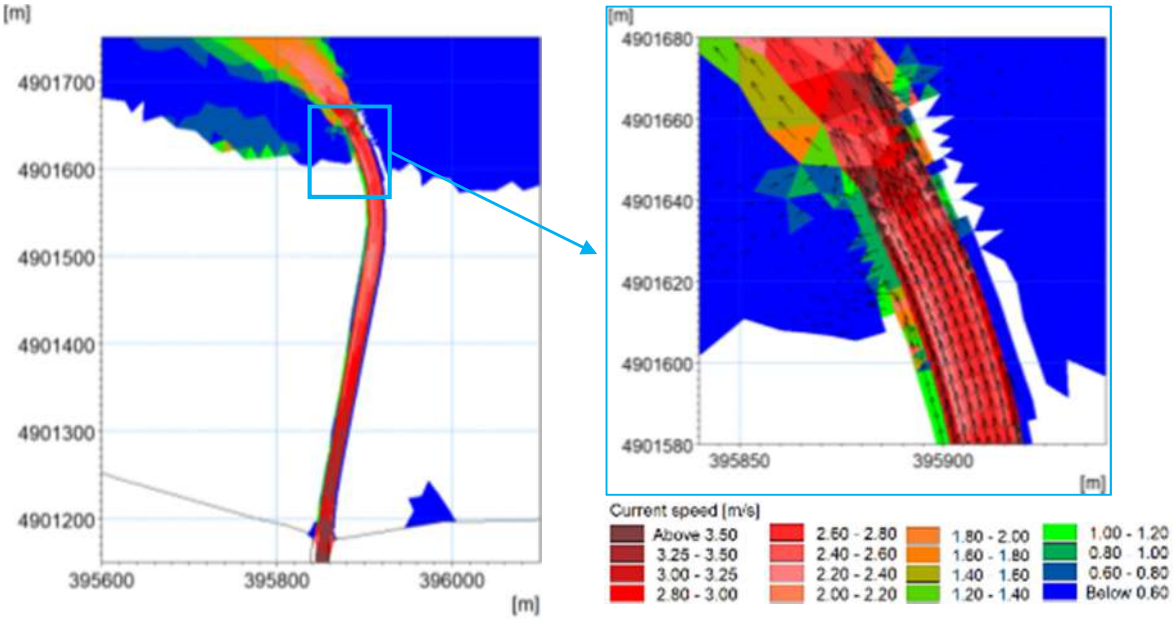

Figure 118 Flow velocity field and water extent in study section of the Miljašić Jaruga river for 100-year extreme sea level value of 93 cm and Miljašić Jaruga discharge of 159 m^3/s what corresponds to 50-year extreme discharge from set 2 (planned state of construction)

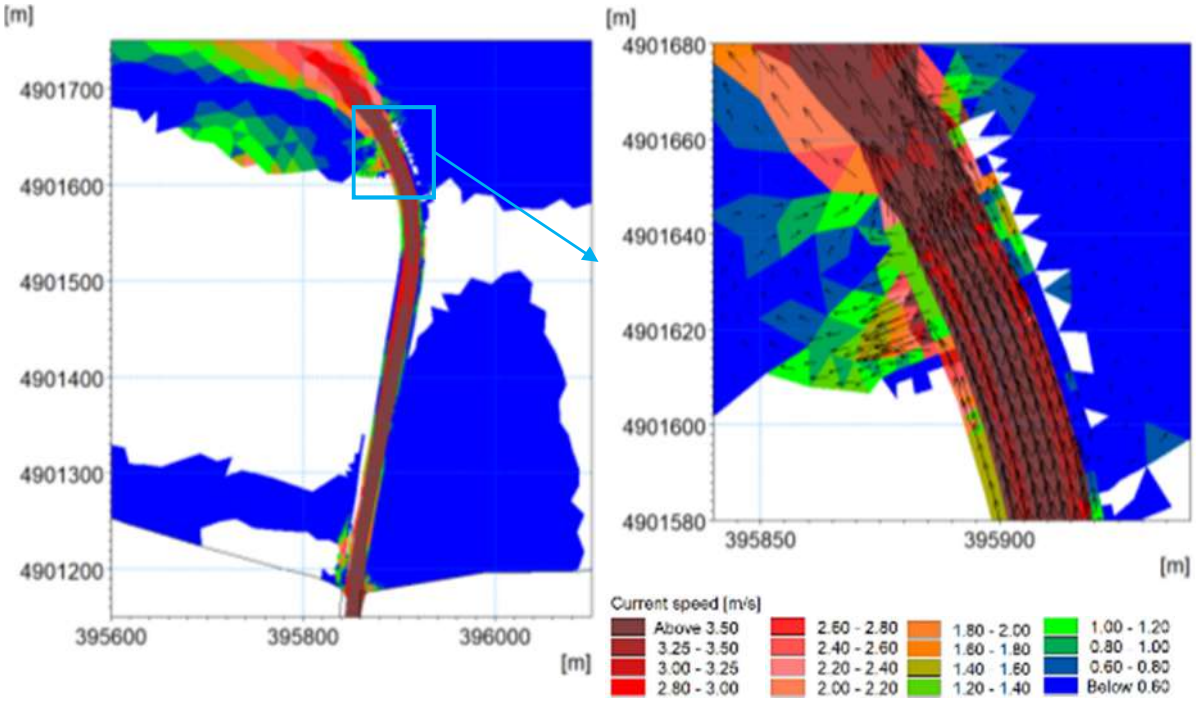

Figure 119 Flow velocity field and water extent in study section of the Miljašić Jaruga river for 100-year extreme sea level value of 93 cm and Miljašić Jaruga discharge of 236 m^3/s what corresponds to 100-year extreme discharge from set 2 (planned state of construction)

The simulation results for the 100-year extreme sea level value of 90 cm (Table 24) which is imposed at the "SEA" open boundary in combination with extreme discharges from DUEL PROJEKT (2019) imposed at the "MJ" open boundary, show that the overbank flow occurs for lower discharge rates as expected. The river exceeds its bankfull conditions at the discharge of 190 m^3/s what is approximately two times higher than the bankfull discharge in the current state of construction (similar as for 5-year extreme water level). In terms of flood frequency analysis conducted by DUEL PROJEKT (2019), the bankfull discharge return period is between 50 and 100 years in set 2 of extreme discharge values. The overbank flow occurs around 10 metres upstream and downstream of the road bridge profile, but it does not happen along the Miljašić Jaruga river section that is the focus of this project. The water spills over the left groyne of the planned state of construction defined based on Carević et al. (2021) after reaching 60 m^3/s (Figure 115) what corresponds to a value a bit higher than 10-year discharge if set 1 is considered (see Table 25). For this extreme sea level, the right groyne overflow occurs at the highest discharge of 240 m^3/s (Figure 120). Not get flooded neither during the highest discharge (Figure 79) for 5-year extreme sea level.

3.5.2 Wave numerical model of the Nin Bay (HR)

The goal of this study is to provide relevant design wave parameters for the Nin Bay, Croatia. These design parameters are valuable to calculate the hydrodynamic forces on coastal structures. The relevant parameters include values for a 5 year, 20 year, 50 year and 100 year return period (also known as a recurrence interval, is an average time or an estimated average time between extreme events such as waves, earthquakes, floods, landslides and droughts). Three meaningful locations have been chosen which are most relevant for the Miljašić Jaruga river mouth, as well as the whole Nin Bay (Figure 121) and wave parameters (significant wave height, peak wave period and wave direction) on the three locations for 5 year, 20 year, 50 year and 100 year return period will be provided. Long-term wave forecasting will be conducted using wind data extracted from the well-known ERA5 climate reanalysis model.

3.5.2.1 Modelling approach

The third generation of the SWAN spectral wave model (version 41.41 is used in this paper), developed in Fortran90 at Delft University of Technology, is known for its exceptional performance in simulating wave propagation and wave growth due to wind power. SWAN is based on the dynamic spectral balance equation and is represented in Cartesian coordinates as follows:

$$\frac{\partial N}{\partial t}+\frac{\partial C_x N}{\partial x}+\frac{\partial C_y N}{\partial y}+\frac{\partial C_\sigma N}{\partial \sigma}+\frac{\partial C_\theta N}{\partial \theta}=\frac{S}{\sigma}, \tag{5}$$

$$N=\frac{E}{\sigma}, \tag{6}$$

where the left-hand side represents the kinematic component and shows the derivatives of the active density N in the geographic and spectral space. C_x and C_y are the Cartesian coordinate components of the wave group velocity in geographic space, while C_ϑ and C_σ are the spectral components of the wave group velocity. The effective density N is the ratio of the wave energy spectrum $E(\sigma, \vartheta)$ and frequency σ. The term S on the right-hand side represents the total source of wave energy. The total source term is composed of the following terms:

$$S=S_{in}+S_{ds}+S_{bot}+S_{br}+S_{nl3}+S_{nl4}, \tag{7}$$

where S_{in} is the energy input due to wind, S_{ds} is the dissipation due to white-capping, S_{nl4} is the nonlinear wave energy transfer between quadruplets, S_{nl3} is the triad nonlinear interaction, S_{fric} is dissipation due to bottom friction, and S_{brk} is dissipation due to depth-induced wave breaking.

SWAN allows the user to turn source terms on and off, as well as choose different formulations for each source term in governing equations. The full description of the numerical wave model can be found in the scientific and technical documents of SWAN.

3.5.2.2 Study site

We used an unstructured mesh for wave numerical model to accurately describe the complex shoreline geometry in the Nin Bay and surrounding area (Figure 121). Similarly, studies that used grids coarser than 2 km recommend the use of unstructured grids to accurately resolve complex shoreline features, especially in the presence of islands and complex topography due to their sheltering effect (Perez et al., 2017). On the other hand, the unstructured grid allows the use of coarser elements away from the coastline to save computational costs for larger domains (Pallares et al., 2017). In particular, the Mediterranean Sea has a complicated morphology and environment, including a very complex coastline, highly variable bathymetry, and limited fetches. Therefore, an unstructured mesh allows flexible local refinement that can improve the accuracy of wave simulation for specific nearshore areas (Vannucchi et al., 2021). The domain of the numerical model in this study covers part of the eastern Adriatic Sea and extends over 14.8° E – 15.2° E in longitude and 44.2° N – 44.6° N in latitude.

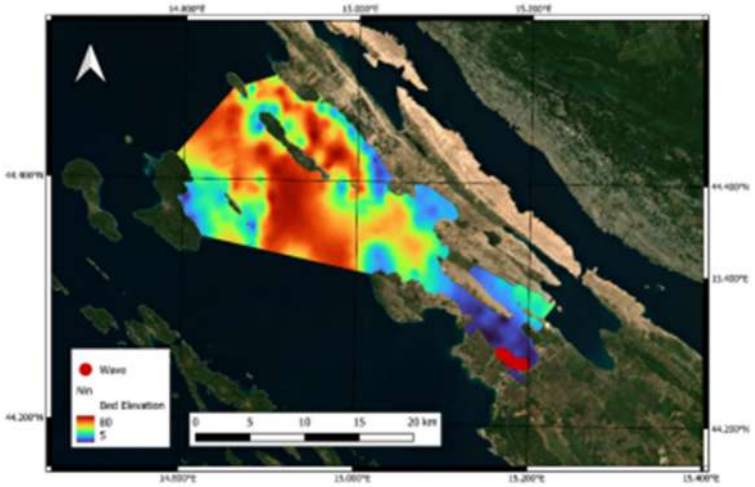

Figure 120 Map of the regional model on the Croatian coast (mid-latitude Adriatic), showing 5 numerical wave stations (red circle); the map is shown in the coordinate reference system EPSG: 4326 - WGS 84.

The source of the basic bathymetric data is the latest GEBCO database (Weatherall et al., 2015). In addition, local bathymetry measurements or publicly available chart data from NAVIONICS were added to the nearshore baseline data to provide finer resolution of the coastline. The resolution of

the baseline bathymetric data is approximately 200m x 200m offshore, while the resolution of the nearshore was finer at 5m x 5m. To accurately represent the complex coastal geography, the spatial resolution of the nearshore data is 5 m. The unstructured grid area consists of 20723 triangular elements, with grid elements decreasing in size to the shoreline. The depth of the deepest water is about 80 m below mean sea level (MSL) at the western open boundary (Figure 121).

3.5.2.3 Initial/boundary conditions and model parameterization

SWAN makes the input parameters and the choice of empirical formulations and their constants flexible for the user. Therefore, it is possible to develop an accurate modelling system for a given region by carefully listing the formulations included in the model and calibrating them (Liang et al., 2014).

In the SWAN model setup, the formulations for the source terms from equations in the previous section are adopted from the selection of formulations provided as part of the SWAN package. SWAN default formulations are chosen for the nonlinear quadruplet wave interactions that adopts the Discrete Interaction Approximation (DIA) formulation (Hasselmann et al., 1985), the breaker index formulation (Battjes and Janssen, 1978), the JONSWAP bottom friction formulation (Hasselmann, 1973), and the triad wave-wave interaction that using the Lumped Triad Approximation (Eldeberky, 1996) since our domain includes intermediate depth and shallow water areas. A summary of the empirical formulas and parameter values used is shown in Table 26.

The wind energy input term in SWAN, S_{in} in source equations, is defined as the sum of the linear and exponential growth terms. The linear term is based on the study of Cavaleri and Rizzoli (1981), while there are several expressions available for the exponential term. First, Komen and Hasselmann (1984) adopted the expression of Snyder et al. (1981) to introduce a revised formulation expressed in terms of the friction velocity. Moreover, Janssen proposed a new quasi-linear wind wave formulation (Janseen, 1989; 1991). On the other hand, the wave dissipation term, S_{ds} in source equations determines the amount of white-capping dissipation in the domain. Komen and Hasselmann (1984) formulated the pressure pulse model for white-capping, which is the default formulation in SWAN. However, in this work, the white-capping formulation in conjunction with the wind energy input formulation given by Janseen (1989; 1991). This choice is due to the successful application of the Janssen formulation in recent research in the Mediterranean (Amarouche et al., 2019; 2022).

Table 26 Summary of used empirical formulations and parameter values

SWAN parameter setting	Formulation	Par. value	Determination method
Directional standard deviation	-	2	Literature [1]
Directional wave resolution	-	36 bins or 72 bins	Literature [1] and Calibration procedure (section 2.6)
Frequency range	-	0.05 – 4 Hz	Literature [1]
Number of spectral frequencies	-	30 bins	Literature [1]
Triad constant *trfac*	Eldeberky [10]	0.05	
Triad constant *cutfr*	Eldeberky [10]	2.5	
Quadruplet constant C_{nl4}	Hasselmann, Hasselmann [7]	3×10^7	Literature [1, 18]
Quadruplet constant λ	Hasselmann, Hasselmann [7]	0.25	Literature [1, 18]
Breaking constant α	Battjes and Janssen [8]	1.00	Literature [1, 18]
Breaking constant γ	Battjes and Janssen [8]	0.73	Literature [1, 18]
Bottom friction C_{fric}	Hasselmann [9]		
Number of iterations	-	1 iteration	Literature [19-21]
Time step size	-	10 min	Literature [16, 20, 22]
White-capping δ parameter	Janssen [14], Janssen [15]	1	Literature [16, 19, 23]
White-capping parameter C_{ds}	Janssen [14], Janssen [15]		Calibration procedure (section 2.6)

The Janssen white-capping formulation requires the input of 2 parameters, δ and C_{ds}. The value for the δ-parameter determines the dependence of the white-capping on the wave number. Komen and Hasselmann (1984) originally suggested a value of 0.5, but recent research showed more accurate model results with a value of 1.0 (Rogers et al., 2003). The latter recommendation is used in this paper.

The model is run in non-stationary mode with a time step of 10 minutes and up to 1 iteration per time step, while outputs are generated and saved hourly and are written in ASCII format inside a text file. The wave simulation model for calibration purposes is run for a period the measuring campaign (December 16, 2022, to February 3, 2023). The first 3 days are considered as model warm-up from a cold-start and are not considered in the evaluation of model performance. This is considered appropriate for the region in question because winter storms are prevalent in the Adriatic Sea, with long periods of calm between, and there were relatively strong wave storms

during this period. The validated model is subsequently run with the calibrated white-capping coefficient to obtain a long time series of wave parameters along several numerical wave measuring locations.

The new fifth generation atmospheric reanalysis, ERA5 (Hersbach et al., 2020), is used as the forcing wind dataset in the wave numerical model. ECMWF has developed the dataset itself and distributed it through the Copernicus service, which increases the demands on the reanalysis product. Coastal wind accuracy has increased since ERA-Interim as advances have been made in model formulation and technical capabilities. The ERA5 wind dataset obtained has an hourly time resolution and a spatial resolution of 0.25° (31 km) in both latitude and longitude. Due to a commonly cited underprediction of the wind magnitudes of reanalysis climate models, the ERA5 wind magnitudes have been multiplied with a factor of 1.5 (Wu et al.,2021; Davison et al., 2019) . This increased wind magnitude will be counterbalanced by a higher calibrated white-capping, which would ultimately provide an adequate interpretation of the wave field.

We used a wider region for the wind forcing data set than for the numerical wave model itself to ensure that every numerical cell has an appropriate amount of surrounding wind data points to interpolate from (Figure 53).

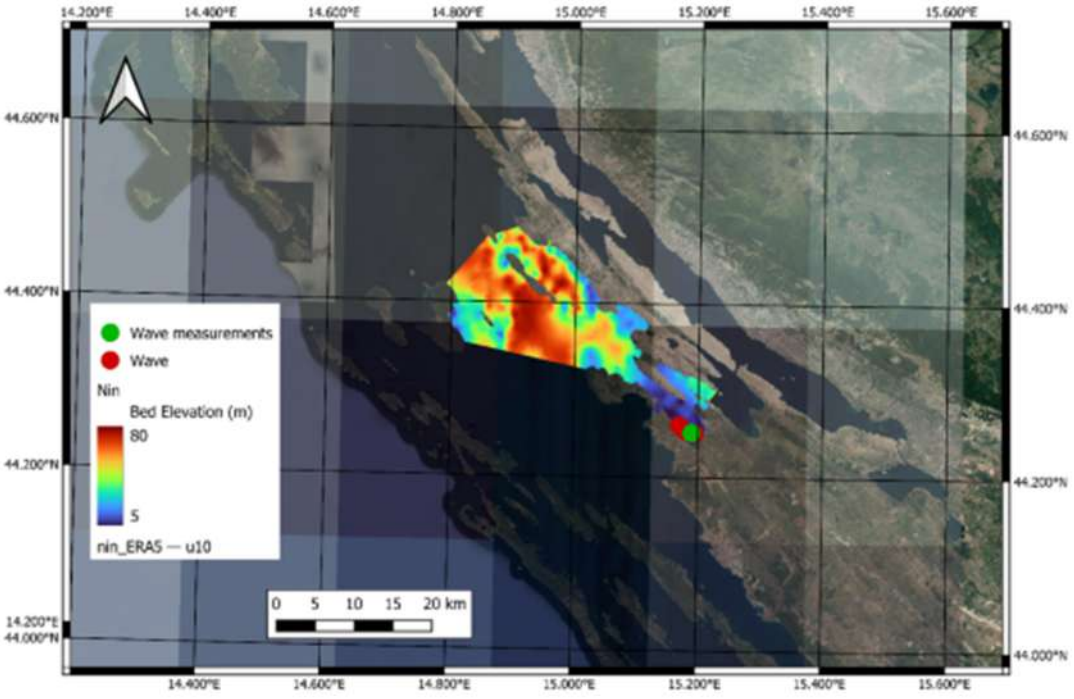

Figure 121 Map of the regional model on the Croatian coast (mid-latitude Adriatic) showing a broader area than just the numerical model with the ERA5 grid shown with transparent rectangles; 3 numerical wave stations (red circle) and 1 wave stations for wave measurements (green circle); the map is shown in the coordinate reference system EPSG: 4326 - WGS 84.

3.5.2.4 Wave numerical model calibration using filed measurements

As a crucial parameter in the numerical model calibration procedure, the white-capping dissipation coefficient C_{ds} stands out. Several previous wave-hindcast studies have shown that the default C_{ds} in the SWAN setup often leads to results that need to be validated (Akpinar and Bingolbali, 2016; Cavaleri et al., 2018). Since C_{ds} is the least known physical term of the SWAN wave model, it is commonly used as a tuning parameter within the calibration procedure (Cavaleri et el., 2018; 2020). This simple solution aims to minimize the discrepancy between simulated and measured significant wave height due to errors in the wind fields. Even though this method does not have a valid physical background, since the simulated white-capping dissipation may not reflect the realistic conditions, this procedure is quite efficient for solving realistic wave simulations.

A surrogate model was developed to define the automated procedure of the C_{ds} calibration. The algorithm of this model uses Radial Basis Functions (RBF) to construct a low-cost model for the objective function interpolation (Regis and Shoemaker, 2007; Gutmann, 2001). The procedure itself involves occasional calls to the SWAN numerical model to evaluate the objective function near the current incumbent point. The maximum number of calls to the SWAN model that the surrogate model processes, is fixed at 10, after which the calibration algorithm is stopped. The surrogate model iterates the C_{ds} value to minimize the loss function defined by the error equation for calculating the *HH* index, between the wave model predicted significant wave heights and measured wave heights (measuring campaign from December 16, 2022, to February 3, 2023 and the location of the measuring wave buoy shown in green in Figure 123). The search range for the white-capping parameter C_{ds} varies between 0 and 5, as the white-capping parameter is commonly limited to this range in formulation by Janssen (1989, 1991)

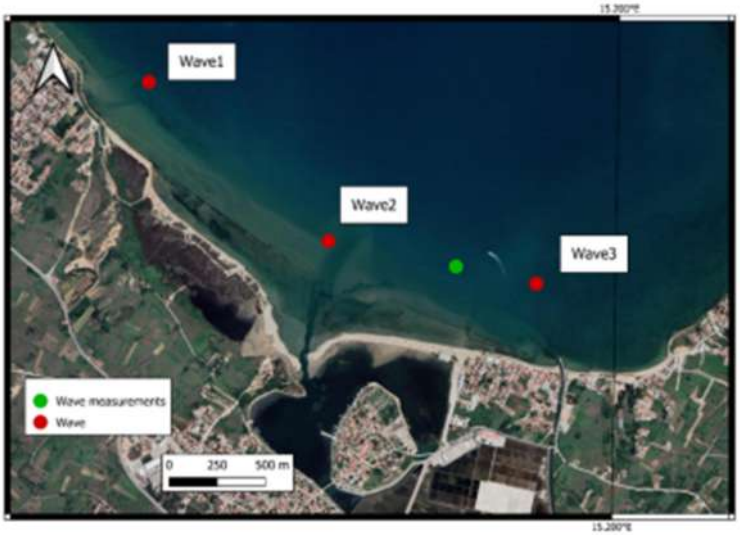

Figure 122 Map of the Nin Bay with green circle indicating the location of the wave buoy and red circles indicating extraction points (Wave1, Wave2 and Wave3) from the wave numerical model for calculating the long-term forecasting

SWAN model uncertainty is examined by the Pearson correlation coefficient (*R*), the corrected indicator *HH* proposed by Hanna and Heinold (1985), the normalized bias (*NBIAS*), and the normalized root mean square error (*NRMSE*), defined in equations (1)–(4) respectively.

In the following text, we present the result of the white-capping parameter calibration procedure described. For the calibration procedure, 10 simulations of the numerical model were run with various white-capping coefficients during the measuring campaign from December 16, 2022, to February 3, 2023.

The results of the surrogate optimization reached a global minimum of the *HH* performance metric at a value of 1.25. The algorithm showed a significant difference between the value of the calibrated white-capping parameter for this case and the SWAN default value for the white-capping coefficient of 4.5 for the Janssen (1991) formulation.

Performance metrics of the accuracy of the calibrated wave numerical model against the measured significant wave heights is shown in Figure 123 and Figure 124. The figure shows a satisfactory accuracy that is in line with research articles in the region (Bujak et al., 2023).

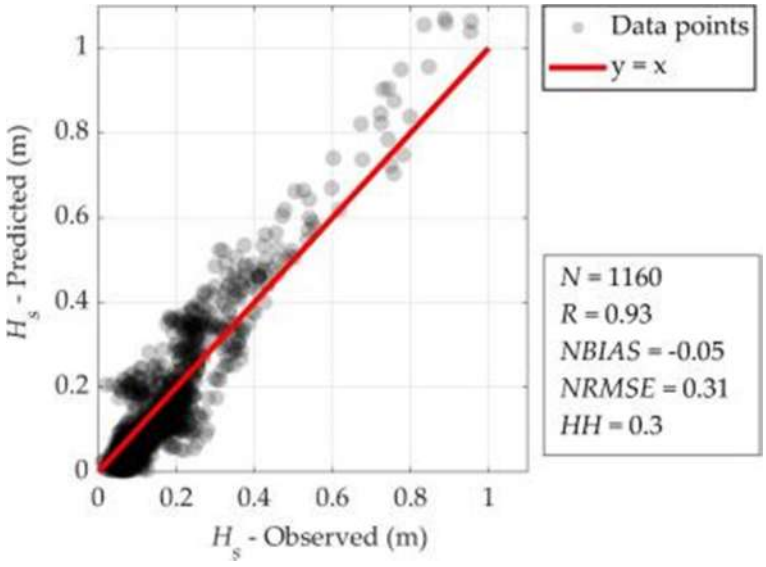

Figure 123 Scatter diagram and performance metrics showing the agreement between the simulated significant wave heights and measured significant wave during the calibration period (December 16, 2022, to February 3, 2023)

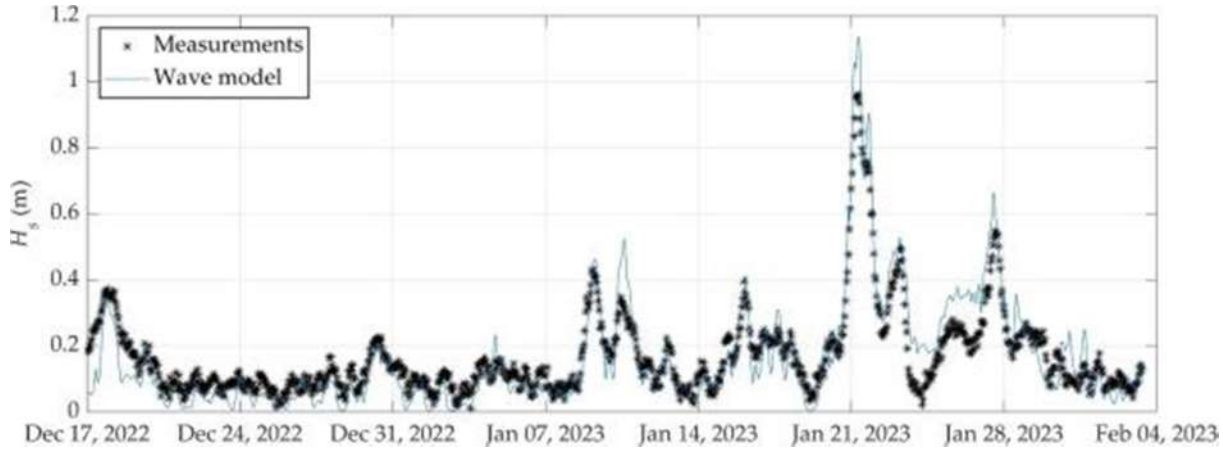

Figure 124 Time series excerpt of measured wave parameters at wave buoy location and modelled wave parameters during the measuring campaign (December 16, 2022, to February 3, 2023)

3.5.2.5 Wave numerical model simulation for the period 2006-2023

A long-term wave simulation with the calibrated numerical model is done to obtain a relatively long time series of wave parameters on 3 locations (red dots in Figure 122). The wave simulation is conducted for the period of 2006-2023, which will provide a 17 year long wave time series. Wave roses of the resulting wave simulation are shown in Figure 125, Figure 126, and Figure 127.

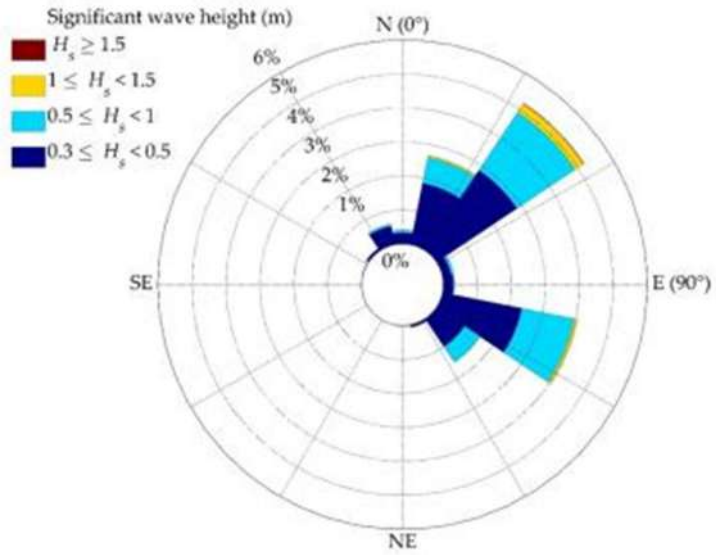

Figure 125 Wave rose of the numerically obtained significant wave heights from the western extraction point (Wave1 shown in Figure 122) for the simulation period of 2006-2023

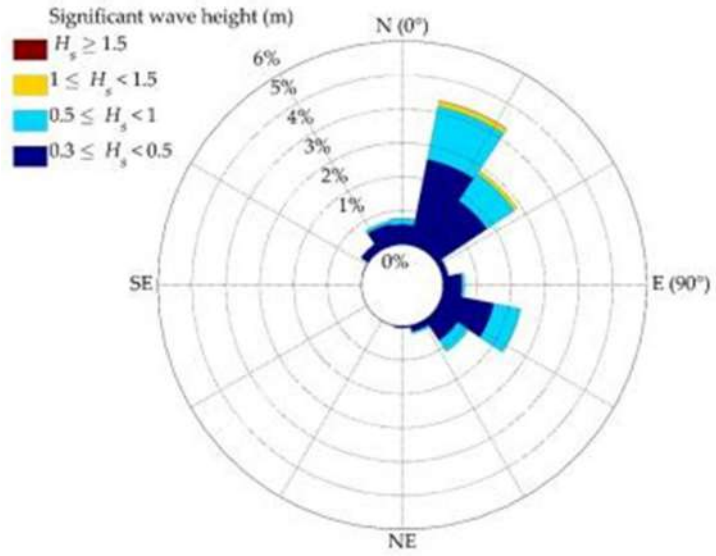

Figure 126 Wave rose of the numerically obtained significant wave heights from the centre extraction point (Wave2 shown in Figure 122) for the simulation period of 2006-2023

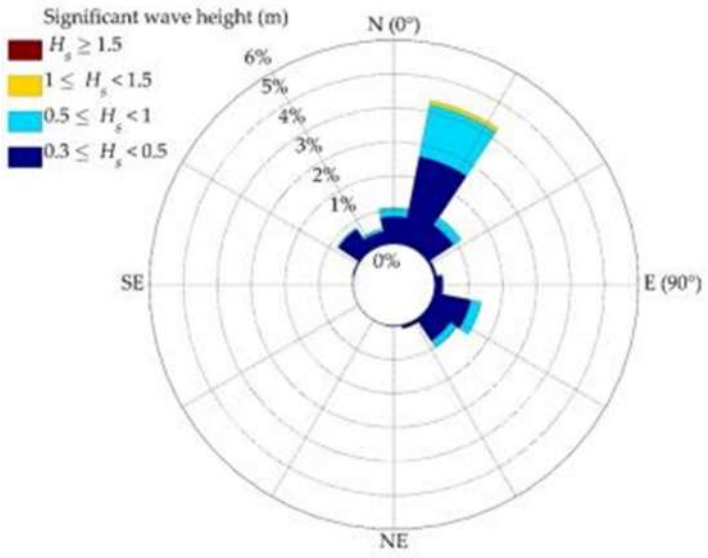

Figure 127 Wave rose of the numerically obtained significant wave heights from the western extraction point (Wave3 shown in Figure 122) for the simulation period of 2006-2023

Most of the time the wave climate is calm, with only two directions with wave frequencies above 2% for wave higher than H_s > 0.3 m. The significant wave height at the Nin Bay is primary arriving from two directions, the N-NE direction and the E-SE direction. We will refer to these two directions from now on as Sector I (N-NE) and Sector II (E-SE). The maximum significant wave height is higher for the Sector I, with value rising to 1.91 m at the most extreme during the simulation period (5.3.2015. 17:00, the corresponding wave field is shown in the Appendix).

The following figures (from Figure 128 to Figure 133) show the relationship between the significant wave height and the peak wave period for each respective sector I (N-NE direction) and sector II (E-SE direction). This relationship is used to determine the associated peak wave period values that correspond to the high return period significant wave heights after wave forecasting.

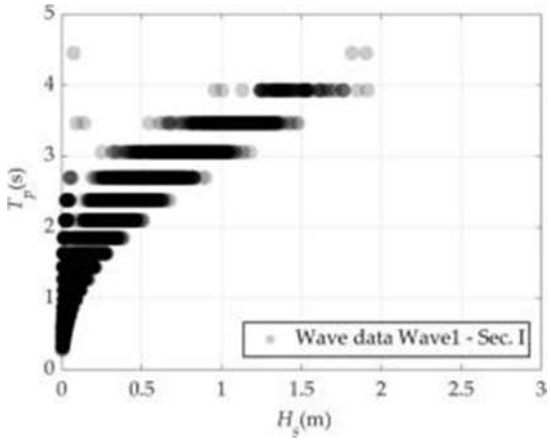

Figure 128 Scatter diagram between the significant wave heights and peak wave periods from the eastern extraction point in the direction of Sector I (Wave1 shown in Figure 122) for the simulation period of 2006-2023

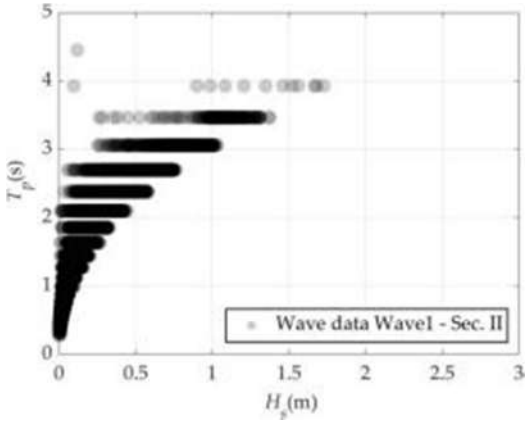

Figure 129 Scatter diagram between the significant wave heights and peak wave periods from the eastern extraction point in the direction of Sector II (Wave1 shown in Figure 122) for the simulation period of 2006-2023

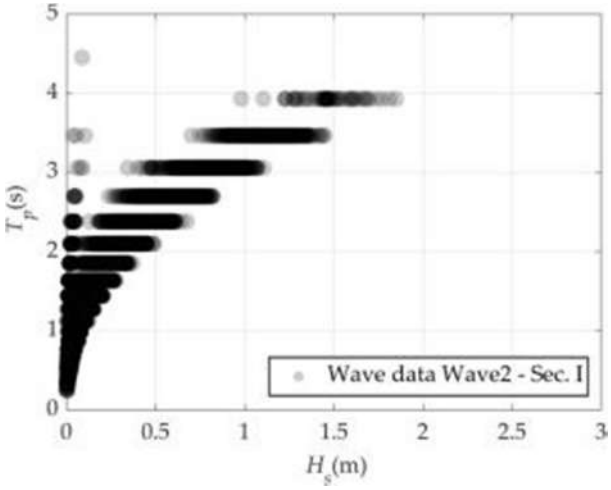

Figure 130 Scatter diagram between the significant wave heights and peak wave periods from the centre extraction point in the direction of Sector I (Wave2 shown in Figure 122) for the simulation period of 2006-2023

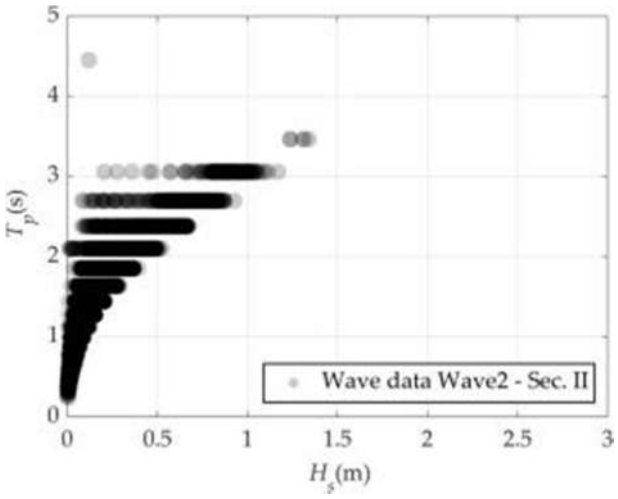

Figure 131 Scatter diagram between the significant wave heights and peak wave periods from the eastern extraction point in the direction of Sector II (Wave2 shown in Figure 122) for the simulation period of 2006-2023

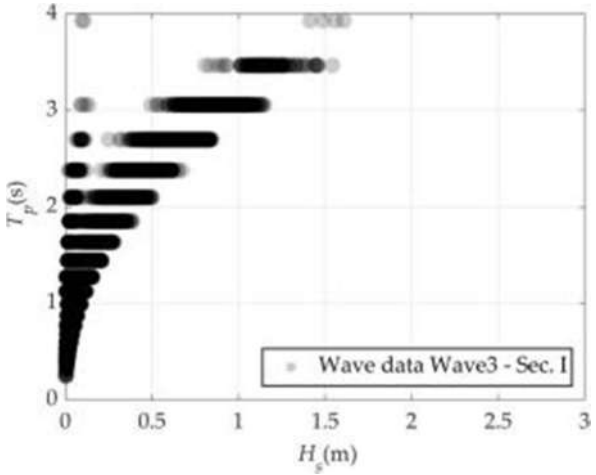

Figure 132 Scatter diagram between the significant wave heights and peak wave periods from the western extraction point in the direction of Sector I (Wave3 shown in Figure 122) for the simulation period of 2006-2023

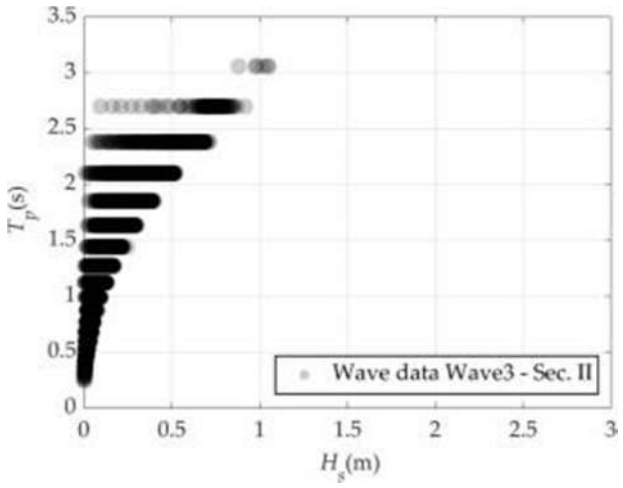

Figure 133 Scatter diagram between the significant wave heights and peak wave periods from the western extraction point in the direction of Sector II (Wave3 shown in Figure 122) for the simulation period of 2006-2023

3.5.2.6 Long-term wave prediction

Wave forecasting is a procedure for determining statistically representative wave parameters (significant wave height and peak wave period) in deep water caused by wind. To the predicted wave parameters, the wave direction is associated in accordance with the direction of the sector (fetch direction). In this study, there are two significant wave direction (Sector I and Sector II). All derived wave forecasts are valid for that location of interest the long-term wave time series was analysed.

As there are simulated wave data for three distinct locations in the Nin Bay, Croatia for a long-term period (2006 – 2023), this data is used to conduct long-term wave forecasting in this study.

The peak-over-threshold (POT) method has been widely used to estimate the return values of extreme waves. In this method, an extreme event is defined as successive significant wave heights above a threshold value. This extreme event is often called a “storm” and the peak or the highest value of this “storm” is referred to as an extreme wave.

We will use a threshold defined as the significant wave hight occurring at the wind velocity V ≥ 5.5-7.9 (m/s) (or ≥ 4 Bf) at the 3 km long fetch (fetch length in the NE direction from the city of Nin, Croatia). In this way, we separate peak significant wave height values. From this set, the peak-over-threshold (POT) method (common for wave data sets between 10 and 30 years) of a significant wave height variable is coupled with a log normal distribution to perform long- term forecasting.

The resulting histograms that separate the occurrences of the above threshold significant wave height into bins, ready to further evaluate long-term forecasting are shown from Figure 134 to Figure 139.

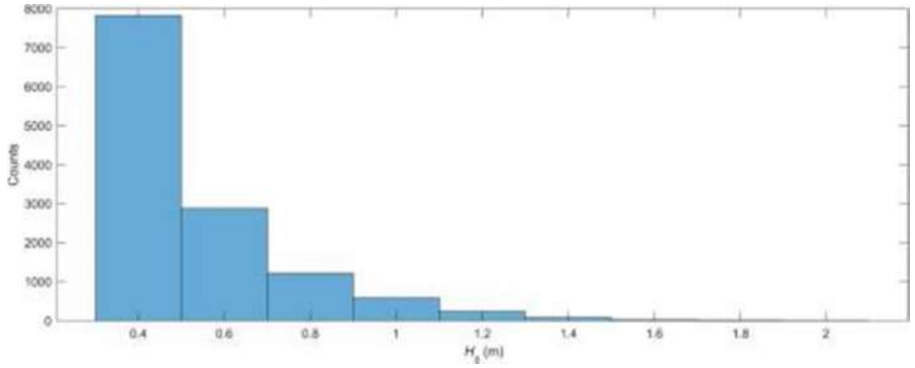

Figure 134 Histogram of significant wave heights above the threshold of H_s = 0.3 m for the simulation period of 2006-2023 with their corresponding count for each bin for the eastern extraction point in Sector I (Wave1 shown Figure 123)

Table 27 Above threshold significant wave heights for the simulation period of 2006-2023 with their corresponding frequency for each bin and the probability of exceedance for the eastern extraction point in Sector I (Wave1 shown Figure 122)

Rank	Wave height range	Mean significant wave height	Absolute frequency	Cumulative absolute frequency	Probability of exceeding
	d Hs - u Hs	Hs,i	fi	Fi	P(Hs>Hs,i) = (2Fi-1)/2n
	(m)	(m)	(1)	(1)	(1)
1	0.3-0.5	0.4	7820	12838	1.000
2	0.5-0.7	0.6	2875	5018	0.391
3	0.7-0.9	0.8	1216	2143	0.167
4	0.9-1.1	1.0	579	927	0.072
5	1.1-1.3	1.2	234	348	0.027
6	1.3-1.5	1.4	77	114	0.009
7	1.5-1.7	1.6	27	37	0.003
8	1.7-1.9	1.8	8	10	0.001
7	1.9-2.1	2.0	2	2	0.000

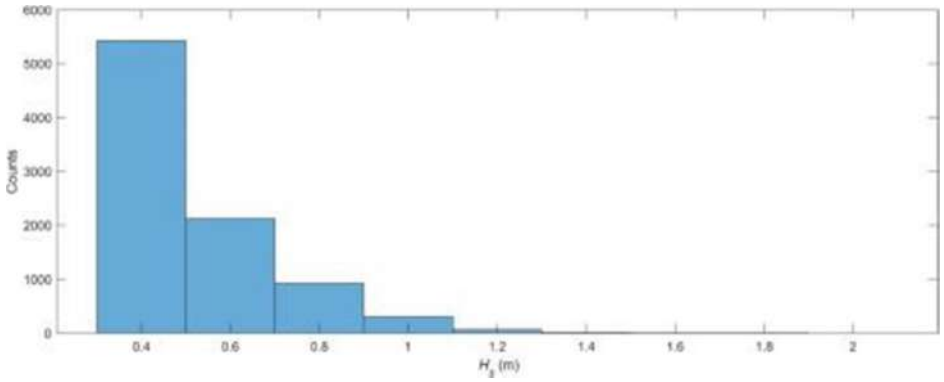

Figure 135 Histogram of significant wave heights above the threshold of H_s = 0.3 m for the simulation period of 2006-2023 with their corresponding count for each bin for the eastern extraction point in Sector II (Wave1 shown Figure 123)

Table 28 Above threshold significant wave heights for the simulation period of 2006-2023 with their corresponding frequency for each bin and the probability of exceedance for the eastern extraction point in Sector II (Wave1 shown Figure 122)

Rank	Wave height range	Mean significant wave height	Absolute frequency	Cumulative absolute frequency	Probability of exceeding
	d Hs - u Hs	Hs,i	fi	Fi	P(Hs>Hs,i) = (2Fi-1)/2n
	(m)	(m)	(1)	(1)	(1)
1	0.3-0.5	0.4	5430	8854	1.000
2	0.5-0.7	0.6	2124	3424	0.387
3	0.7-0.9	0.8	923	1300	0.147
4	0.9-1.1	1.0	300	377	0.043
5	1.1-1.3	1.2	63	77	0.009
6	1.3-1.5	1.4	9	14	0.002
7	1.5-1.7	1.6	4	5	0.001
8	1.7-1.9	1.8	1	1	0.000
7	1.9-2.1	2.0	0	0	0.000

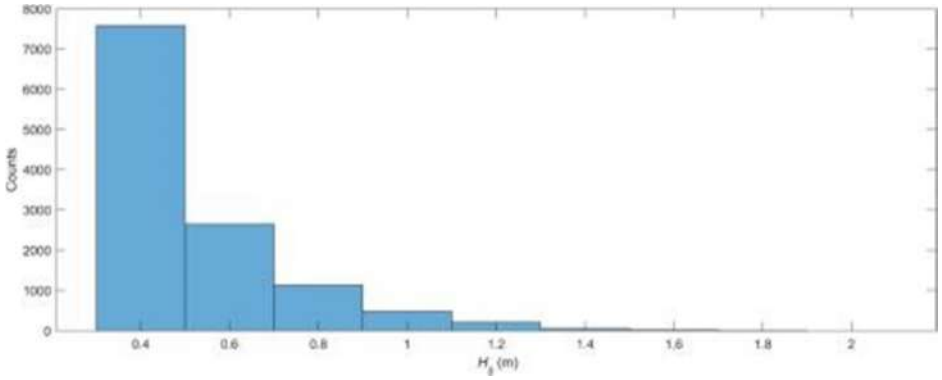

Figure 136 Histogram of significant wave heights above the threshold of H_s = 0.3 m for the simulation period of 2006-2023 with their corresponding count for each bin for the centre extraction point in Sector I (Wave2 shown Figure 123)

Table 29 Above threshold significant wave heights for the simulation period of 2006-2023 with their corresponding frequency for each bin and the probability of exceedance for the centre extraction point in Sector I (Wave2 shown Figure 122)

Rank	Wave height range	Mean significant wave height	Absolute frequency	Cumulative absolute frequency	Probability of exceeding
	d Hs - u Hs	Hs,i	fi	Fi	P(Hs>Hs,i) = (2Fi-1)/2n
	(m)	(m)	(1)	(1)	(1)
1	0.3-0.5	0.4	7582	12131	1.000
2	0.5-0.7	0.6	2653	4549	0.375
3	0.7-0.9	0.8	1134	1896	0.156
4	0.9-1.1	1.0	475	762	0.063
5	1.1-1.3	1.2	214	287	0.024
6	1.3-1.5	1.4	53	73	0.006
7	1.5-1.7	1.6	16	20	0.002
8	1.7-1.9	1.8	4	4	0.000
7	1.9-2.1	2.0	0	0	0.000

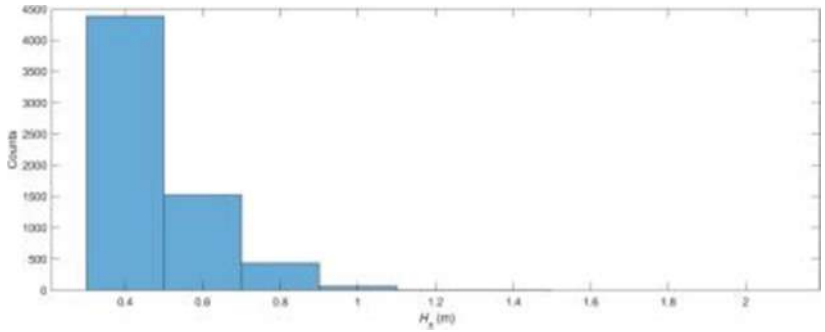

Figure 137 Histogram of significant wave heights above the threshold of H_s = 0.3 m for the simulation period of 2006-2023 with their corresponding count for each bin for the centre extraction point in Sector II (Wave2 shown Figure 123)

Table 30 Above threshold significant wave heights for the simulation period of 2006-2023 with their corresponding frequency for each bin and the probability of exceedance for the centre extraction point in Sector II (Wave2 shown Figure 122)

Rank	Wave height range	Mean significant wave height	Absolute frequency	Cumulative absolute frequency	Probability of exceeding
	d Hs - u Hs	Hs,i	fi	Fi	P(Hs>Hs,i) = (2Fi-1)/2n
	(m)	(m)	(1)	(1)	(1)
1	0.3-0.5	0.4	4384	6409	1.000
2	0.5-0.7	0.6	1525	2025	0.316
3	0.7-0.9	0.8	432	500	0.078
4	0.9-1.1	1.0	61	68	0.011
5	1.1-1.3	1.2	4	7	0.001
6	1.3-1.5	1.4	3	3	0.000
7	1.5-1.7	1.6	0	0	0.000
8	1.7-1.9	1.8	0	0	0.000
7	1.9-2.1	2.0	0	0	0.000

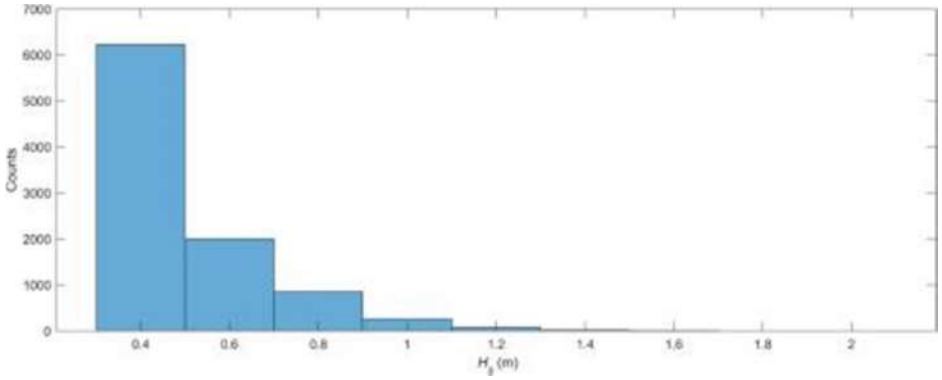

Figure 138 Histogram of significant wave heights above the threshold of H_s = 0.3 m for the simulation period of 2006-2023 with their corresponding count for each bin for the western extraction point in Sector I (Wave3 shown Figure 123)

Table 31 Above threshold significant wave heights for the simulation period of 2006-2023 with their corresponding frequency for each bin and the probability of exceedance for the western extraction point in Sector I (Wave3 shown Figure 122)

Rank	Wave height range	Mean significant wave height	Absolute frequency	Cumulative absolute frequency	Probability of exceeding
	d Hs - u Hs	Hs,i	fi	Fi	P(Hs>Hs,i) = (2Fi-1)/2n
	(m)	(m)	(1)	(1)	(1)
1	0.3-0.5	0.4	6225	9440	1.000
2	0.5-0.7	0.6	2000	3215	0.341
3	0.7-0.9	0.8	849	1215	0.129
4	0.9-1.1	1.0	262	366	0.039
5	1.1-1.3	1.2	85	104	0.011
6	1.3-1.5	1.4	16	19	0.002
7	1.5-1.7	1.6	3	3	0.000
8	1.7-1.9	1.8	0	0	0.000
7	1.9-2.1	2.0	0	0	0.000

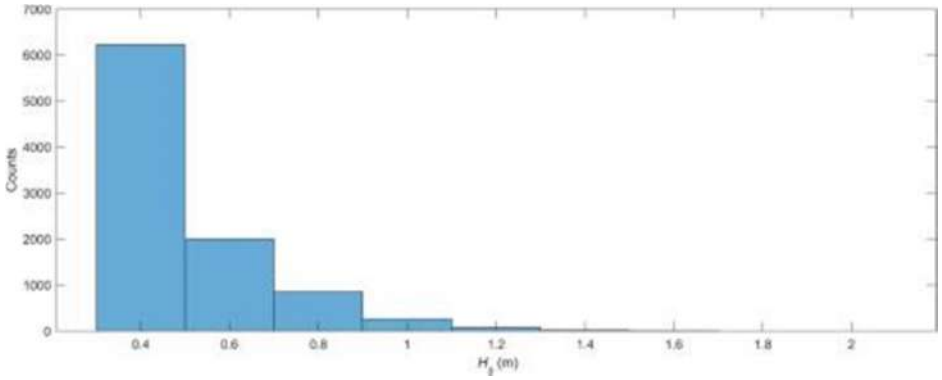

Figure 139 Histogram of significant wave heights above the threshold of H_s = 0.3 m for the simulation period of 2006-2023 with their corresponding count for each bin for the western extraction point in Sector II (Wave3 shown Figure 122)

Table 32 Above threshold significant wave heights for the simulation period of 2006-2023 with their corresponding frequency for each bin and the probability of exceedance for the western extraction point in Sector II (Wave3 shown Figure 122)

Rank	Wave height range	Mean significant wave height	Absolute frequency	Cumulative absolute frequency	Probability of exceeding
	d Hs - u Hs	Hs,i	fi	Fi	P(Hs>Hs,i) = (2Fi-1)/2n
	(m)	(m)	(1)	(1)	(1)
1	0.3-0.5	0.4	3300	4165	1.000
2	0.5-0.7	0.6	790	865	0.208
3	0.7-0.9	0.8	69	75	0.018
4	0.9-1.1	1.0	6	6	0.001
5	1.1-1.3	1.2	0	0	0.000
6	1.3-1.5	1.4	0	0	0.000
7	1.5-1.7	1.6	0	0	0.000
8	1.7-1.9	1.8	0	0	0.000
7	1.9-2.1	2.0	0	0	0.000

Long-term wave forecasting gives the corresponding return periods of different durations associated with significant wave heights. For this purpose, the ordered pairs [ln $H_{s,i}$ and P ($H_s \geq H_{s,i}$] are plotted, and the log-normal theoretical probability curve (in this case a line) is extrapolated into the low probability region. The probabilities of occurrence P and the return period RP are related through the following equation:

$$P(H_S \geq H_S^{PR}) = \frac{T_{REG}}{n \cdot RP} \quad (8)$$

where:

T_{REG} = period of observation, T_{REG}=17 years for the simulated wave time series (2006 - 2023)

n = number of wave situations

RP = return period

Through extrapolation of the log-normal theoretical probability curve the results of the long-term wave forecast for the return periods of 1, 5, 10, 20, 50 and 100 years are obtained. In addition to the graph showing the linear extrapolation of short-term wind events, a table view of the aforementioned return periods with corresponding significant wave heights is also given.

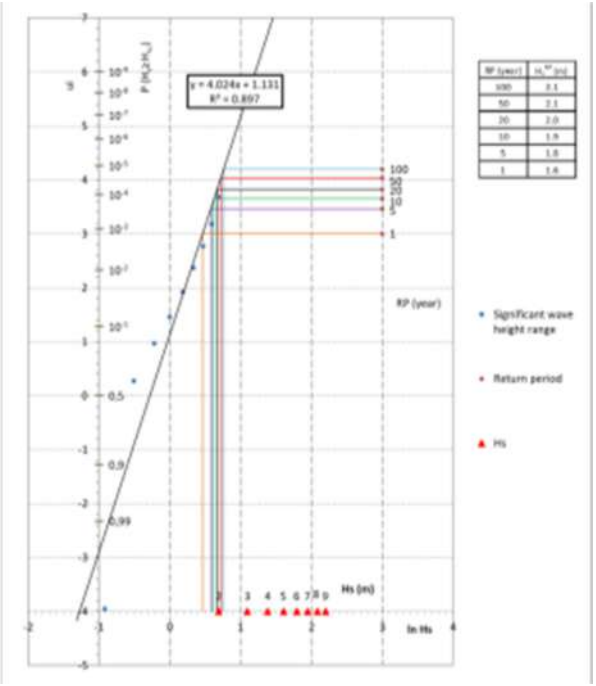

Figure 140 Log-normal probability curve distribution for long-term forecast of significant wave height Hs at the eastern extraction point in Sector I (Wave1 shown in Figure 122)

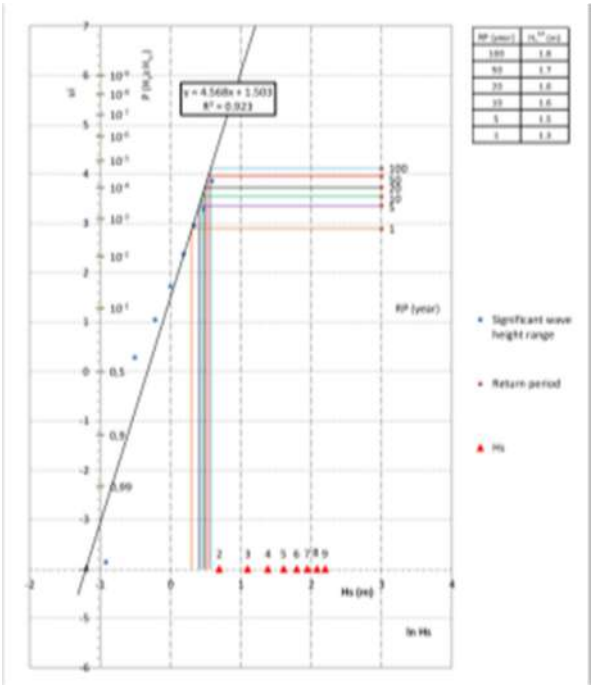

Figure 141 Log-normal probability curve distribution for long-term forecast of significant wave height Hs at the eastern extraction point in Sector II (Wave1 shown in Figure 122)

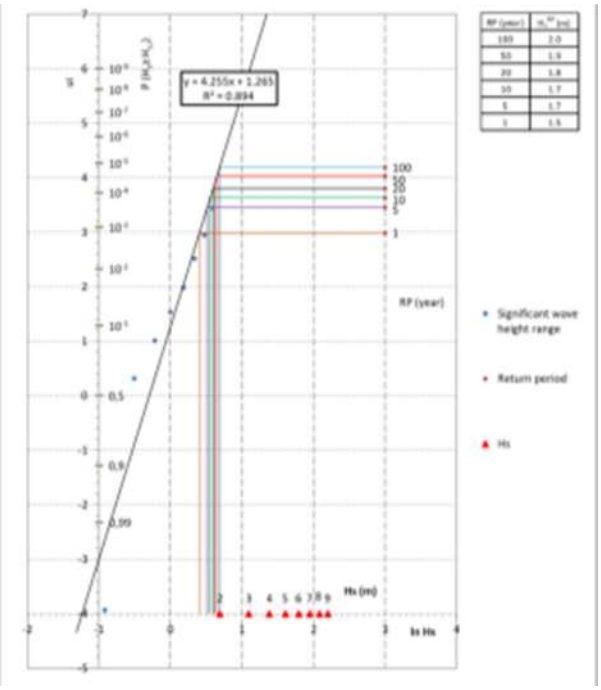

Figure 142 Log-normal probability curve distribution for long-term forecast of significant wave height Hs at the centre extraction point in Sector I (Wave2 shown in Figure 122)

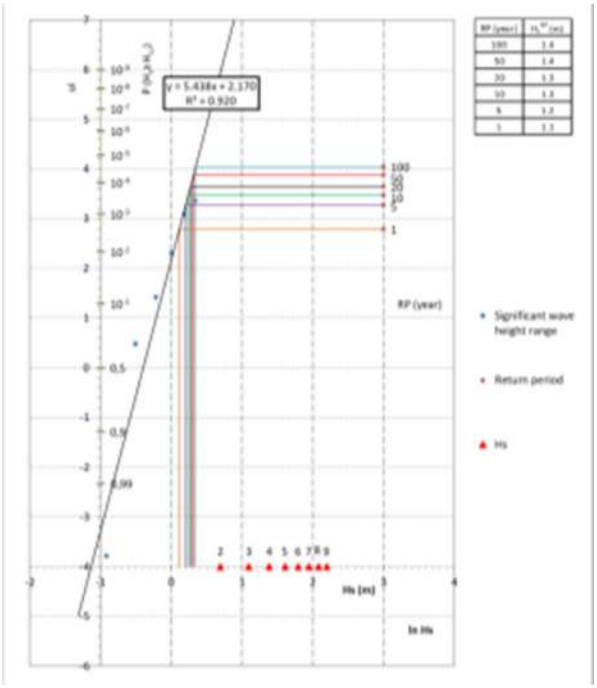

Figure 143 Log-normal probability curve distribution for long-term forecast of significant wave height Hs at the centre extraction point in Sector II (Wave2 shown in Figure 122)

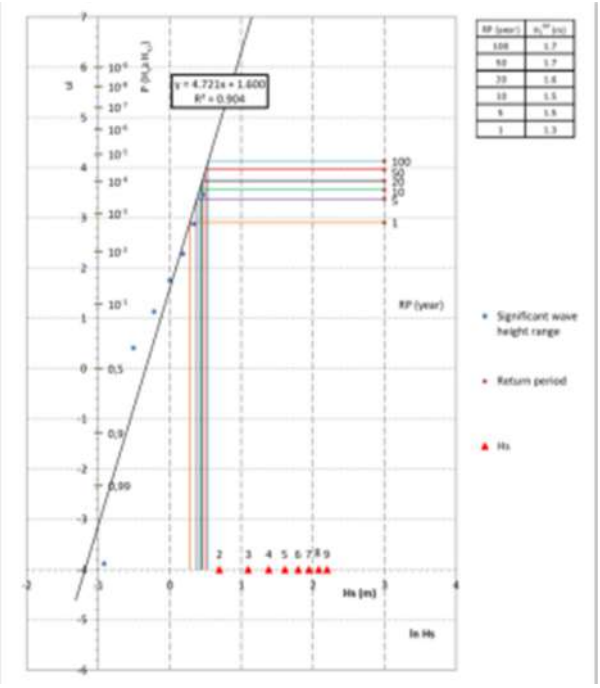

Figure 144 Log-normal probability curve distribution for long-term forecast of significant wave height Hs at the western extraction point in Sector I (Wave3 shown in Figure 122)

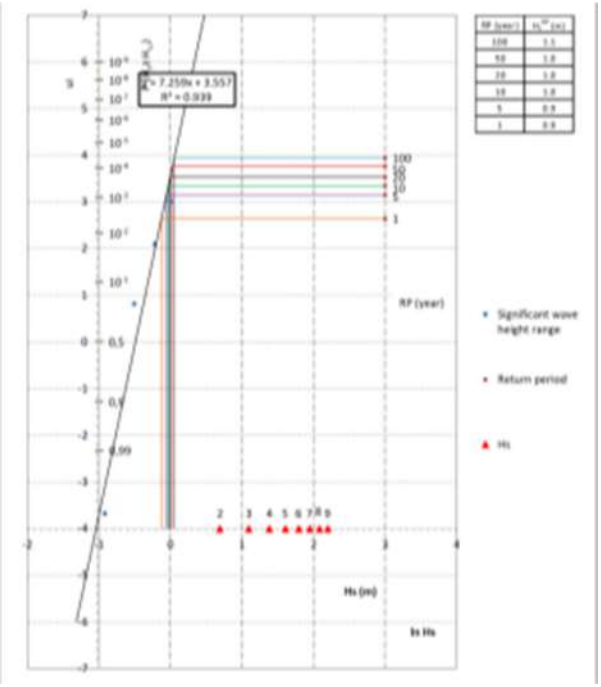

Figure 145 Log-normal probability curve distribution for long-term forecast of significant wave height Hs at the western extraction point in Sector II (Wave3 shown in Figure 122)

3.6 Marche coastal area (IT)

3.6.1 Modeling inundation scenarios

Coastal systems of Marche Region are characterized by low sandy beaches. Residuals coastal biocenosis are endangered by flooding and inundation, that are more frequent and intense in reason of current climate change.

European regulatory framework on flood risks (European directive 2007/60/EC) has imposed the perimeter of the areas subject to flooding systems intended to cope with the phenomena of sea level rise, and the consequent setback of the coasts, which threaten infrastructure and buildings. The purpose of perimeter is to prevent risk plumbing in coastal areas without jeopardizing ecosystems. In particular, the hydraulic hazard is linked to the physical phenomena that interact with the territory and can be evaluated by suitably combining different aspects that characterize the action of the sea on the coast. The combination of these aspects allows the identification of areas characterized by different levels of hazards and their mapping.

This information is essential for coastal ecosystem management, since allows to identify biocenosis directly threatened by flooding and to make coastal management compatible with natural ecosystem's conservation.

The simulations are performed in five pilot areas:

- Pesaro;
- Fano;
- Montemarciano;
- San Benedetto del Tronto;
- Fermo

3.6.2 Model description

The focus of the modelling is the assessment of the inundation perimeters associated to flooding scenarios with return period (Rp) equal to 20, 100 and >100 years (200 years was chosen) for five coastal locations along the Marche Region. Such perimeters were already defined within the "Piano di Gestione Integrata delle Zone Costiere" (PGIZC, 2019) that, following the Direttiva europea 2007/60/CE, computed the hazard maps for coastal inundation associated to high (Rp=20 years), medium (Rp=20 years) and low (Rp>100 years) probability of occurrence. The contributions that were used in the PGIZC to calculate the maximum sea level were: meteorological variations, astronomical tide, set-up, run-up. The climate change effect was accounted for by increasing of 10% the computed water levels. Then, the obtained levels were combined with the DTM model of the Marche Region using the GIS software to find the inundation perimeters.

The objective of the analysis is to verify the perimeters of the PGIZC. To account for climate change effects, the analysis is projected to 2070 under the IPCC RCP8.5 scenario.

Two numerical models are being used, Delft3D and XBeach. Delft3D is a wave-averaged model that provides a description of the wave-forced flow averaged over the wave period. The WAVE module of Delft3D, which uses the third-generation model SWAN as wave-driver, allows one to simulate the wave propagation over large domains in relatively short time. However, it has limitations when dealing with large seabed gradients, like, for example, near harbours or barriers used for coastal protection. Therefore, the wave-resolving model XBeach, which computes velocities and water levels with the wave period , was also used . Delft3D is being used to transfer the wave from a depth of 20 m to a depth of 8-9 m. The resulting wave characteristics are used to force the XBeach model that computes the propagation of the wave towards the shoreline and provided the inundation perimeters.

The wave forcing is derived from the Copernicus Climate Change Service, projected to 2070 under the RCP8.5 scenario and given at 20 m depth. Each domain of interest is covered with two grids. The largest one, with 100 m resolution, extend s towards the offshore until reaching a depth of 20 m, while the size in the alongshore direction i s chosen to avoid that “boundary effects” could affect the dynamic s evolving in the stud y area. The smallest grid has variable size and variable resolution between 5 m or 10 m depending on the site at hand. It follows the coastline shape and extend s in land for few hundred meters to properly model the inundation perimeters. In fact, such grid i s being used also for the XBeach simulations. The wave characteristics are extracted from a point placed at the centre of the smallest grid offshore boundary. The bathymetry is built using some topo-bathymetric sections, a lidar of the Marche Region coastal area, a DTM of the Marche Region and the EMODnet bathymetry. Coastal defence structures are modeled by modifying the seabed height depending on the type of structure (for example, the height of the emerged barriers was fixed at 1.5 m above the mean water level). The wave forcing consist s of a 8 - hours time series that is applied a t the offshore boundary of the largest grid, this because the maximum inundation is reached at the peak of the storm. The wave height is made to reach the peak at the sixth hour, then it decreases. The wave period and direction are taken as constant. To evaluate the influence of the beach profile on the coastal inundation, some one- dimensional runs are being performed varying the beach profile from a “winter-type” to a “summer-type” profile.

The resulting wave characteristics are being used to force the XBeach model. Moreover, the contribution of the Sea Level Rise (SLR), storm surge, meteorological tide, wave set-up and run-up are accounted for. The wave set-up and run-up are directly computed by the model. A sinusoidal tidal timeseries is built and added to an initial water level equal to the sum of SLR and storm surge.

The peak of the tidal time series i s made simultaneous with the storm peak to consider the most pessimistic scenario.

3.6.3 Model development and results

3.6.3.1 Data collection analysis

3.6.3.1.1 Wave Data

Wave data were downloaded from the "Ocean surface wave time series for the European coast from 1976 to 2100 derived from climate projections" dataset of the Copernicus Climate Change Service, which gives hourly values of wave significant height, wave peak period and wave mean direction along the 20 m bathymetric contour, with a resolution of around 30 km.

Time series for the RCP8.5 scenario, which includes the years from 2041 to 2070, were downloaded for the grid points closest to the locations of interest. Then, an extreme value analysis was performed to obtain the wave forcing for the numerical simulations associated to 20, 100 and 200 year-return periods. The first step was to filter the data to identify the storm events. Then the most representative sector for each location was chosen and a bivariate probabilistic analysis was performed. Initially, the two distributions that best adapted to the Hs and Tp data were separately identified. Then, a copula operator was used to find the joint distribution. The graphic results are the so-called "environmental contours", which are curves in the Hs-Tp plane related to different return periods. On such curves, the couple Hs-Tp to force the simulations with was selected by maximizing the energy flux.

3.6.3.1.2 Level Data

Level data were downloaded from the "Water level change time series for the European coast from 1977 to 2100 derived from climate projections" and "Water level change indicators for the European coast from 1977 to 2100 derived from climate projections" datasets of the Copernicus Climate Change Service. From the first dataset, the surge time series for the RCP8.5 scenario (2041-2070) were downloaded to perform an extreme value analysis to find the surges associated with 20, 100 and 200 year-return periods. The maximum astronomical tide was downloaded from the second dataset. The sea level rise for 2070 was set to 0.36 m.

3.6.3.1.3 Topography and bathymetry data

Topography and bathymetry data were provided by the Marche Region. They consisted in:

- High resolution Lidar of the coastal area (0.5m);
- Topo-bathymetric sections, surveyed during both summer and winter periods.

While surveys carried out in summer are used to build the bathymetry for the computational domains, the surveys performed during winter are used to run further simulations to compare the inundation perimeters obtained with a “summer-type” and “winter-type” beach profile.

Such detailed datasets were completed with the online-available EMODnet bathymetry data and DTM of the Marche Region.

3.6.3.2 Wave propagation

Delft3D software was used the wave forcing transfer to the shore. Study areas have been discretized in grids on which the equations of the have been solved. Wave forcing derived from the Copernicus climate dataset is projected to 2070 in the hypothesis of an emission scenario of the RCP8.5 type.

The wave forcing provided by Copernicus refers to a depth of 20 m, which is reached at about 10 km from the Marche coast. Therefore, for all five sites, a first grid aligned with the shoreline was created, which extends out to sea to a depth of 20 m. Parallel to the coast, the grid has been extended enough to avoid "edge effects" that may influence the dynamics in the area of interest. The grid is square mesh, of size 100m 100m.

A second detailed mesh structured grid was then built, with a resolution of about 5m x 5m or 10m x 10m and variable dimensions according to the site in question. This grid follows the course of the coast even more precisely and extends several hundred meters inland from the shoreline in order to model appropriately the flood. This grid was also used in the next phase of modeling with the XBeach software. The two grids have been connected through a nesting procedure, used in the WAVE module to transfer information from an external grid to an internal one.

The following figure shows the example for the site of Fano.

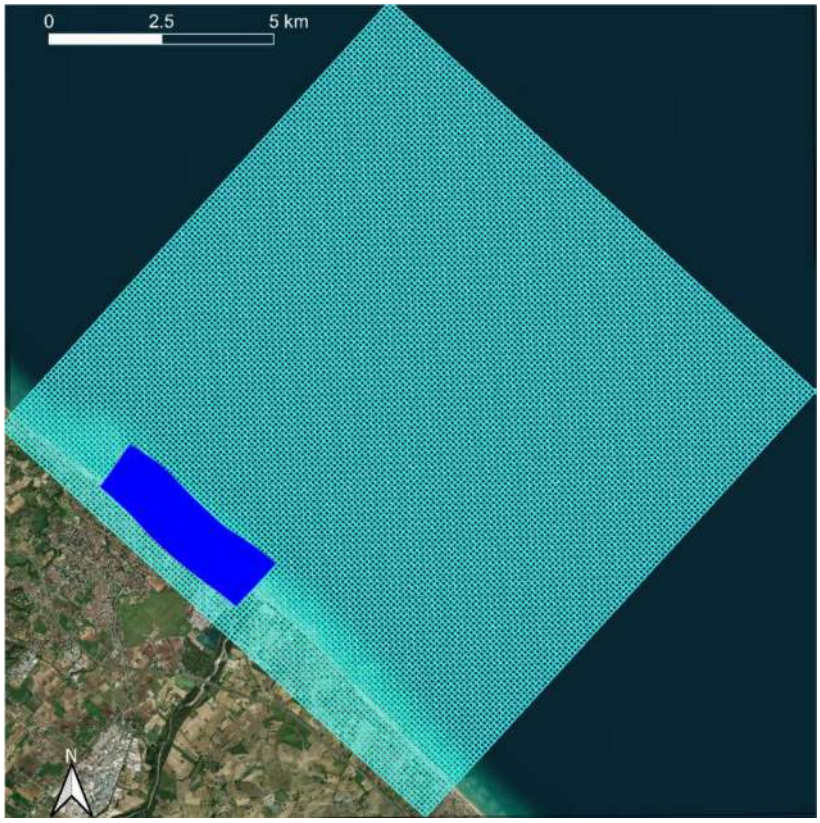

Figure 146 Calculation grids for the case of Fano. In light blue, the external grid used for the Delft3D model. In blue, the internal grid used for both the Delft3D model and the XBeach model.

The coastal defence works have been modeled directly by modifying the elevation of the soil at the grid points inside their perimeter. These quotas have been assigned on the basis of the type of work:

- emerged cliffs: +1.5 m a.s.l.;
- submerged reefs: -0.7 m a.s.l.;
- groynes: +1.5 m a.s.l.;
- submerged groynes: -0.7 m a.s.l.

The following figure shows the bathymetry for the internal grid of Fano.

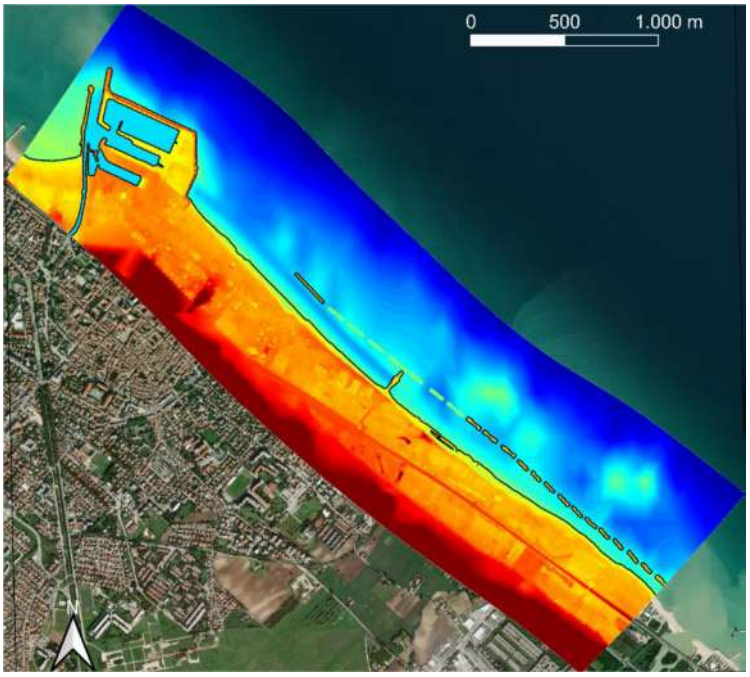

Figure 147 bathymetry for the internal grid of Fano.

The boundary condition imposed on the wide edge of the outer grid consists of a set of waves generated from JONSWAP spectrum in which are imposed the characteristics of significant wave height, peak period, and direction. The series has a total running time of 8 hours. The wave height starts from 1 m, reaches the peak (i.e., the value associated with Tr20/Tr100/Tr200) at the sixth hour and then decreases symmetrically with respect to the ascending branch. The period and direction of the wave were kept constant throughout duration of the simulation.

The 2D spectra constituting the wave forcing of the XBeach model were extracted at a point located at the centre of the offshore edge of the inner grid.

To evaluate the influence of the beach profile on coastal inundation, were performed one-dimensional runs on a section for each site, for which the terrain has been reconstructed using the summer relief once (September-October) and the winter relief once (March April).

Table 33 Wave characteristics for the peak of the simulated storm surge

	Hs (m)			Tp (s)			Dir (°N)
Tr	20	100	200	20	100	200	20,100,200
Pesaro	5.07	5.94	6.29	9.71	10.51	10.88	45

Fano	4.61	5.84	6.36	9.74	10.82	11.30	60
Montemarciano	4.87	6.1	6.63	8.76	8.90	8.92	60
Fermo	4.21	5.23	5.67	10.79	11.82	12.24	105
S. Benedetto del Tronto	4.9	6.07	6.58	10.78	11.63	11.92	105

3.6.3.3 Modeling coastal inundation

The 2D spectra resulting from the Delft3D simulations were used to construct the time series of levels and velocities to be used as boundary conditions in XBeach simulations.

In addition to wave forcing, other contributions were considered to determine the inundation perimeters, such as Sea Level Rise (SLR), storm surge, astronomical tide, set-up, and run-up.

The last two contributions are directly calculated by the numerical model, while SLR, storm surge and tidal were entered as changes in sea level. In particular, for the astronomical tide a sinusoidal series was constructed with a peak corresponding to the maximum value, added to a starting level of the sea surface corresponding to the sum between SLR and storm surge. Assuming the most conservative scenario, the peak of the storm was made to coincide with the maximum of tidal elevation. The simulations are of the hydrodynamic type and, therefore, do not consider the morphodynamic evolution of the seabed.

Table 34 Forcing used in the simulation

	Waves characteristics			SRL + storm surge (m)			tide
Tr	20	100	200	20	100	200	
Pesaro	From Delft3D simulation			1.48	1.67	1.76	0.48
Fano				1.47	1.67	1.76	0.45
Montemarciano				1.39	1.56	1.64	0.37
Fermo				1.29	1.47	1.55	0.33
S. Benedetto del Tronto				1.22	1.35	1.41	0.35

Chapter 4 Conclusions

4.1 Grado and Marano Lagoon, and Gulf of Trieste (IT)

Hindcast and tests results performed to achieve the best modelling system configuration are available at full resolution at the CASCADE PP4 dedicated web page (http://interreg.c3hpc.exact-lab.it/CASCADE/).

In particular, the validation of the model simulation over one year long are presented with specific diagrams and tables that summarize the bias and the correlation of the simulations with the measurements. The validation is supported also with a validation of the boundary conditions and initial conditions that are used for operational forecast.

Further details and quantitative indexes that have been used to achieve the best modelling configuration of the forecasting system developed and implemented in the frame of the project are accessible at: http://interreg.c3hpc.exact-lab.it/CASCADE/

The forecasts are operationally running and the dissemination process is in the final stage. There are ten classes of products for more than one hundred of geographical location for which sea surface physical features and vertical profiles are reposted with hourly resolution. Forecasts covers a five days window and are updated on a daily base, according the availability of the boundary conditions and the forcing data. Those products are available at: http://dati.arpa.fvg.it/fileadmin/CRMA/AA11/SHYFEM_plots/SHYFEM_forecast.php

4.2 Transitional and coastal areas in Emilia Romagna (IT)

Through the implementation of the forecasting system, it is possible to achieve very high-resolution modelling outcomes to provide short-term predictions on the behaviour of the system. Such an application improves the amount of information available for decision makers reaching specific points which are not normally covered by large scale modelling implementations. Besides the improved physical knowledge and forecasting, the biogeochemical aspects have also been addressed which play a very important role for the Sacca di Goro system. With the economic activities developed in the area (e.g., clam farming), the outputs can be used to better define activities to take place and provide information on what should and what should not be done in the time range addressed by the forecasts. Furthermore, the improved knowledge obtained through the biogeochemical model application allows the end users to better comprehend the system and opens new approaches for forthcoming implementations.

4.3 Torre Guaceto-Canale Reale, Punta della Contessa and Melendugno in Puglia (IT)

The modelling and forecasting activities for the Apulia pilot have been developed by means of downscaling procedures at subregional and pilot scales from CMS (Copernicus Marine Service) Mediterranean Near Real Time System, MedFS. The MedFS has provided analysis and short-term forecast of the main physical ocean and wave parameters to the nested models. Investigations on extreme event of sea level and waves at different return time for the entire Adriatic Sea have been performed through the CMS Mediterranean reanalysis products. Maps of sea level and significant wave height for the return period of 10, 25 and 50 years at the coastal nodes have been produced.

First downscaling for circulation and wave models has been performed at the subregional scale of the Adriatic Sea, adopting an unstructured-grid coastal ocean approach with resolution ranging from 2.5km in open sea to 300m at overall coasts.

Then, coastal and pilot modelling downscaling has been focused on the areas of Torre Guaceto-Canale Reale, Punta della Contessa and Melendugno. Due to the continuity between the three Pilots and between the hydrodynamic features, we have adopted a seamless modelling approach for the entire Adriatic coastal waters of Apulia. The area covered by the model designed for the Apulia Pilot scale is the Southern Adriatic Sea with a horizontal resolution ranging from 2.0km in open sea to 30m at overall Apulian coasts. Both systems have been validated with in-situ data and satellite for tracers and waves. The operational chain built for the ocean models in the CASCADE framework is capable every day to provide 3-days of forecasts with hourly frequency.

4.4 Coastal area in Veneto (IT)

Activities performed within the project allowed to obtain a spatially explicit food web model for the Tegnùe di Chioggia area. The work was primarily aimed at investigating the possibilities offered by this type of models in supporting management application. Coherently with this aim the work involved a phase of model development (spatialization), which exploited part of the results of monitoring activities carried out at P5, and an application phase. Results obtained for the current situation (reference scenario) were corroborated by using AIS data. Within further work on the model, an extension of this corroboration activities should be planned.

Overall, results suggest the interest in applying this type of analysis for comparing scenarios produced by alternative management choices. Nonetheless, given the restricted difference in the values calculated for the different indicators in the regions considered, it seems of relevance to extend the effort, by performing an uncertainty analysis of the results obtained. Modelling activities performed reported a high sensitivity of food web indicators to changes in water temperature and

primary production phenology in the area. Further model testing is required, by extending the set of scenarios considered (i.e., changes in fishery pressure in the area) and including the estimation of additional ecological network analysis indicators (e.g., Finn cyclic index).

4.5 Miljašić Jaruga river mouth, Nin bay (HR)

A 3D hydrodynamic model of the Nin Bay and Miljašić Jaruga river has been developed for the analysis of the sea circulation and river flow for the current and planned state of construction in the study area. Additionally, the model has been calibrated based on the temperature measurements on the same location. Due to the constraints in the temporal availability of the input data (mainly related to Miljašić Jaruga discharge time series), the calibration period is considered between December 16th, 2022 and February 2nd, 2023. The second part of the calibration is related to the comparison of video recordings and simulated water extent for the flood event that occurred on September 11th, 2017.

The model calibration related to the analysis of the Sep2017 flood event show successful presentation of the flooding of the left overbank area approximately 40 metres downstream of the road bridge as well as right overbank flow approximately 20 meters upstream of the river mouth. The model failed to simulate the right overbank flow downstream the bridge, but it is justifiable to consider that this area was flooded because of the water approaching from the upstream sections, which were not covered by the domain of this model.

4.6 Marche coastal area (IT)

The model allows to obtain boundaries of inundation with different return period. This is essential for the understanding of threats to coastal ecosystems. Models output make also available information for decision makers at a scale of analysis that is not covered by general models.

Model outputs are used to refine the preliminary boundaries included in the ICMZ and to apply management measures. In addition, model results, together with the monitoring of activity 4.2.1, is useful to check the effectiveness of the actions identified in the ICMZ.

Moreover, model result will increase awareness in policy makers, management bodies and general stakeholders, about the implication of climate change on coastal systems and on the possible adaptation measures.

References

Adriat, A., Karachle, P.K. & Stergiou, K.I. (2014). Diet and feeding habits of Spicara maena and S. smaris in the North Aegean Sea. Acta Adriatica. 55, 75–84.

Aguilar-Manjarrez, J., Soto, D. & Brummett, R. (2017). Aquaculture zoning, site selection and area management under the ecosystem approach to aquaculture. A handbook.

Akpinar, A. and B. Bingolbali, *Long-term variations of wind and wave conditions in the coastal regions of the Black Sea.* Natural Hazards, 2016. **84**(1): p. 69-92.

Altair. (n.d.). *Altair PBS Professional 2020.1 User's Guide*. 2020. https://www.altair.com/pdfs/pbsworks/PBSUserGuide2020.1.pdf

Amarouche, K., et al., *Evaluation of a high-resolution wave hindcast model SWAN for the West Mediterranean basin.* Applied Ocean Research, 2019. **84**: p. 225-241.

Amarouche, K. and A. Akpınar, *Increasing Trend on Storm Wave Intensity in the Western Mediterranean.* Climate, 2021. **9**(1).

Amarouche, K., A. Akpınar, and A. Semedo, *Wave storm events in the Western Mediterranean Sea over four decades.* Ocean Modelling, 2022. **170**.

Andreoli, E., Boscolo, F., Carlin, A., Curiel, D., Gordini, E., Mizzan, L. & Zanetto, M. (2010). Side Scan Sonar mosaics of selected northern Adriatic mesophotic biogenic reefs off Venice (GeoTIFF image). Zenodo. http://doi.org/10.5281/zenodo.4608083

Antunes, P., Karadzic, V., Santos, R., Beça, P. & Osann, A. (2011). Participatory multi-criteria analysis of irrigation management alternatives: The case of the Caia irrigation district, Portugal. Int. J. Agric. Sustain., 9, 334–349.

Ardhuin, F.; Rogers, E.; Babanin, A.V.; Filipot, J.F.; Magne, R.; Roland, A.; Collard, F. Semiempirical dissipation source functions for ocean waves. Part I: Definition, calibration, and validation. J. Phys. Oceanogr. 2010, **40**, 1917–1941.

ARPAV. (2011). Le tegnùe dell 'Alto Adriatico, 206.

Battjes, J.A. and J.P.F.M. Janssen. *Energy loss and set-up due to breaking of random waves*. in *Proceedings of the 16th International Conference on Coastal Engineering*. 1978. Hamburg, Germany.

Bellafiore, D., Umgiesser, G., 2010. Hydrodynamic coastal processes in the north Adriatic investigated with a 3D finite element model, Ocean Dynam., 60, 255–273.

Bellafiore, D., McKiver, W. J., Ferrarin, C., & Umgiesser, G. (2018). The importance of modeling

nonhydrostatic processes for dense water reproduction in the Southern Adriatic Sea. *Ocean Modelling*, *125*, 22–38. https://doi.org/10.1016/j.ocemod.2018.03.001

Bentley, J.W., Serpetti, N. & Heymans, J.J. (2017). Investigating the potential impacts of ocean warming on the Norwegian and Barents Seas ecosystem using a time-dynamic food-web model. Ecol. Modell., 360, 94–107.

Bidlot, J, S Abdalla, and PAEM Janssen (2005). A revised formulation for ocean wave dissipation in CY25R1. In: Internal Memorandum Research Department

Bidlot, JR (2008). Intercomparison of operational wave forecasting systems against buoys: Data from ECMWF, MetO

Bignami, F., S. Marullo, R. Santoleri, and M. E. Schiano, 1995: Longwave radiation budget in the mediterranean sea. J. Geophys. Res, 100 (C2), 2501–2514, doi:10.1029/94JC02496.

B. Buongiorno Nardelli, C. Tronconi, A. Pisano, R. Santoleri, High and Ultra-High resolution processing of satellite Sea Surface Temperature data over Southern European Seas in the framework of MyOcean project, Remote Sensing of Environment, 129, pp 1-16, 2013

Bourdaud, P., Gascuel, D., Bentorcha, A. & Brind'Amour, A. (2016). New trophic indicators and target values for an ecosystem-based management of fisheries. Ecol. Indic., 61, 588–601.

Brigolin, D., Maschio, G.D., Rampazzo, F., Giani, M. & Pastres, R. (2009). An individual-based population dynamic model for estimating biomass yield and nutrient fluxes through an off-shore mussel (Mytilus galloprovincialis) farm. Estuar. Coast. Shelf Sci., 82, 365–376.

Bujak, D., et al., *The Feasibility of the ERA5 Forced Numerical Wave Model in Fetch-Limited Basins.* Journal of Marine Science and Engineering, 2023. **11**(1).

Burchard, H., & Petersen, O. (1999). Models of turbulence in the marine environment —a comparative study of two-equation turbulence models. *Journal of Marine Systems*, *21*(1–4), 29–53. https://doi.org/10.1016/S0924-7963(99)00004-4

Calude, C. & Longo, G. (2015). The Deluge of Spurious Correlations in Big Data. Lois des dieux, des hommes et de la nature, Nantes, France. pp.1-18, ff10.1007/s10699-016-9489-4ff. ffhal01380626

Caressa, S., Gordini, E., Marocco, R., Tunis, G. (2002). Caratteri geomorfologici degli affiornamenti rocciosi del Golfo di Trieste (Adriatico settentrionale). Gortania – Atti Muse Friul. diStoria Nat., 23 (2001), 5-29, ISSN: 0391-5859

Carević, D., Bujak, D., Bogovac, T. (2021): Idejno rješenje rekonstrukcije i numerički model valova ušća Miljašić jaruge (Nin), University of Zagreb, Faculty of Civil Engineering, Zagreb

Carrere L., F. Lyard, M. Cancet, A. Guillot, N. Picot, (2016). FES 2014, a new tidal model – Validation results and perspectives for improvements, presentation to ESA Living Planet Conference, Prague.

Casellato, S. & Stefanon, A. (2008). Coralligenous habitat in the northern Adriatic Sea: An overview. Mar. Ecol., 29, 321–341.

Cavaleri, L. and P.M. Rizzoli, *Wind Wave Prediction in Shallow-Water - Theory and Applications.* Journal of Geophysical Research-Oceans, 1981. **86**(Nc11): p. 961-973.

Cavaleri, L. (2000): The oceanographic tower Acqua Alta — activity and prediction of sea states at Venice, *Coastal Engineering*, 39(1), pp. 29-70.

Cavaleri, L., et al., *Wave modelling in coastal and inner seas.* Progress in Oceanography, 2018. **167**: p. 164-233.

Cavaleri, L., Bajo, M., Barbariol, F., Bastianini, M., Benetazzo, A., Bertotti, L., Chiggiato, J., Davolio, S., Ferrarin, C., Magnusson, L., Papa, A., Pezzutto, P., Pomaro, A., Umgiesser, G. (2019): The October 29, 2018 storm in Northern Italy – An exceptional event and its modeling, *Progress in Oceanography*, 178

Cavaleri, L., Bajo, M., Barbariol, F., Bastianini, M., Benetazzo, A., Bertotti, L., Chiggiato, J., Ferrarin, C., Trincardi, F., Umgiesser, G. (2020): The 2019 flooding of Venice and its implications for future predictions, *Oceanography*, 33, pp. 42-49.

Cavaleri, L., F. Barbariol, and A. Benetazzo, *Wind–Wave Modeling: Where We Are, Where to Go.* Journal of Marine Science and Engineering, 2020. **8**(4)

Chalikov, D. V., and M. Y. Belevich (1993), One-dimensional theory of the wave boundary layer, Bound. Layer Meteor., **63**, 65–96.

Christakos, K., et al., *Modelling wave growth in narrow fetch geometries: The white-capping and wind input formulations.* Ocean Modelling, 2021. **157**.

Christensen, V. & Pauly, D. (1992). ECOPATH II - a software for balancing steady-state ecosystem models and calculating network characteristics. Ecol. Modell., 61, 169–185.

Christensen, V. & Walters, C.J. (2004). Ecopath with Ecosim: Methods, capabilities and limitations. Ecol. Modell., 172, 109–139.

Christensen, V., Coll, M., Steenbeek, J., Buszowski, J., Chagaris, D. & Walters, C.J. (2014).

Representing Variable Habitat Quality in a Spatial Food Web Model. Ecosystems, 17, 1397–1412.

Christensen, V., Guénette, S., Heymans, J.J., Walters, C.J., Watson, R., Zeller, D., *et al.* (2003). Hundred-year decline of North Atlantic predatory fishes. Fish Fish., 4, 1–24.

Christensen, V., Walters, C.J., Pauly, D. & Forrest, R. (2008). Ecopath with Ecosim version 6 User Guide. Lensfest Ocean Futures Project 2008, 1–235.

Clementi, E., Pistoia, J., Delrosso, D., Mattia, G., Fratianni, C., Storto, A., Ciliberti, S., Lemieux, B., Fenu, E., Simoncelli, S., Drudi, M., Grandi, A., Padeletti, D., Di Pietro, P., Pinardi, N., (2017a). A 1/24 degree resolution Mediterranean analysis and forecast modelling system for the Copernicus Marine Environment Monitoring Service. Extended abstract to the 8th EuroGOOS Conference, Bergen.

Clementi, E., Oddo, P., Drudi, M., Pinardi, N., Korres, G., Grandi A., (2017b). Coupling hydrodynamic and wave models: first step and sensitivity experiments in the Mediterranean Sea. Ocean Dynamics. doi: https://doi.org/10.1007/s10236-017-1087-7.

Clementi, E., Aydogdu, A., Goglio, A. C., Pistoia, J., Escudier, R., Drudi, M., Grandi, A., Mariani, A., Lyubartsev, V., Lecci, R., Cretí, S., Coppini, G., Masina, S., & Pinardi, N. (2021). Mediterranean Sea Analysis and Forecast (CMEMS MED-Currents, EAS6 system) (Version 1) [Data set]. Copernicus Monitoring Environment Marine Service (CMEMS). https://doi.org/10.25423/CMCC/MEDSEA_ANALYSISFORECAST_PHY_006_013_EAS6

CMEMS Copernicus Marine Services https://marine.copernicus.eu/

Coll, M. & Steenbeek, J. (2017). Standardized ecological indicators to assess aquatic food webs: The ECOIND software plug-in for Ecopath with Ecosim models. Environ. Model. Softw., 89, 120–130.

Coll, M., Lotze, H.K. & Romanuk, T.N. (2008). Structural degradation in mediterranean sea food webs: Testing ecological hypotheses using stochastic and mass-balance modelling. Ecosystems, 11, 939–960.

Colleter, M., Valls, A., Guitton, J., Gascuel, D., Pauly, D. & Christensen, V. (2015). Global overview of the applications of the Ecopath with Ecosim modeling approach using the EcoBase models repository. Ecol. Modell., 302, 42–53.

Cressman, G. P.: An operational objective analysis scheme, Mon. Weather Rev., 87, 367–374, 1959.

Crowder, L. & Norse, E. (2008). Essential ecological insights for marine ecosystem-based

management and marine spatial planning. Mar. Policy, 32, 772–778.

Davison, S., et al., *Assessment of ERA5 winds in the Mediterranean Sea*. 2019, Institute of Marine Sciences, Italian National Research Council (ISMAR-CNR): Venice, Italy.

Disciplinare integrativo al regolamento di esecuzione ed organizzazione dell'area marina protetta "Secche di Tor Paterno" (Decreto Istitutivo del Ministero dell'Ambiente del 29 novembre 2000). (2021).

Dobricic S., and N. Pinardi (2008). An oceanographic three-dimensional variational data ssimilation scheme. Ocean Modelling, 22 (3-4) 89-105.

DUEL PROJEKT (2019): Uređenje ušća vodotoka Miljašić Jaruge – Izrada idejnog projekta, Rijeka

Ecopath 30 Years Conference Proceedings: Extended Abstracts. (2014). , 22.

ECOSS Project Deliverable 3.2.1. (2020). Report on the ecological monitoring, conservation strategies and management questions of Natura 2000 marine sites.

Eldeberky, Y., *Nonlinear Transformation of Wave Spectra in the Nearshore Zone*, in *Delft University of Technology, Department of Civil Engineering*. 1996: The Netherlands.

Escudier, R., Clementi, E., Omar, M., Cipollone, A., Pistoia, J., Aydogdu, A., Drudi, M., Grandi, A., Lyubartsev, V., Lecci, R., Cretí, S., Masina, S., Coppini, G., & Pinardi, N. (2020). Mediterranean Sea Physical Reanalysis (CMEMS MED-Currents) (Version 1) Data set. Copernicus Monitoring Environment Marine Service (CMEMS). https://doi.org/10.25423/CMCC/MEDSEA_MULTIYEAR_PHY_006_004_E3R1

Escudier, R., Clementi, E., Cipollone, A., Pistoia, J., Drudi, M., Grandi, A., Lyubartsev, V., Lecci, R., Aydogdu, A., Delrosso, D., Omar, M., Masina, S., Coppini G., Pinardi, N. (2021). A High Resolution Reanalysis for the Mediterranean Sea. Frontiers in Earth Science, 9, 1060, https://www.frontiersin.org/article/10.3389/feart.2021.702285, DOI=10.3389/feart.2021.702285

Estévez, R.A. & Gelcich, S. (2015). Participative multi-criteria decision analysis in marine management and conservation: Research progress and the challenge of integrating value judgments and uncertainty. Mar. Policy, 61, 1–7.

eXact team. (n.d.). *eXact lab C3HPC*. Retrieved February 22, 2021, from https://www.exact-lab.it/?page_id=46

eXact team. (2020). *A Quick Start Guide to the eXact lab C3HPC*.

Falace, A., Kaleb, S., Curiel, D., Miotti, C., Galli, G., Querin, S., *et al.* (2015). Calcareous bio-concretions in the Northern Adriatic Sea: Habitat types, environmental factors that influence Habitat distributions, and predictive modeling. PLoS One, 10, 1–21.

Fao. (2008). Building an Ecosystem Approach To Aquaculture. Fao, 231.

Federico, I., Pinardi, N., Coppini, G., Oddo, P., Lecci, R., Mossa, M., 2017. Coastal ocean forecasting with an unstructured grid model in the Southern Adriatic and Northern Ionian seas, Nat. Hazards Earth Syst. Sci., 17, 45–59.

Feng, X. and X. Chen, *Feasibility of ERA5 reanalysis wind dataset on wave simulation for the western inner-shelf of Yellow Sea.* Ocean Engineering, 2021. 236.

Ferrarin, C., Roland, A., Bajo, M., Umgiesser, G., Cucco, A., Davolio, S., Buzzi, A., Malguzzi, P., Drofa, O., 2013. Tide-surge-wave modelling and forecasting in the Mediterranean Sea with focus on the Italian coast, Ocean Model., 61, 38–48.

Ferrarin C, Maicu F, Umgiesser G., 2017. The effect of lagoons on Adriatic Sea tidal dynamics. Ocean Model., 119:57–71.

Ferrarin, C., Bellafiore, D., Sannino, G., Bajo, M., & Umgiesser, G. (2018). Tidal dynamics in the inter-connected Mediterranean, Marmara, Black and Azov seas. *Progress in Oceanography*, *161*, 102–115. https://doi.org/10.1016/j.pocean.2018.02.006

Ferrarin, C., Cucco, A., Umgiesser, G., Bellafiore, D., & Amos, C. L. (2010). Modelling fluxes of water and sediment between Venice Lagoon and the sea. *Continental Shelf Research*, *30*(8), 904–914. https://doi.org/10.1016/j.csr.2009.08.014

Ferrarin, C., Umgiesser, G., Bajo, M., Bellafiore, D., De Pascalis, F., Ghezzo, M., Mattassi, G., & Scroccaro, I. (2010). Hydraulic zonation of the lagoons of Marano and Grado, Italy. A modelling approach. *Estuarine, Coastal and Shelf Science*, *87*(4), 561–572. https://doi.org/10.1016/j.ecss.2010.02.012

Ferrarin, C., Umgiesser, G., Roland, A., Bajo, M., De Pascalis, F., Ghezzo, M., & Scroccaro, I. (2016). Sediment dynamics and budget in a microtidal lagoon — A numerical investigation. *Marine Geology*, *381*, 163–174. https://doi.org/10.1016/j.margeo.2016.09.006

Fortibuoni, T., Canese, S., Bortoluzzi, G., Franceschini, G. & Giovanardi, O. (2020)(a). Bathymetry data (GeoTIFF image format) of the Northern Adriatic Tegnùe di Chioggia site collected in 2014-2015 for the DeFishGear project. IEDA. doi:10.26022/IEDA/329816

Fortibuoni, T., Canese, S., Bortoluzzi, G., Franceschini, G. & Giovanardi, O. (2020)(b). Bathymetry

data (GeoTIFF grid format) of the Northern Adriatic Tegnùe di Chioggia site collected in 2014-2015 for the DeFishGear project. IEDA. doi:10.26022/IEDA/329815

Fouzai, N., Coll, M., Palomera, I., Santojanni, A., Arneri, E. & Christensen, V. (2012). Fishing management scenarios to rebuild exploited resources and ecosystems of the Northern-Central Adriatic (Mediterranean Sea). J. Mar. Syst., 102–104, 39–51.

Frölicher, T.L. & Laufkötter, C. (2018). Emerging risks from marine heat waves. Nat. Commun., 9, 2015–2018.

Goda (2010), Random Seas and Design of Maritime Structures, Advanced Series on Ocean Engineering: Vol. 33, pp. 732, https://doi.org/10.1142/7425

Gordini, E. & Ciriaco, S. (2020). Bathymetry data (GeoTIFF grid format) of the Northern-most Adriatic area: Interreg Ita-Slo 2007-2013 TRECORALA Project. IEDA. doi:10.26022/IEDA/329903

Günther, H., Hasselmann, S., & Janssen, P. A. E. M. (1992). The WAM model Cycle 4 (revised version). Klim. Rechenzentrum. Techn. Rep, (4), 23-40.

Gunther, H., Hasselmann, H., Janssen, P.A.E.M., (1993). The WAM model cycle 4, DKRZ report n. 4.

Gutmann, H.M., *A radial basis function method for global optimization.* Journal of Global Optimization, 2001. **19**(3): p. 201-227.

Hanna, S.R. and D.W. Heinold (1985), Development and Application of a Simple Method for Evaluating Air Quality., American Petroleum Institute, Health and Environmental Affairs Department: Washington, DC, USA

Hasselmann, K., *ON THE SPECTRAL DISSIPATION OF OCEAN WAVES DUE TO WHITE CAPPING.* Boundary-Layer Meteorology, 1973. **6**: p. 107-127.

Hasselmann, K. (1974). On the characterization of ocean waves due to white capping, Boundary-Layer Meteorology, 6, 107-127.

Hasselmann, S., et al., *Computations and parameterizations of the nonlinear energy transfer in a Gravity-Wave specturm.* J. Phys. Oceanogr., 1985. **15**: p. 1378–1391.

Hasselmann, D.; Bösenberg, J.; Dunckel, M.; Richter, K.; Grünewald, M.; Carlson, C. Measurements of wave-induced pressure over surface gravity waves. In Wave Dynamics and Radio Probing of the Ocean Surface; Springer: Boston, MA, USA, 1986; pp. 353–368.

Hellerman, S., Rosenstein, M. (1983). Normal monthly wind stress over the world ocean with error estimates. Journal of Physical Oceanography, 13(7), 1093-1104.

Hernvann, P.Y., Gascuel, D., Grüss, A., Druon, J.N., Kopp, D., Perez, I., *et al.* (2020). The Celtic Sea

Through Time and Space: Ecosystem Modeling to Unravel Fishing and Climate Change Impacts on Food-Web Structure and Dynamics. Front. Mar. Sci., 7, 1–26.

Hersbach, H., et al., *The ERA5 global reanalysis.* Quarterly Journal of the Royal Meteorological Society, 2020. **146**(730): p. 1999-2049.

Heymans, J.J., Coll, M., Link, J.S., Mackinson, S., Steenbeek, J., Walters, C., *et al.* (2016). Best practice in Ecopath with Ecosim food-web models for ecosystem-based management. Ecol. Modell., 331, 173–184.

ISPRA. (2010). "Valutazione Degli Effetti Della Zona Di Tutela Biologica Di Chioggia Sui Popolamenti Demersali e Bentonici e Sulle Possibilità Di Ripopolamento Di Specie Di Interesse Commerciale."

Jackson, J.B.C., Kirby, M.X., Berger, W.H., Bjorndal, K. a, Botsford, L.W., Bourque, B.J., *et al.* (2001). Historical Overfishing and the Recent Collapse of Coastal Ecosystems Published by : American Association for the Advancement of Science Stable URL : http://www.jstor.org/stable/3084305 REFERENCES Linked references are available on JSTOR for this article : Science (80-.)., 293, 629–638.

Jacob, D., Petersen, J., Eggert, B., Alias, A., Christensen, O.B., Bouwer, L.M., *et al.* (2014). EURO-CORDEX: New high-resolution climate change projections for European impact research. Reg. Environ. Chang., 14, 563–578.

Janeković, I., Kuzmić, M. (2005): Numerical solution of the Adriatic Sea principal tidal constituents, *Annales geophysicae*, 23, pp. 3207-3218

Janssen, P.A.E.M., *Wave-Induced Stress and the Drag of Air Flow over Sea Waves.* Journal of Physical Oceanography, 1989. **19**(6): p. 745-754.

Janssen, P., *Quasi-linear Theory of Wind-Wave Generation Applied to Wave Forecasting.* Journal of Physical Oceanography, 1991. **21**: p. 1631-1642.

Jerlov, N. G. (1976). Marine optics. Elsevier.

Kara, B. A., Wallcraft, A. J., Hurlburt, H. E., 2007. A Correction for Land Contamination of Atmospheric Variables near Land–Sea Boundaries, J. Phys. Oceanogr., 37, 803–818.

Khalili, N.R. & Duecker, S. (2013). Application of multi-criteria decision analysis in design of sustainable environmental management system framework. J. Clean. Prod., 47, 188–198.

Killworth, Peter D. (1996). "Time Interpolation of Forcing Fields in Ocean Models". In: Journal of Physical Oceanography 26.1, pp. 136–143.

Komen, G.J., S. Hasselmann, and K. Hasselmann, *On the Existence of a Fully-Developed Wind-Sea*

Spectrum. Journal of Physical Oceanography, 1984. **14**(8): p. 1271-1285.

Komen, G. J., L. Cavaleri, M. Donelan, K. Hasselmann, S. Hasselmann, and P. A. E. M. Janssen. Dynamics and Modelling of Ocean Waves. Cambridge University Press, sep 1994. ISBN 9780521577816. doi: 10.1017/CBO9780511628955. URL https://www.cambridge.org/core/product/identifier/ 9780511628955/type/book.

Kondo, J. 1975. Air-sea bulk transfer coefficients in diabatic conditions. Boundary- Layer Meteorol., 9: 91-112.

Korres, G., Ravdas, M., Zacharioudaki, A., Denaxa, D., & Sotiropoulou, M. (2021). Mediterranean Sea Waves Reanalysis (CMEMS Med-Waves, MedWAM3 system) (Version 1) Data set. Copernicus Monitoring Environment Marine Service (CMEMS). https://doi.org/10.25423/CMCC/MEDSEA_MULTIYEAR_WAV_006_012

Korres, G., Ravdas, M., Denaxa, D., & Sotiropoulou, M. (2021). Mediterranean Sea Waves Reanalysis INTERIM (CMEMS Med-Waves, MedWAM3I system) (Version 1) Data set. Copernicus Monitoring Environment Marine Service (CMEMS). https://doi.org/10.25423/CMCC/MEDSEA_MULTIYEAR_WAV_006_012_MEDWAM3I

La Sorte, F.A., Johnston, A. & Ault, T.R. (2021). Global trends in the frequency and duration of temperature extremes. Clim. Change, 166, 1–14.

Liang, B.C., et al., *22-Year wave energy hindcast for the China East Adjacent Seas.* Renewable Energy, 2014. **71**: p. 200-207.

Libralato, S. (2018). System omnivory index. Encycl. Ecol., 1, 481–486.

Libralato, S., Caccin, A. & Pranovi, F. (2015). Modeling species invasions using thermal and trophic niche dynamics under climate change. Front. Mar. Sci., 2.

Lundquist, C.J. & Granek, E.F. (2005). Strategies for successful marine conservation: Integrating socioeconomic, political, and scientific factors. Conserv. Biol., 19, 1771–1778.

Lynch, D.R and W.G. Gray (1979). A wave equation model for finite element tidal computations. In: Computers & fluids 7.3, pp. 207–228.

Madec, Gurvan and the NEMO team, (2016). NEMO ocean engine: version 3.6 stable. Note du Pole de modelisation, Institut Pierre-Simon Laplace N 27. ISSN No 1288-1619. https://www.nemo-ocean.eu/wp-content/uploads/NEMO_book.pdf

Maderich V., Ilyin Y., Lemeshko E., 2015. Seasonal and interannual variability of the water exchange in the Turkish Straits System estimated by modelling. Mediterranean Marine Science, [S.l.], v. 16, n. 2, p. 444-459, ISSN 1791-6763, doi:http://dx.doi.org/10.12681/mms.1103.

Mazzoldi, C., Sambo, A. & Riginella, E. (2014). The Clodia database: A long time series of fishery data from the Adriatic Sea. Sci. Data, 1, 1–8.

Međugorac, I., Pasarić, M., Orlić, M. (2015): Severe flooding along the eastern Adriatic coast: the case of 1 December 2008, *Ocean Dynamics*, 65, pp. 817-830.

Međugorac, I., Pasarić, M., Pasarić, Z., Orlić, M. (2016): Two recent storm-surge episodes in the Adriatic, *International Journal of Safety and Security Engineering*, 6(3), pp. 589–596.

Međugorac, I., Orlić, M., Janeković., Pasarić, Z., Pasarić, M. (2018): Adriatic storm surges and related cross-basin sea-level slope, *Journal of Marine Systems*, 181, pp. 79-90.

Medvedev, I. P., Vilibić, I., Rabinovich, A. B. (2020): Tidal resonance in the Adriatic Sea: Observational Evidence, *Journal of Geophysical Research – Oceans,* 125, e2020JC016168,

Melli, V., Angiolillo, M., Ronchi, F., Canese, S., Giovanardi, O., Querin, S., *et al.* (2017). The first assessment of marine debris in a Site of Community Importance in the north-western Adriatic Sea (Mediterranean Sea). Mar. Pollut. Bull., 114, 821–830.

Mentaschi, L., et al. (2013), Problems in RMSE-based wave model validations. Ocean Modelling, 72, p. 53-58.

Mesinger, F., Janjic, Z. I., Nickovic, S., Gavrilov, D., and Deaven, D. G.: The step-mountain coordinate: model description and per- formance for cases of Alpine lee cyclogenesis and for a case of an Appalachian redevelopment, Mon. Weather Rev., 116, 1493– 1518, 1988.

Moss, R.H., Edmonds, J.A., Hibbard, K.A., Manning, M.R., Rose, S.K., Van Vuuren, D.P., *et al.* (2010). The next generation of scenarios for climate change research and assessment. Nature, 463, 747–756.

Nakicenovic, N., *et al.* (2000) Special Report on Emissions Scenarios. Cambridge University Press, Cambridge, 599 p.

Napolitano, E., Iacono, R., Sorgente, R., Fazioli, L., Olita, A., Cucco, A., Oddo, P., and Guarnieri, A.: The regional forecasting systems of the Italian seas, Journal of Operational Oceanography, 9, 66–76, 2016.

Nigam, T., Escudier, R., Pistoia, J., Aydogdu, A., Omar, M., Clementi, E., Cipollone, A., Drudi, M.,

Grandi, A., Mariani, A., Lyubartsev, V., Lecci, R., Cretí, S., Masina, S., Coppini, G., & Pinardi, N. (2021). Mediterranean Sea Physical Reanalysis INTERIM (CMEMS MED-Currents, E3R1i system) (Version 1) Data set. Copernicus Monitoring Environment Marine Service (CMEMS). https://doi.org/10.25423/CMCC/MEDSEA_MULTIYEAR_PHY_006_004_E3R1I

Oddo P., N. Pinardi, M. Zavatarelli, 2005. "A numerical study of the interannual variability of the Adriatic Sea (2000-2002)", The Science of the Total Environment, 353, 39-56

Oddo, P., Adani, M., Pinardi, N., Fratianni, C., Tonani, M., Pettenuzzo, D., (2009). A Nested Atlantic-Mediterranean Sea General Circulation Model for Operational Forecasting. Ocean Sci. Discuss., 6, 1093-1127.

Oddo, P., Bonaduce, A., Pinardi, N., Guarnieri, A., (2014) Sensitivity of the Mediterranean sea level to atmospheric pressure and free surface elevation numerical formulation in NEMO. Geosci. Model Dev., 7, 3001–3015.

Pacanowsky, R.C., and Philander S.G.H., (1981) Parameterization of vertical mixing in numerical models of tropical oceans. J Phys Oceanogr 11:1443-1451

Pallares, E., et al., Comparison between nested grids and unstructured grids for a high-resolution wave forecasting system in the western Mediterranean sea. Journal of Operational Oceanography, 2017. **10**(1): p. 45-58.

Pauly, D. & Watson, R. (2005). Background and interpretation of the "Marine Trophic Index" as a measure of biodiversity. Philos. Trans. R. Soc. B Biol. Sci., 360, 415–423.

Perez, J., M. Menendez, and I.J. Losada, *GOW2: A global wave hindcast for coastal applications.* Coastal Engineering, 2017. **124**: p. 1-11.

Pettenuzzo, D., Large, W.G., Pinardi, N., (2010) On the corrections of ERA-40 surface flux products consistent with the Mediterranean heat and water budgets and the connection between basin surface total heat flux and NAO. Journal of Geophysical Research 115, C06022, doi:10.1029/2009JC005631

Piazzi, L., Gennaro, P. & Balata, D. (2012). Threats to macroalgal coralligenous assemblages in the Mediterranean Sea. Mar. Pollut. Bull., 64, 2623–2629.

Pomeroy, R. & Douvere, F. (2008). The engagement of stakeholders in the marine spatial planning process. Mar. Policy, 32, 816–822.

Ponti, M. & Mastrototaro, F. (2005). Distribuzione dei popolamenti ad ascidie sui fondali rocciosi (Tegnùe) al largo di Chioggia (Venezia) In: Riassunti del 36° Congresso nazionale della Società

Italiana di Biologia Marina. Trieste. SIBM 324 pp

Ponti, M. (2020)(a). 3D wireframe plot of the northern Adriatic mesophotic biogenic reefs. https://zenodo.org/search?page=1&size=20&q=3D%20wireframe%20plot%20tegn%C3%B9a

Ponti, M. (2020)(b). Single-beam bathymetry data (ESRI ASCII grid format) of selected mesophotic biogenic reefs from the northern Adriatic Sea. IEDA. doi:10.26022/IEDA/329803

Ponti, M. (2020)(c). Single-beam bathymetry data (GeoTIFF image format) of selected mesophotic biogenic reefs from the northern Adriatic Sea. IEDA. doi:10.26022/IEDA/329814

Ponti, M., Fava, F. & Abbiati, M. (2011). Spatial-temporal variability of epibenthic assemblages on subtidal biogenic reefs in the northern Adriatic Sea. Mar. Biol., 158, 1447–1459.

Provini A, Crosa G, Marchetti R (1992) Nutrient export from Po and Adige river basins over the last 20 years. Sci Total Environ Suppl:291–313

Reed, R. K. 1977. On estimating insolation over the ocean. J. Phys. Oceanogr., 17: 854- 871.

Regis, R.G. and C.A. Shoemaker, *A stochastic radial basis function method for the global optimization of expensive functions.* Informs Journal on Computing, 2007. **19**(4): p. 497-509.

Rodi, W. (1987): Examples of Calculation Methods for Flow and Mixing in Stratified Fluids, *Journal of Geophysical Research*, 92, (C5), pp. 5305-532

Roe, P.L. (1981): Approximate Riemann solvers, parameters vectors and difference schemes, *Journal of Computational Physics*, 43, pp. 357-372.

Rogers, W.E., P.A. Hwang, and D.W. Wang, *Investigation of wave growth and decay in the SWAN model: Three regional-scale applications.* Journal of Physical Oceanography, 2003. **33**(2): p. 366-389.

Rummukainen, M. (2013). Climate change: Changing means and changing extremes. Clim. Change, 121, 3–13.

Russo, A. & Artegiani, A. (1996). Adriatic sea hydrography. Scientia Marina, 60, 33-43.

Russo, E., Monti, M.A., Mangano, M.C., Raffaetà, A., Sarà, G., Silvestri, C., *et al.* (2020). Temporal and spatial patterns of trawl fishing activities in the Adriatic Sea (Central Mediterranean Sea, GSA17). Ocean Coast. Manag., 192.

Sala, E., Ballesteros, E., Dendrinos, P., Di Franco, A., Ferretti, F., Foley, D., *et al.* (2012). The structure of mediterranean rocky reef ecosystems across environmental and human gradients, and conservation implications. PLoS One, 7.

Šantić, M., Paladin, A. & Rada, B. (2011a). Feeding habits of common pandora Pagellus erythrinus (Sparidae) from eastern central Adriatic Sea. Cybium, 35, 83–90.

Šantić, M., Rada, B., Paladin, A. & Kovačević, A. (2011b). Biometric properties and diet of common pandora, Pagellus erythrinus (Osteichthyes: Sparidae), from the eastern Adriatic Sea. Arch. Biol. Sci., 63, 217–224.

Šepić, J., Balić, M., Čupić, S., Didenkulova, I., Heidarzadeh, M., Karlović, M., Kim, J., Matić, F., Međugorac, I., Mihanović, H. et al. (2022): Contribution of the short-period sea level oscillations (T < 2 h) to the flooding events along the European coasts, *Ocean Science Meeting 2022*, online lecture, pp. 1

S.HY.F.E.M. (n.d.). Retrieved February 18, 2021, from https://sites.google.com/site/shyfem/project-definition

Simoncelli, S., Pinardi, N., Oddo, P., Mariano, A. J., Montanari, G., Rinaldi, A., and Deserti, M.: Coastal Rapid Environmental As- sessment in the Northern Adriatic Sea, Dynam. Atmos. Oceans, 52, 250–283, 2011.

Sleigh, D.H., Gaskel, P.H. (1998): An unstructured finite volume algorithm for predicting flow in rivers and estuaries, *Computer and Fluids*, 27(4), pp. 479-508.

Smagorinsky, J. (1993): *Some historical remarks on the use of nonlinear viscosities*, In: Large eddy simulations of complex engineering and geophysical flows, B. Galperin and S. Orszag Eds.), Cambridge Univ. Press, pp. 1-34.

SMAGORINSKY, J. (1963). GENERAL CIRCULATION EXPERIMENTS WITH THE PRIMITIVE EQUATIONS. *Monthly Weather Review*, *91*(3), 99–164. https://doi.org/10.1175/1520-0493(1963)091<0099:GCEWTP>2.3.CO;2

Snyder, R.L., et al., *Array Measurements of Atmospheric-Pressure Fluctuations above Surface Gravity-Waves.* Journal of Fluid Mechanics, 1981. 102(Jan): p. 1-59.

Song, Y., Haidvogel, D. (1994): A semi-implicit ocean circulation model using a generalised topography-following coordinate system, *Journal of Comp. Physics*, 115, pp. 228-244.

Storto, A., Masina, S., Navarra, A., (2015). Evaluation of the CMCC eddy-permitting global ocean physical reanalysis system (C-GLORS, 1982-2012) and its assimilation components. Quarterly Journal of the Royal Meteorological Society, 142, 738–758, doi: 10.1002/qj.2673.

The Concise Encyclopedia of Statistics. (2008). Springer New York. https://doi.org/10.1007/978-0-387-32833-1

The SWAN team, *SWAN SCIENTIFIC AND TECHNICAL DOCUMENTATION*. 2022, Delft University of Technology: Delft.

Tolman H.L. (2002). Validation of WAVEWATCH III version 1.15 for a global domain.NOAA / NWS / NCEP / OMB Technical Note 213, 33 pp.

Tolman H.L. (2009). User Manual and system documentation of WAVEWATCH III version 3.14. NOAA/NWS/NCEP/MMAB Technical Note 276, 194 pp + Appendices.

Tonani, M., Pinardi, N., Dobricic, S., Pujol, I., Fratianni, C., (2008). A high-resolution free-surface model of the Mediterranean Sea. Ocean Sci., 4, 1-14.

Tonani, M., Balmaseda, M., Bertino, L., Blockley, E., Brassington, G., Davidson, F., Drillet, Y., Hogan, P., Kuragano, T., Lee, T., Mehra, A., Paranathara, F., Tanajura, CAS, Wang, H., (2015) Status and future of global and regional ocean prediction systems. J Operational Oceanography 8:201-220, doi:10.1080/1755876X.2015.1049892.

Toro, E., F. (1997): *Riemann Solvers and Numerical Methods for Fluid Dynamics*, Springer, Germany.

Trincardi, F., Barbanti, A., Bastianini, M., Benetazzo, L., Cavaleri, L., Chiggiato, J., Papa, A., Pomaro, A., Sclavo, M., Tosi, L., Umgiesser, G. (2016): The 1966 flooding of Venice: What time taught us for the future, *Oceanography*, 29(4), str. 178-186.

Tsimplis, M. N., Blackman, D. (1997): Extreme sea-level distribution and return periods in the Aegaen and Ionian Seas*, Estaruine, Coastal and Shelf Science,* 44(1), str. 79-89.

Umgiesser, G. (2004). *Finite Element Model for Coastal Seas User Manual*.

Umgiesser, G., Canu, D. M., Cucco, A., & Solidoro, C. (2004). A finite element model for the Venice Lagoon. Development, set up, calibration and validation. *Journal of Marine Systems*, *51*(1–4), 123–145. https://doi.org/10.1016/j.jmarsys.2004.05.009

Umgiesser, G., Ferrarin, C., Cucco, A., De Pascalis, F., Bellafiore, D., Ghezzo, M., & Bajo, M. (2014). Comparative hydrodynamics of 10 Mediterranean lagoons by means of numerical modeling. *Journal of Geophysical Research: Oceans*, *119*(4), 2212–2226. https://doi.org/10.1002/2013JC009512

UNEP MAP/MED POL. (2011). Modelling for Maritime Spatial Planning: Tools, concepts, applications - BaltSeaPlan Report 19.

Vallarola, F., De Ascentiis, A. & Cargini, D., a cura di Torre del Cerrano e Natura 2000, Area Marina Protetta Torre del Cerrano. (2015). Torre del Cerrano e Natura 2000; Piano di Gestione del Sito di Interesse Comunitario IT7120215 "Torre del Cerrano"Editpress, Pineto-Silvi (Te).

van Vuuren, D.P., de Vries, B., Beusen, A. & Heuberger, P.S.C. (2008). Conditional probabilistic estimates of 21st century greenhouse gas emissions based on the storylines of the IPCC-SRES scenarios. Glob. Environ. Chang., 18, 635–654.

Vannucchi, V., et al., *Dynamical Downscaling of ERA5 Data on the North-Western Mediterranean Sea: From Atmosphere to High-Resolution Coastal Wave Climate.* Journal of Marine Science and Engineering, 2021. **9**(2).

Verri, G., Pinardi, N., Oddo, P., Ciliberti, S. A., and Coppini, G.: River runoff influences on the Central Mediterranean Overturning Circulation, Clim. Dynam., 2017.

Voinov, A. & Bousquet, F. (2010). Modelling with stakeholders. Environ. Model. Softw., 25, 1268–1281.

Walters, C. J., D. Pauly & Christensen, V. (1999). Ecospace: Prediction of Mesoscale Spatial Patterns in Trophic Relationships of Exploited Ecosystems, with Emphasis on the Impacts of Marine Protected Areas. Ecosystems 2(6):539–554.

Walters, C., Christensen, V. & Pauly, D. (1997). Walters et al 1997.pdf. Rev. Fish Biol. Fish., 7, 139–172.

Walters, C., Pauly, D., Christensen, V. & Kitchell, J.F. (2000). Representing density dependent consequences of life history strategies in aquatic ecosystems: EcoSim II. Ecosystems, 3, 70–83.

Weatherall, P., et al., *A new digital bathymetric model of the world's oceans.* Earth and Space Science, 2015. **2**(8): p. 331-345.

White, E.R. & Hastings, A. (2020). Seasonality in ecology: Progress and prospects in theory. Ecol. Complex., 44.

Wu, J. (1994.): The sea surface is aerodynamically rough even under light winds, *Boundary layer Meteorology*, 69, pp. 149-158.

Wu, W., et al., *Evaluation of different wind resources in simulating wave height for the Bohai, Yellow, and East China Seas (BYES) with SWAN model.* Continental Shelf Research, 2020. **207**.

Wu, W., et al., *A quantitative method to calibrate the SWAN wave model based on the whitecapping dissipation term.* Applied Ocean Research, 2021. 114

Zhang, Y., Ye, F., Stanev, E.V., Grashorn, S. (2016a): Seamless cross-scale modeling with SCHISM, *Ocean Modelling*, 102, str. 64-81.

Zhang, Y., Priest, G.R., Allan, J., Stimely, L. (2016b) Benchmarking an unstructured-grid model for tsunami current modeling, *Pure and Applied Geophysics*, 173, doi: 4075-4087.

https://www.facebook.com/ninzadarhalf/videos/nin-11-09-2017/2172671973053764/ (date of access, February 10th, 2023)

https://podaac.jpl.nasa.gov/announcements/2021-08-09-Sea-level-projections-from-the-IPCC-6th-Assessment-Report

www.navionics.com (date of access: January 15th, 2023)

www.wunderground.com/history/daily/hr/zemunik-donji/LDZD (date of access: February 4th, 2023)